NASA Technical Paper 3407

ATCOM Technical Report 93-A-002

September 1993

Effect of an Extendable Slat on the Stall Behavior of a VR-12 Airfoil

P. Plantin De Hugues, K. W. McAlister, and C. Tung

US ARMY AVIATION and TROOP COMMAND

National Aeronautics and Space Administration

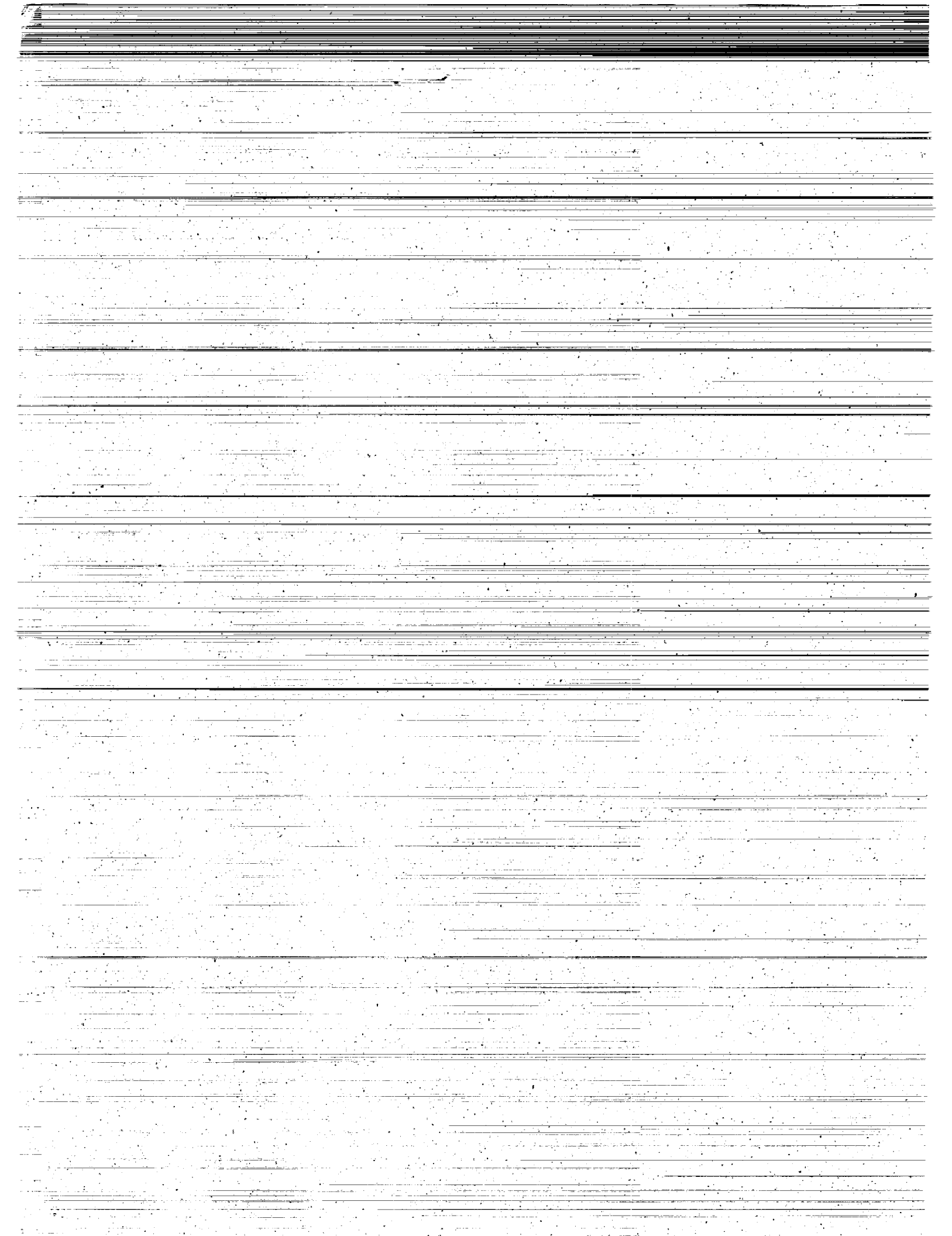

NASA Technical Paper 3407

ATCOM Technical Report 93-A-002

1993

Effect of an Extendable Slat on the Stall Behavior of a VR-12 Airfoil

P. Plantin De Hugues
French Foreign Ministry, Paris, France

K. W. McAlister and C. Tung
Aeroflightdynamics Directorate
U.S. Army Aviation and Troop Command
Ames Research Center, Moffett Field, California

National Aeronautics and Space Administration

Ames Research Center
Moffett Field, California 94035-1000

CONTENTS

EFFECT OF AN EXTENDABLE SLAT ON THE STALL BEHAVIOR OF A VR-12 AIRFOIL

P. Plantin De Hugues,* K. W. McAlister,† and C. Tung†

Ames Research Center

SUMMARY

Experimental and computational tests were performed on a VR-12 airfoil to determine if the dynamic-stall behavior that normally accompanies high-angle pitch oscillations could be modified by segmenting the forward portion of the airfoil and extending it ahead of the main element. In the extended position the configuration would appear as an airfoil with a leading-edge slat, and in the retracted position it would appear as a conventional VR-12 airfoil. The calculations were obtained from a numerical code that models the vorticity transport equation for an incompressible fluid. These results were compared with test data from the water tunnel facility of the Aeroflightdynamics Directorate at Ames Research Center.

Steady and unsteady flows around both airfoils were examined at angles of attack between 0° and 30°. The Reynolds number was fixed at 200,000, and the unsteady pitch oscillations followed a sinusoidal motion described by $\alpha = \alpha_m + 10° \sin(\omega t)$. The mean angle ($\alpha_m$) was varied from 10° to 20° and the reduced frequency from 0.05 to 0.20. The results from the experiment and the calculations show that the extended-slat VR-12 airfoil experiences a delay in both static and dynamic stall not experienced by the basic VR-12 airfoil.

INTRODUCTION

Considering a helicopter in forward flight, the angle of attack of each blade oscillates between a small angle on the advancing side to an high angle on the retreating side. Airfoils that oscillate in pitch will not only shed vorticity from the trailing edge, but if the amplitude if sufficiently high, they may shed a more concentrated vortex from the leading edge (fig. 1). The evolution in time of this leading-edge vortex, as it forms at a high angle of attack and moves over the upper surface of the airfoil, is what is responsible for the phenomenon known as dynamic stall.

The loads that result from dynamic stall are severe enough to be seen as being among the most important limitations to helicopter speed. The sudden loss of lift and the increase in both drag and pitching moment are known to induce large and potentially dangerous vibrations. An airfoil design that eliminates, or even reduces, the effects of dynamic stall would contribute substantially to the overall performance of a rotor.

Several methods have been proposed to delay, or possibly eliminate, dynamic stall on pitching airfoil sections. One of these methods involves the addition of a small aerodynamic element, called a slat, in front of the airfoil. The slat is mounted ahead of the airfoil in such an attitude as to assist in turning the flow around the leading edge when the airfoil is at a high angle of attack, thereby delaying the onset of leading-edge stall. In a recent water tunnel study (ref. 1) it was demonstrated that a slatted airfoil not only delays the static stall angle, but under certain conditions also suppresses the characteristic deep-stall phenomenon that normally occurs on the basic airfoil. The two-element configuration in this previous study was based on a VR-7 airfoil with a small NACA element extended and drooped ahead of the main element.

In order to develop a more streamlined configuration with a potentially higher Mach number divergence, a new, two-element design was proposed based on a VR-12 airfoil. In this case the slat was to be formed by simply extending the forward portion of the airfoil using a parting line that would result in a well-tailored passage between the two elements. When the slat is extended, the configuration appears as a multi-element airfoil, and when the slat is retracted, the configuration appears as a VR-12 airfoil (fig. 2). A movable slat

*French Foreign Ministry, Paris, France.

†Aeroflightdynamics Directorate, ATCOM, Ames Research Center, Moffett Field, California.

might be used in a similar fashion, as was the Handley Page automatic slot (ref. 2).

In this experiment the steady and unsteady lift, drag, and pitching moment were measured on the entire multi-element configuration. In addition, flow visualizations were performed using a fluorescing dye injected not only from the leading edge of the main element, but also from the leading edge of the slat. A computational fluid dynamics (CFD) study of the aerodynamics of both the basic and the extended-slat airfoils was undertaken to validate the code against the experimentally observed results.

NOMENCLATURE

A_p	planform area of airfoil (span×chord)
B	boundary of fluid region
c	chord of basic VR-12 airfoil
C_d	drag coefficient, drag/$A_p q_\infty$
C_l	lift coefficient, lift/$A_p q_\infty$
C_m	moment coefficient, moment/$cA_p q_\infty$
k	reduced frequency, $\omega c/2V_\infty$
$\vec{n}$	unit vector
q_∞	dynamic pressure, $\frac{1}{2}\rho V_\infty^2$
$\vec{Q}$	gradient of fundamental solution, eq. (5)
$\vec{r}$	cylindrical coordinate
R	fluid domain
Re	Reynolds number, cV_∞/ν
t	time
$\vec{v}$	calculated velocity vector
V_∞	free-stream velocity
$\vec{w}$	calculated vorticity vector
x	distance along airfoil chord
α	airfoil angle of attack
α_m	airfoil mean angle of attack
ν	fluid kinematic viscosity
ρ	fluid density
ω	frequency of oscillation in pitch, rad/sec

CODE DESCRIPTION

The computer code (called ZETA) used in this study was developed for incompressible, unsteady, two-dimensional viscous flows around a multi-element airfoil (ref. 3). Vorticity is made the primary variable and the solution is partitioned into its kinematic and kinetic parts. Since vorticity is normally limited to only a portion of the flow field, a considerable computational savings is realized. The kinematic part of the solution concerns the continuity equation

$$\nabla \cdot \vec{v} = 0 \tag{1}$$

along with the definition of vorticity,

$$\nabla \times \vec{v} = \vec{w} \tag{2}$$

where $\vec{v}$ and $\vec{w}$ are the velocity and vorticity vectors, respectively. The kinetic part of the solution concerns the Reynolds-averaged transport of vorticity,

$$\frac{\delta \vec{w}}{\delta t} = -(\vec{v} \cdot \nabla)\vec{w} + \nabla \cdot (\nu \nabla \vec{w}) \tag{3}$$

where t represents time and ν is the kinematic viscosity of the fluid. When the flow is turbulent, ν will include the eddy viscosity, which in this case is represented by the Baldwin-Lomax model. Using the fundamental solution of an elliptic equation, equations (1) and (2) can be recast into an integral form for the velocity vector as

$$\begin{aligned}\vec{v}(\vec{r},t) = &-\int_R \vec{w}_o \times \vec{Q} dR_o \\ &+ \int_S [(\vec{v}_o \cdot \vec{n}_o) - (\vec{v}_o \times \vec{n}_o)] \\ &\times \vec{Q} dB_o + \vec{v}_\infty\end{aligned} \tag{4}$$

where $\vec{r}$ is a position vector, $\vec{v}_\infty$ is the free-stream velocity, R is the fluid domain contained between the far-stream boundary and the solid surface S, and $\vec{n}$ is a unit normal vector on S facing away from the region R. The subscript "o" indicates that the variable, the differentiation, or the integration is performed in the r_o space. Q is the gradient of the fundamental solution, which for two-dimensional flows is given by

$$\vec{Q} = \frac{\vec{r}_o - \vec{r}}{2\pi |\vec{r}_o - \vec{r}|^2} \tag{5}$$

On each internal and external boundary, two Dirichlet-type boundary conditions are required for the solution of the vorticity and velocity vectors. These boundary conditions are obtained by solving equation (4) with different initial conditions.

The numerical procedure involves the conformal mapping of the physical domain onto a circular region over which a simple computation grid is defined. The grid in the computational plane consists of concentric

circles and radial lines within a unit circle. The unit circle corresponds to the surface of the airfoil, and the flow field around the airfoil is contained within the unit circle. In the case of a two-element airfoil, the main element is mapped onto the unit circle and the slat onto a smaller circle (concentric with the unit circle). The computational domain is located between the two circles. The steps required to conformally map the extended-slat airfoil onto the computational plane are shown in figure 3. The transformation of the computational grid back onto the physical plane is shown in figure 4. In the case of the extended-slat airfoil, the grid consists of 120 lines in the circumferential direction and 50 lines in the radial direction. For the basic airfoil, these values were reduced to 80 and 45, respectively. A more detailed description of the mathematical formulation, conformal transformation, and solution procedure is given in reference 4.

The equations of motion are solved numerically at discrete points along the solid boundaries and within the fluid interior. The computation loop consists of two kinematic steps using known vorticity and velocity values. The interior vorticity values are computed by solving the vorticity transport equation. New boundary vorticity values are then established using the new interior vorticity. In the next kinetic step, the new velocity values are computed using the vorticity values computed in the kinematic step.

TEST DESCRIPTION

The Facility and the Model

The experimental study was conducted in the Aeroflightdynamics Directorate's closed-circuit water tunnel at Ames Research Center (fig. 5). The advantages at this facility are that unsteady loads on the entire airfoil can be measured and visualizations of the flow can be easily obtained.

The test section is 8.3 in. wide, 12 in. high, and 34 in. long. There are removable windows on all four sides. The free-stream velocity (V_∞) of the water is determined from the difference in static pressure between the settling chamber and the test section. A honeycomb and several screens are positioned in the settling chamber to straighten the flow and reduce the turbulence intensity to about 0.05% when a model is not present in the test section. The turbulence intensity can increase by a factor of five when a stalled airfoil is present in the test section. The tunnel was operated at an ambient temperature of about 70°F.

The model selected for this study was a Boeing–Vertol VR-12 airfoil (fig. 2) with a rectangular planform. The basic airfoil had a chord length of 4 in. To minimize the moment of inertia of the airfoil, the main body of the airfoil was made from a lightweight urethane material and the bulk of the stainless steel spar was concentrated around the quarter-chord pitch axis. The mean camber line over the aft 4% of the VR-12 airfoil is inclined $+3°$ relative to the chord line. To insure rigidity, the thickness of the trailing edge was maintained at $0.005c$ by incorporating a stainless steel plate (0.020 in. thick) along the span of the airfoil.

The chord length of the slat was 11% of the chord of the main element. The slat was positioned $0.035c$ forward of the main element and remained fixed at that distance during the test. The resulting angle of the chord of the slat was $-39.5°$ relative to the chord of the main element. The slat and its attachment ribs were machined from stainless steel as a single unit and joined to the spar with pins. The slat and spar assembly are shown in figure 6 alongside the mold used for constructing the model of the extended-slat VR-12 airfoil.

Load Measurements

When installed in the water tunnel, the spar of the airfoil extended through the test-section windows and was supported by lift and drag transducers on both sides (fig. 7). One end of the spar was connected to an instrumented drive shaft through a torsionally stiff coupling so that airfoil incidence and pitching moment could be measured. Frictional moments imparted by the support bearings and seals were also measured and later treated as dynamic-load tares.

The electrical instrumentation consisted of transducers for the measurement of airfoil incidence, lift (both sides), drag (both sides), total pitching moment, and the bearing and seal moments (both sides). After amplification, these signals were either summed appropriately (i.e., both frictional moments subtracted from the total pitching moment) and displayed on local monitors, or they were transmitted to a remote data-acquisition system where they were digitized and ensemble averaged. Digitizing and averaging operations were based on two additional signals: a 360/rev pulse train that was synchronous with ωt, and a 1/rev pulse

that was synchronous with the beginning of each cycle of oscillation.

In cases involving an airfoil undergoing oscillations in pitch, the ensemble average of a given unsteady load was monitored in real time so that the data-acquisition sequence could be terminated at any time. Although the average was routinely based on 100 cycles of data, this on-line capability of monitoring the progress of the averaging process was especially useful when the period of oscillation was long. Oscillation periods in this experiment ranged from about 0.8 sec to 166 sec. When the oscillation period was considered too long (in view of potential errors due to "zero" drifts), the acquisition was terminated once a given load was observed to have obtained a desired smoothness. This was a subjective decision that depended greatly on the nonperiodic content of the signal.

In addition to the averaged data being stored for future processing, the data were automatically reduced to engineering coefficients and graphically presented in a familiar format that showed the lift, drag, and moment loads versus angle of attack. This practice of immediately displaying the results permitted a timely evaluation of the data so that any irregularity in the measurement system could be quickly exposed and corrected. It is estimated that the angle of attack of the airfoil could be measured with an accuracy of 0.5°. Lift and drag measurements are considered accurate to 0.002 lb and the pitching moments to 0.02 in-lb.

Flow Visualization

The technique for visualizing the flow was based on the release of a fluorescing dye from an orifice (0.030-in. diameter) located midspan on the leading edge of the basic VR-12 airfoil. For the extended-slat airfoil, the dye was released from orifices located on the leading edge of each element to study the slat's influence on dynamic stall. The dye solution was prepared from Rhodamine 6G and deionized water at a ratio of about 1 mg powder to 800 ml water. This aqueous solution was carried to the model through flexible tubes from a reservoir located above the water tunnel and at a sufficient height to maintain flow at all angles of attack. The dye flowed out from the surface of the airfoil and mixed with the fluid coming from the stagnation region. The mixture was then transported downstream from the leading edge by the fluid in the boundary layer and wake, thereby enabling the thickness and eventual separation of the boundary layer to be observed.

The dye appears orange under ordinary room lighting, and has a fluorescence emission that is yellow when the dye is stimulated by light at a shorter wavelength. Since a dark background offers the best contrast with yellow, the rear test-section wall was painted black and a black pigment was included in the urethane mixture when the airfoil models were cast. The dye was stimulated by two sources of light: a xenon strobe that emitted a large quantity of radiation in the ultraviolet range, and an argon-ion laser that emitted a majority of its radiation in the green and blue range.

The strobe cavity has the shape of a long tube so that the light from the xenon gas needed only to be baffled to form a sheet of light with a thickness of about 1 in. The light from the laser was carried along an optical fiber and then directed onto a mirror that was oscillating at about 120 cps. The slightly diverging beam that was reflected from the mirror formed a fan of light with nearly the same thickness as the strobe. In both cases, the light passed through the upper test-section window and straight down onto the airfoil surface. The strobe was used for the single-frame recordings that were made on Kodak TMY 6053 black and white film (ASA 400), and the laser was used for the video recordings (30 frames per sec) on Betacam-formatted film.

The flow visualization portion of the experiment was performed with the lift and drag balance removed. Values of either ωt (unsteady case) or α (steady case) were digitally displayed by light-emitting diodes that were positioned in the field of view of the camera looking into the test section.

RESULTS FROM COMPUTATIONS

For both the basic and the extended-slat airfoils, the steady and unsteady flow fields were calculated at a Reynolds number of 200,000. Steady calculations were made over a range from $\alpha = 0°$ to 30°. Unsteady calculations were made at a reduced frequency of 0.1 and for a pitching motion defined by $\alpha = 15° + 10° \sin(\omega t)$. The basic airfoil was treated as fully turbulent. The extended-slat airfoil was considered to be fully laminar over the slat and fully turbulent over the main element.

Steady Results

The computations were initiated with an impulsive start from a stagnant flow condition. A certain number of computational steps were required for the solution to reach an asymptotic state, during which time the results often appeared to oscillate. Representative examples of this behavior are shown in figure 8 for angles of attack that are both below and above the stall angle. The time histories that are shown in this figure are given in terms of the computational time, which is a nondimensional quantity. If the calculation were to begin with an initial time step of 0.01 (also a nondimensional quantity) and remain unchanged until a solution is reached after 3600 steps, then the computational time would be equal to 36. Since the code considers the chord length of the airfoil to be 3.6 units, this means that the free stream moves a distance of 10 chords during this computational time period.

Considering the lift coefficient for the basic airfoil at $\alpha = 5°$, the calculation quickly approaches an asymptotic value within a computational time of 20. Just before stall, at $\alpha = 15°$, the calculation seems to be overly damped and a computational time of at least 120 is required to reach an acceptable solution. Just after stall, as typified by the time history shown for $\alpha = 25°$, the calculation is underdamped and again requires a computational time of at least 120 to be qualified as a converged solution. The time histories for the extended-slat airfoil differ mainly in the apparent damping (all appear more damped), and all require a computational time of 120 to reach converged values.

The calculated lift, drag, and pitching-moment coefficients for the basic VR-12 airfoil are shown in figure 9 at discrete angles of attack ranging from 0° to 30°. The lift coefficient is linearly dependent on the angle of attack between 0° and 7°. Between 7° and 13°, the slope gradually decreases, indicating that the separation point is moving from the trailing edge toward the leading edge of the airfoil. Above 15° the airfoil stalls, as indicated by the rapid increases in drag and pitching moment. Although there is also an abrupt decrease in the lift at stall, the lift gradually increases with further increases in angle of attack. The calculated streamlines and surface pressure distributions are shown at 5-deg intervals in figure 10. At $\alpha = 15°$ the streamline pattern indicates that there is some separation over the aft portion of the airfoil. For $\alpha \geq 20°$ the flow is separated over a majority of the upper surface. The calculated streamlines are not at all steady when the airfoil is stalled; the particular sets that are shown were selected because they illustrate the presence of vortex-like structures that are periodically shedding into the wake.

The calculated loads for the extended-slat VR-12 airfoil at fixed angles of attack are shown in figure 11. The chord of the basic VR-12 airfoil was used as the reference length for calculating the coefficients for both the slat and the main element. Using the same reference length enables the individual contributions of the slat and the main element to be readily identified. The combined results indicate that the extended-slat airfoil stalls at around 17°. The relatively flat response of the slat for $\alpha \geq 20°$ suggests that the flow may be completely separated from this element of the airfoil. The early increase in the magnitude of the moment on the main element occurs because a majority of this part of the airfoil is aft of the pitch axis, as well as because there is an apparent shift in the center of pressure toward the trailing edge. The calculated streamlines and surface pressure distributions for the extended-slat airfoil are shown at 5-deg intervals in figure 12. These results show that a strong pressure peak is maintained near the leading edge of the slat even at high angles of attack; however, the separation from the aft portion of the slat may have coerced a separated condition on the main element.

The difference between the load coefficients of the basic and of the extended-slat airfoils is shown in figure 13. A sizable increase in the lift for the extended-slat airfoil is realized at the higher angles of attack (even after both airfoils have stalled). The stall angle for the extended-slat airfoil is delayed by about 2° compared to that of the basic airfoil; however, an undesirable increase in the magnitude of the pitching moment develops on the extended-slat airfoil after about $\alpha = 8°$.

Unsteady Results

The calculated load coefficients for the basic VR-12 airfoil are shown in figure 14 along with instantaneous streamlines at various times during the cycle of oscillation. A prominent feature in these results is the strong stall vortex that is created at around 23° and which induces a large peak in each of the loads. As shown in figure 15, the behavior of the extended-slat VR-12 airfoil is different. These results reveal that the contribution of the main element dominates each of the loads. However, there are no abrupt dynamic loads on either element, neither is there any evidence of a stall

vortex. The main element does experience flow separation from the trailing edge. The large undulation in the pitching moment that occurs around $\alpha = 10°$ may be due to the movement of the reattachment point past the pitch axis in the direction of the trailing edge. The improvement in performance of the extended-slat airfoil over that of the basic airfoil is shown more directly in figure 16. The lift hysteresis is significantly lower for the extended-slat airfoil, and the peak drag and moment loads are also reduced.

RESULTS FROM EXPERIMENT

For both the basic and the extended-slat airfoils, the steady and unsteady loads were measured at a Reynolds number of 200,000. The chord length of the basic airfoil was used as the reference length in all coefficients for the basic and the extended-slat airfoils. Steady measurements were made over a range from $\alpha = 0°$ to 30°. Unsteady measurements were made with a pitching motion defined by $\alpha = \alpha_m + 10° \sin(\omega t)$. The reduced frequency (k) was varied from 0.05 to 0.20 with constant $\alpha_m = 15°$, and the mean angle (α_m) was varied from 10° to 20° with constant $k = 0.10$. These test conditions are summarized in tables 1 and 2. The average free-stream velocity during this test was 6.5 ft/sec; the dynamic pressure was 0.28 lb/in.^{2}.

At $\alpha = 25°$ the frontal area of the basic VR-12 airfoil was 13.8% of the cross section of the test section. Some blockage effects can therefore be expected; however, wall corrections were not applied to the data. Because of tunnel blockage, the dynamic pressure varied slightly in response to the changing angle of attack of the airfoil; hence there was always some phase angle between q_∞ and α. Since the coefficients C_l, C_d, and C_m are nondimensionalized using q_∞, it was necessary to use the instantaneous value rather than the averaged value over the cycle.

The hysteresis in the load curves between $\alpha > 10°$ and $\alpha < 20°$ (fig. 17) indicates the bimodal nature of the flow near stall. The flow approaching stall (α increasing) is different from that approaching reattachment (α decreasing), even though the angle of attack may be the same. Hysteresis loops are a result of aerodynamic bifurcations (ref. 5) and may even occur for angles of attack below stall (ref. 6). The small fluctuations between $\omega t = 0°$ and $\omega t = 180°$ illustrate what happens when there is random formation and shedding of secondary structures and when only a few cycles are used to ensemble average the data (in this case only five cycles were used).

Basic VR-12 Airfoil

Steady results– The measured loads for the basic airfoil at fixed angles of attack are shown in figure 18. The lift curve is fairly linear up to $\alpha = 8°$, after which the slope decreases due to increasing separation over the aft portion of the airfoil. The increase in separated flow over the upper surface also contributes to an increase in drag. While on the upper surface the pressure decreases near the leading edge and increases near the trailing edge (which increases even further due to separation), each invoking a positive moment, the increase in pressure over the lower surface appears to be dominant, resulting in a net shift in the center of pressure toward the trailing edge and an increase in the magnitude of the pitching moment. Between 17° and 18° an abrupt change in all the loads occurs, signaling that the airfoil has stalled.

The abrupt stall exhibited by the loads was also observed in the flow visualizations. The sequence shown in figure 19 reveals that the separation point is advancing from the trailing edge when suddenly, at $\alpha = 17°$, the flow over the upper surface of the airfoil fully separates. There is an estimated $1/2°$ installation error between the load and the visualization setups. The fact that the VR-12 has an upper surface that is much flatter than that of the VR-7 airfoil may account for the significantly more abrupt stall than was observed in the latter case in an earlier study (ref. 1).

Figure 20 shows the comparison between the steady (increasing α only) and the quasi-steady cases (full cycle of oscillation). Even though the frequency of oscillation was quite low (the time period to complete one cycle was about 63 sec), the flow was sufficiently unsteady to cause a delay in the stall angle. However, outside the hysteresis boundary the steady and quasi-steady values are nearly identical.

Unsteady results– The case for $\alpha = 15° + 10° \sin(\omega t)$ and $k = 0.1$ was selected for extensive experimental study and for comparison with the calculations. The measured loads are shown in figure 21, and the corresponding flow visualizations are shown in figures 22 (featuring the complete cycle) and 23 (focusing on the stall vortex). For $\dot{\alpha} > 0$ the flow is attached and the lift increases rapidly with only a modest amount of separation near the trailing edge

as the airfoil passes $\omega t = -45°$ ($\alpha = 8°$). Around $\omega t = 0°$ ($\alpha = 15°$) the separation point on the upper surface moves up the airfoil and causes the slope of the lift curve to noticeably decrease. At about $\omega t = 35°$ ($\alpha = 21°$) a vortex forms near the leading edge. After reaching $\omega t = 45°$ ($\alpha = 22°$) the flow is fully separated from the upper surface and the stall vortex has moved halfway down the airfoil. At this point the lift, drag, and pitching moment are all rapidly increasing in magnitude. At $\omega t = 90°$ ($\alpha = 25°$), the vortex moves into the wake and all of the loads quickly decrease in magnitude. When $\dot{\alpha} < 0$ the reattachment point slowly moves away from the leading edge and over the upper surface of the airfoil. The "hump" in the pitching moment curve around $\omega t = 225°$ ($\alpha = 8°$) corresponds to the movement of the reattachment point past the quarter-chord pitch axis.

Figure 23 shows more precisely the events associated with the development of the dynamic-stall vortex. At $\omega t = 34°$, the separation point has moved forward to about $x/c = 0.3$; however, a condition of flow reversal exists along the entire upper surface of the airfoil. Whereas it has taken an increase in ωt of at least 35° for the separation point to move from the trailing edge to this point, it now takes only 1° for the airfoil to completely separate over the upper surface and a stall vortex to emerge near the leading edge. As ωt increases over the next 15 degrees, the separated flow over the airfoil appears to be organized into numerous large-scale structures. However, the stall vortex is not as clearly identifiable as it has been on other airfoils (e.g., the VR-7). A vortex appears to be passing the quarter-chord location (which is the pitch axis) at $\omega t = 52°$ and would account for the double inflection in the moment curve that occurs at the same azimuth. The same vortex was observed in the video to move past the trailing edge and into the wake behind the airfoil at $\omega t = 72°$, which is coincident with the sudden decrease in the magnitude of the lift, drag, and moment loads. The marked change in the pitching moment at $\omega t = 235°$ is caused by the reattachment of the flow to the airfoil just as the point of reattachment moves past the pitch axis.

The loads were also measured at other reduced frequencies and mean angles. The results for $k = 0.05 \rightarrow 0.20$ at a fixed mean angle (α_m) of 15° are shown in figures 24 and 25. Several characteristics associated with the stall process can be quantized to show the influence of k. At $k = 0.05$ the maximum rate of change with respect to α of both the lift and drag occurs at $\omega t = 40°$. Over the range of $k = 0.05 \rightarrow 0.20$ these events are delayed by $\Delta(\omega t) = 27°$. At $k = 0.05$ the peak value of lift is reached at $\omega t = 45°$. Over the range of $k = 0.05 \rightarrow 0.20$ this peak was delayed by $\Delta(\omega t) = 26°$. At $k = 0.05$ the stall vortex passes over the quarter-chord location at $\omega t = 44°$, as indicated by the double inflection in the moment curve. Over the range of $k = 0.05 \rightarrow 0.20$ this event is delayed by $\Delta(\omega t) = 33°$. The movement of the stall vortex across the pitch axis appears to be a linear function of k, having a slope given by $\mathrm{d}\omega t/\mathrm{d}k = 220°$. Increasing k also causes a broadening of the hysteresis amplitude for each of the load coefficients and a delay in the angle at which the airfoil recovers from stall. The influence of the mean angle of oscillation was examined over the range $\alpha_m = 10° \rightarrow 20°$ at a fixed reduced frequency (k) of 0.10. These results are presented in figures 26 and 27 and show a progressive delay in the stall, an increase in the maximum loads, and a broadening of the hysteresis loops.

Extended-Slat VR-12 Airfoil

Steady results– The quasi-steady behavior of the extended-slat airfoil is shown in figure 28 for $\alpha = 15° + 15° \sin(\omega t)$ and $k = 0.003$. A slight deviation in the loads near $\alpha = 0°$ is most likely due to the movement of the stagnation point around the leading edge of the slat and a sudden increase in the flow between the slat and the main element. Between $\alpha = 1°$ and $\alpha = 12°$ the lift varies linearly with α. All of the loads exhibit a steady increase with angle of attack until reaching about $\alpha = 22°$, at which time the airfoil experiences an abrupt stall. Within the angle range of $\alpha = 0° \rightarrow 30°$, a hysteresis occurs between $\alpha = 17°$ and $\alpha = 26°$.

The measured loads at fixed angles of attack are presented in figure 29. The variation of the loads with α are similar to those obtained for the quasi-steady case, except the stall angle occurs between $\alpha = 20°$ and 21° in the steady case. Visualizations of the flow (fig. 30) indicate that the flow is attached over most of the airfoil for $\alpha < 10°$. At $\alpha = 15°$, the boundary layer is considerably thicker and some amount of separated flow is present over the aft portion of the airfoil. This condition no doubt accounts for the decrease in the slope of the lift curve. At $\alpha = 20°$ the separation point has moved farther up the airfoil, but the confluent boundary layers from the slat and the main element remain well defined over the forward portion

of the airfoil. Consistent with the static-load measurements, an increase of only 1° to $\alpha = 21°$ causes the flow to completely separate from the main element. At this angle the flow over a major portion of the slat has separated, although the slat does not fully separate until $\alpha = 25°$.

A comparison between the steady and the quasi-steady ($k = 0.003$) loads is given in figure 31. These results show that a small amount of unsteadiness is sufficient to cause a delay in stall. Steady data for decreasing values of α from an initially stalled condition were not obtained, but some hysteresis would be expected.

Unsteady results– Unsteady loads were measured for the same range of conditions as for the basic airfoil. The results for the standard case of $\alpha = 15° + 10° \sin(\omega t)$ and $k = 0.10$ are shown in figure 32. The large hysteresis in the lift and the rapid increases in the drag and pitching moment near $\alpha = 24°$ indicate that the slat does not prevent the airfoil from stalling over this α range. This is further confirmed by the flow visualizations shown in figures 33 (featuring the complete cycle) and 34 (focusing on the stall). For increasing α, the flow is attached; the lift smoothly increases with no appreciable separation on the airfoil as it passes $\omega t = 0°$ ($\alpha = 15°$). At $\omega t = 45°$ ($\alpha = 22°$), the separation point on the upper surface has moved up to about $x/c = 0.6$ and is accompanied by a noticeable decline in the slope of the lift curve. At $\omega t = 90°$ the flow has fully separated and the drag and pitching moment loads are near their maximum values. Over the remainder of the cycle, the reattachment point slowly moves toward the trailing edge. A brief, positive-going surge in the moment curve occurs at $\omega t = 180°$ when the reattachment point moves past the quarter-chord pitch axis.

Figure 34 shows the stall development in greater detail. At $\omega t = 64°$ ($\alpha = 24°$) the boundary layer appears to be quite thick and possibly separated at $x/c = 0.45$. The lift variation with α has already greatly decreased, and the magnitudes of the drag and pitching moment are rapidly increasing. Over the next 6 degrees (from $\omega t = 64°$ to 70°) a significant portion of the flow on the slat appears to be separating, and large-scale structures appear over the main element. During the next 13 degrees (from $\omega t = 70°$ to 83°) the visualizations indicate that a stall vortex may be developing over the forward 25% of the airfoil. At $\omega t = 83°$ the vortex appears to be passing the $x/c = 0.25$ location and is coincident with the maximum drag and pitching moment loads. At $\omega t = 182°$ the reattachment point has just moved past the quarter-chord pitch axis.

The influence of the reduced frequency was studied over the range of $k = 0.05 \rightarrow 0.20$ for $\alpha = 15° + 10° \sin(\omega t)$. The results are presented in figures 35 and 36 and show that the stall is progressively delayed and that the hysteresis amplitudes of all the loads increase with k, especially those for the lift and the pitching moment. The damping in pitch also increases with k, primarily due to the large positive moment that develops during the reattachment phase of the cycle. The mean angle of oscillation was varied from 10° to 20° with $k = 0.10$. As shown in figures 37 and 38, increasing the mean angle forces the airfoil to oscillate through more extended periods of separated flow, thereby substantially increasing the hysteresis amplitudes. Increasing α_m causes all of the loads to reach higher maximum values and the stall to occur at progressively lower values of ωt. The momentary surge in the loads around $\omega t = 85°$ in the $\alpha_m = 20°$ case may be due to the passage of a stall vortex over the surface of the airfoil.

Contrast in Performance

A summary of the measured loads for the basic and extended-slat airfoils is shown in figure 39. The most noticeable difference between the two airfoils is in the pre-stall slope of the pitching-moment curve. The slope for the extended-slat airfoil is much less than that for the basic airfoil and is probably due to the thinner boundary layer over the main element, which in turn is a result of the energizing effect of the flow from the passage between the slat and the main element. Another difference occurs in the lift at the lower frequencies. The surge in the lift that develops after $\alpha = 20°$ on the basic airfoil is only faintly present on the extended-slat airfoil. Furthermore, a longer period of time is required to recover from stall with the basic airfoil (as evidenced by the hysteresis loop) than with the extended-slat airfoil (which begins to close around $\alpha = 17°$).

To compare more directly, the measured steady and unsteady loads are shown in figure 40 for the basic and extended-slat airfoils. The differences between the two airfoils are readily discernable in the unsteady case in terms of the lift surge, the extent of the lift hysteresis, and level of the pitching moment. Clear evidence has

already been established that a stall vortex is present on the basic airfoil when $\alpha = 15° + 10° \sin(\omega t)$, which would account for the higher drag and moment peaks. In the steady case the major difference is the delay in the angle of stall, which is about 3° in favor of the extended-slat airfoil. Overall, the unsteady and steady results both show that the performance of the extended-slat airfoil is superior to that of the basic airfoil. Another way of evaluating the success of the slat is in terms of lift/drag (fig. 41). In the unsteady case, the the average value of lift/drag is about 10% higher for the extended-slat airfoil. In the steady case, the extended-slat airfoil has a higher value of lift/drag once the basic airfoil has stalled (at around $\alpha = 17°$). Prior to stall, the basic airfoil has a higher lift/drag in the steady case due to the slightly lower drag that exists over this α range. The difference is greatly amplified because the drag for the basic airfoil is close to zero. Figure 42 shows that if the airfoil oscillation occurs over the higher angles of attack, then the lift/drag will be higher on the extended-slat airfoil for all values of k.

Since the results that have been presented were obtained at $Re = 200,000$ (which means that the slat Reynolds number was only about 20,000) and in a nearly incompressible medium, it is reasonable to question what differences might appear in data obtained at higher values of Re and M_∞. Although no other data exist for the extended-slat configuration, steady data (obtained with a balance) for the VR-12 airfoil are available at the condition of $Re = 4,000,000$ and $M_\infty = 0.3$ (ref. 7). The steady loads that were measured in the water tunnel are compared with these wind tunnel data in figure 43. Both sets of data show a similar trend in the variation of lift with angle of attack. Following an initial linear response as α increases, the lift-curve slope begins to decrease until reaching the stall angle. In both cases the stall is abrupt and the angle of stall agrees within 1°. The primary differences between the two sets of data are in terms of the maximum value of lift (lower in the present experiment) and the pre-stall drag and moment curve slopes (higher in the present experiment).

ACCURACY OF THE CODE

The measured and calculated loads are compared in figure 44 for the steady results and in figure 45 for the unsteady results. In the steady case the best agreement between the measured and calculated results is in the lift for the basic airfoil, although the stall is prematurely predicted by the calculations by several degrees. The calculations also underpredict the magnitudes of the drag and of the pitching moment. The results for the extended-slat case are in greater disagreement. In addition to the premature stall, the calculations give a much higher value of lift than was measured, and the magnitude of the pitching moment rapidly increases (in a nose-down direction) well before stall (starting around $\alpha = 8°$).

In the unsteady case (fig. 45) the calculated loads on the basic airfoil appear to be overly responsive to the various flow events occurring during the stall and the reattachment portions of the cycle. This is evident from the large and numerous undulations in all the loads. The calculations for the basic airfoil show a fairly linear variation with α prior to stall. Unlike the steady calculation for the basic airfoil, the unsteady calculation indicates a stall angle that is several degrees higher than the measured results, and all of the peak loads are higher as well. The higher peak loads are probably due to an excessively strong stall vortex. The calculated peak loads on the extended-slat airfoil are much less than those calculated on the basic airfoil, but they are still not in good agreement with the measured values. In general, the unsteady calculations correctly indicate that the extended-slat airfoil performs better than the basic airfoil, but the quantitative disagreement with the measured results suggests that the model needs to be improved.

At this time it is not known which parameters should be modified to obtain more accurate solutions, since improvements are clearly needed in both the steady and unsteady flow cases as well as for both the single-element and the two-element airfoil configurations. Historically, all turbulence models have been suspect in flows that are either unsteady or involve a separated region, both of which are present in this study.

CONCLUDING REMARKS

The focus to this study was to determine the effect of an extendable slat on both the static and dynamic stall behavior of a VR-12 airfoil. The measurements that were obtained also provided a basis for evaluating the accuracy of a design code that was developed for two-element airfoil configurations. All of the results

are for an incompressible flow at a Reynolds number of 200,000. The major concluding remarks are as follows:

1. The addition of an extendable leading-edge slat on a VR-12 airfoil delays the static stall by about 3° and reduces the development of a dynamic-stall vortex during high-amplitude pitching motions. A significant amount of trailing-edge separation was present in both steady and unsteady cases, whether or not the slat was extended.

2. At fixed angles of attack, the slat causes higher values of lift/drag to occur when $\alpha > 17°$. When the airfoil undergoes a pitching motion and $\alpha_m > 13°$, the average value of lift/drag for the extended-slat airfoil becomes increasingly higher than that for the basic airfoil as k increases.

3. The ZETA code correctly indicated a qualitative improvement in the performance of the extended-slat airfoil over that of the basic airfoil. However, the measured and calculated results are generally not in good agreement, and some improvements (most likely in the turbulence model) are clearly needed.

REFERENCES

1. McAlister, K .W.; and Tung, C.: Suppression of Dynamic Stall with a Leading-Edge Slat on a VR-7 Airfoil. NASA TP-3357.

2. Lachmann, G. V.: Sir Frederick Handley Page, The Man and his Work. Journal of the Royal Aeronautical Society, vol. 68, no. 643, 1964, pp. 433–452.

3. Tung, C; McAlister, K. W.; and Wang, C. M.: Dynamic Stall Study of a Multi-Element Airfoil. 18th European Rotorcraft Forum, Paper No. 9, Avignon, France, 1992.

4. Wang, C. M.; Wu, J. C.; and Tung, C.: A Numerical Study of General Viscous Flows Around Multi-Element Airfoils. AIAA Paper 90-0572, January 1990.

5. Tobak, M.; and Chapman, G. T.: Nonlinear Problems in Flight Dynamics Involving Aerodynamic Bifurcations. NASA TM-86706, 1985.

6. Selig, M. S.: The Design of Airfoils at Low Reynolds Numbers. AIAA 23rd Aerospace Sciences Meeting, AIAA Paper 85-0074, Reno, Nevada, January 1985.

7. Dadone, L. U.: EGCLM962 Balance Data for Boeing Vertol VR-12 Airfoil, private communication, July 1992.

Table 1. VR-12 steady data at Re = 200,000

Frame		
Without slat	With slat	α
30054	30297	0°
	30301	1°
30057	30304	2°
30060	30307	4°
30063	30310	6°
30066	30313	8°
30069	30316	10°
30072	30319	12°
30075	30322	14°
30078		15°
30084	30325	16°
30087		17°
30090	30328	18°
30093	30331	19°
30096	30333	20°
30099	30337	21°
30102	30340	22°
30105	30343	23°
30108	30346	24°
	30349	25°
30111	30352	26°
30114	30355	28°
30117	30358	30°

Table 2. VR-12 unsteady data at Re = 200,000

Frame					
Without slat	With slat	Cycles averaged	Mean angle	Amplitude	k
30004	30366	100	15	10	0.05
30006	30364	100	15	10	0.10
30010	30368	100	15	10	0.15
30013	30370	100	15	10	0.20
30025	30375	100	10	10	0.10
30046	30381	100	20	10	0.10
30052	30295	5	15	15	0.003

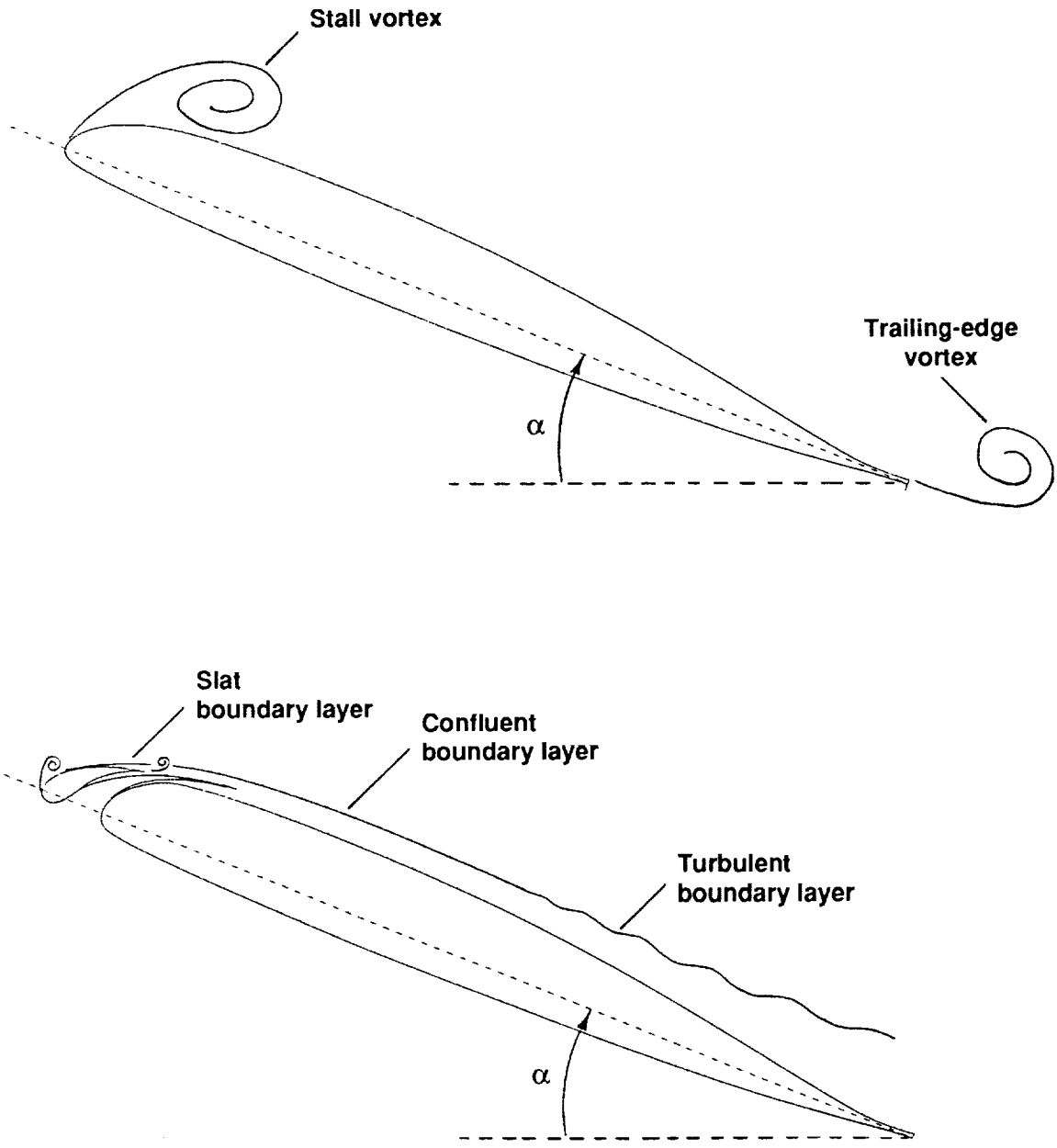

Figure 1. Boundary-layer development and vortex shedding from airfoil undergoing a pitching motion.

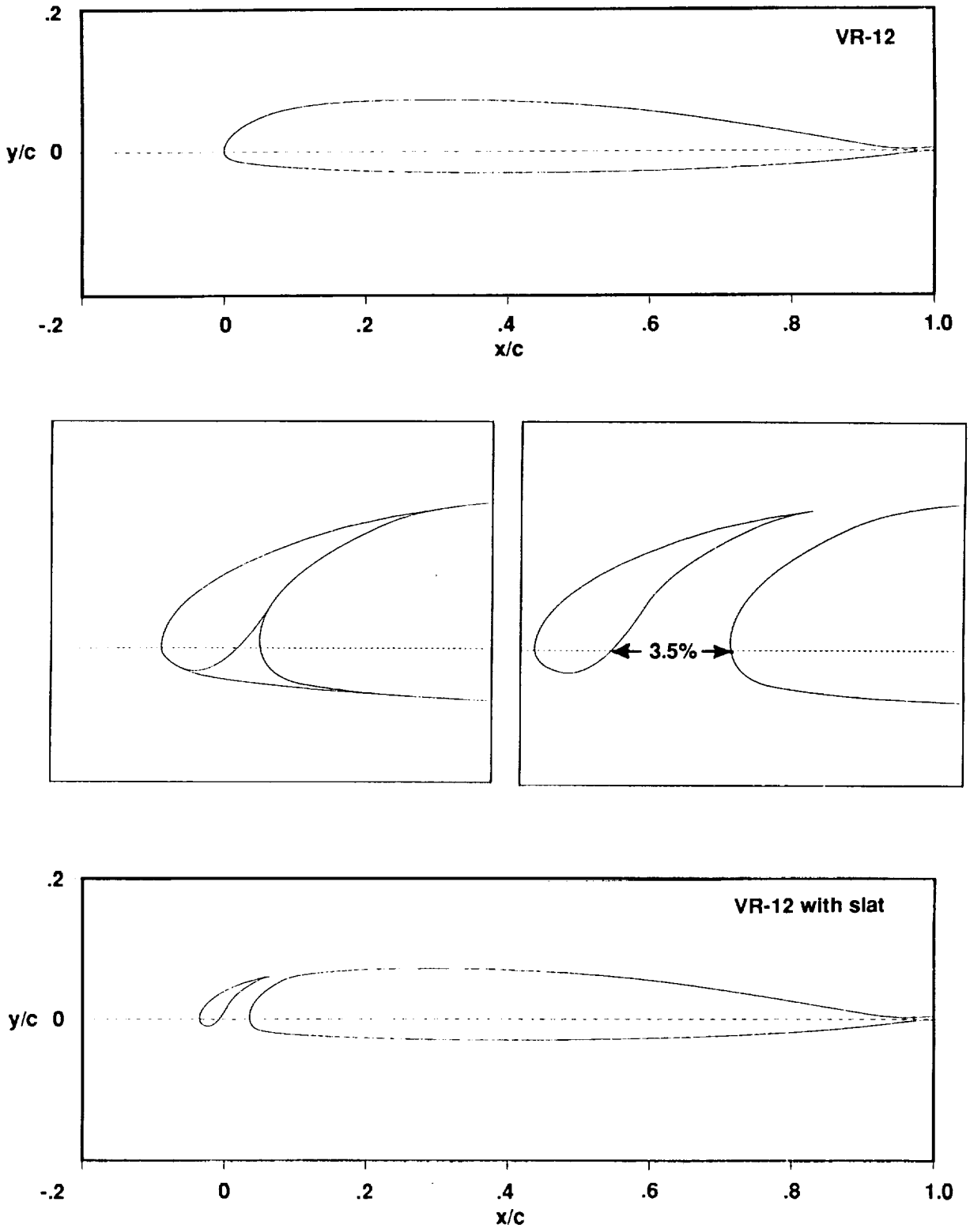

Figure 2. VR-12 airfoil with and without slat extension.

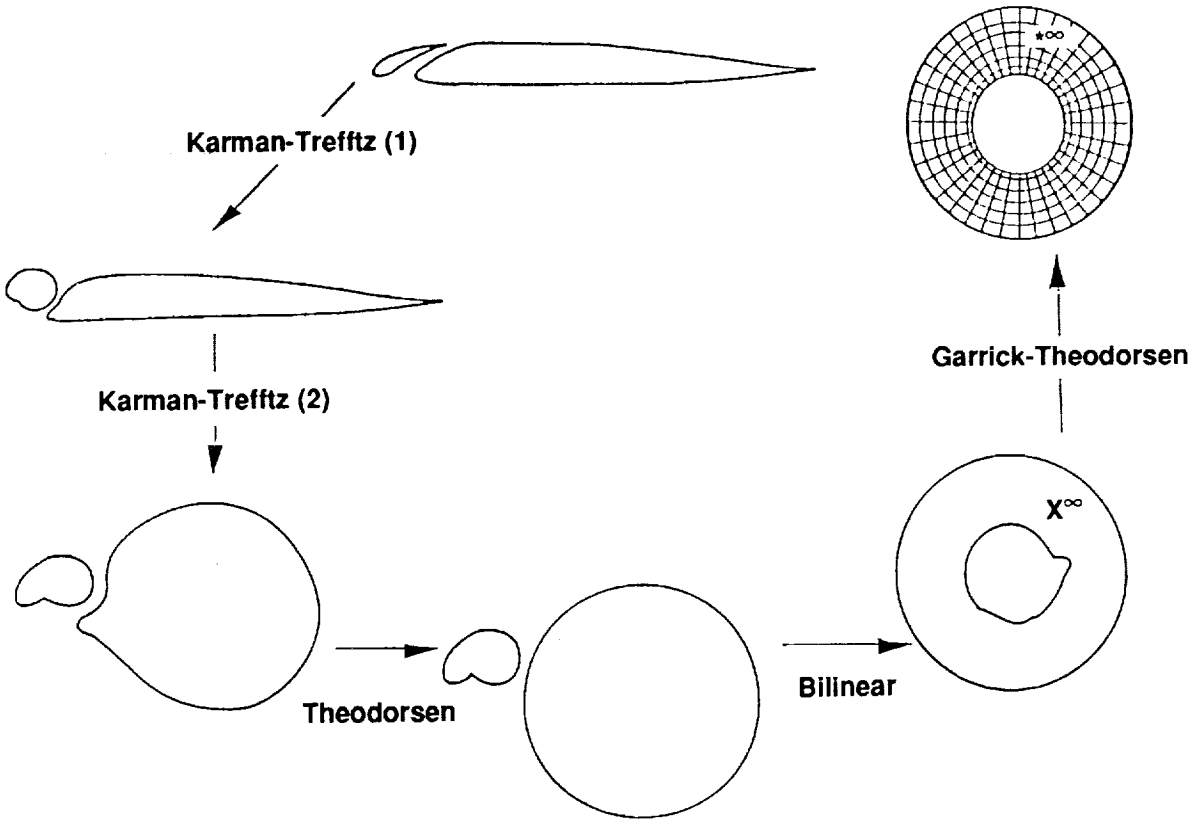

Figure 3. Transformation from physical domain to computational domain.

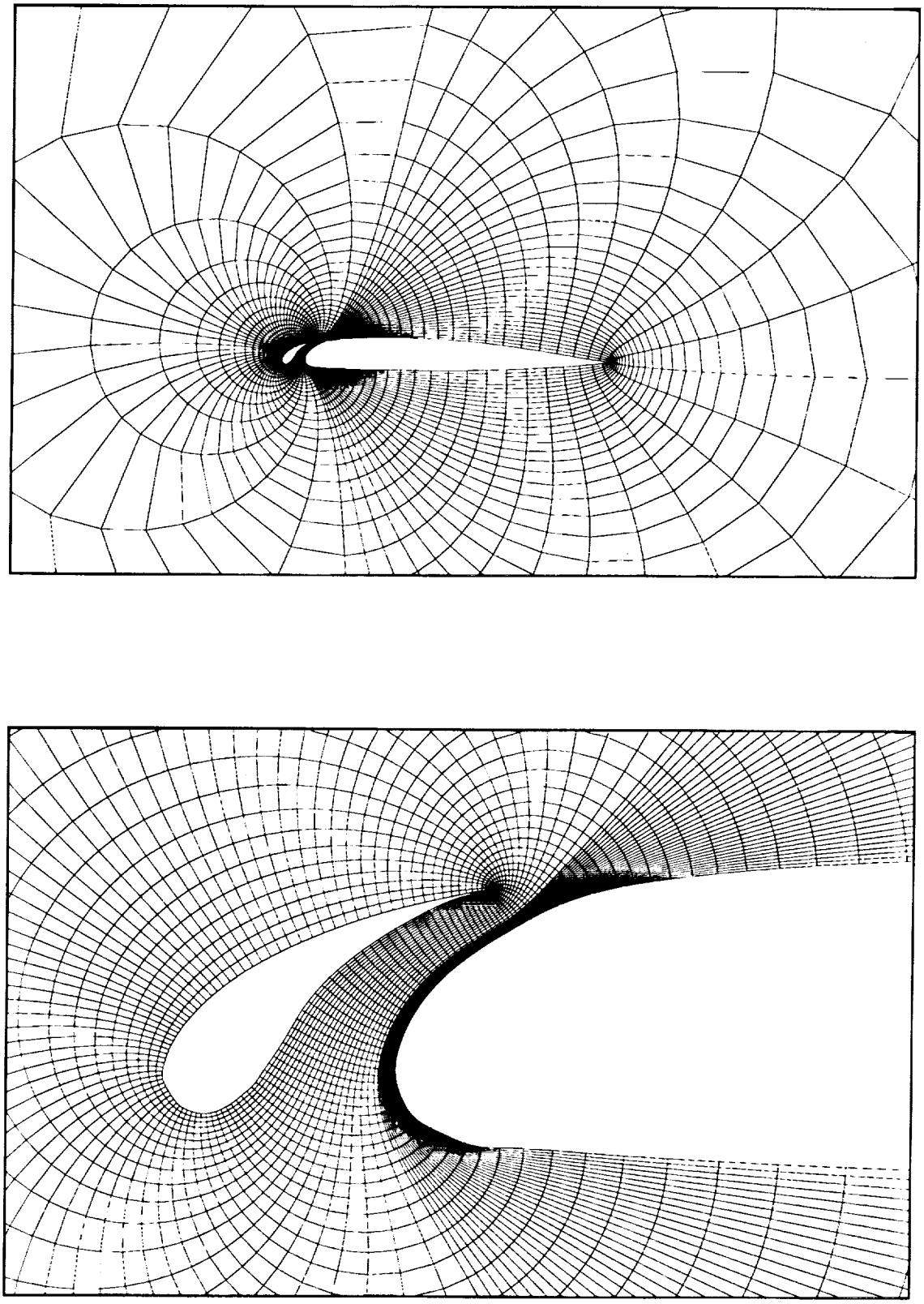

Figure 4. Computational grid in the physical domain.

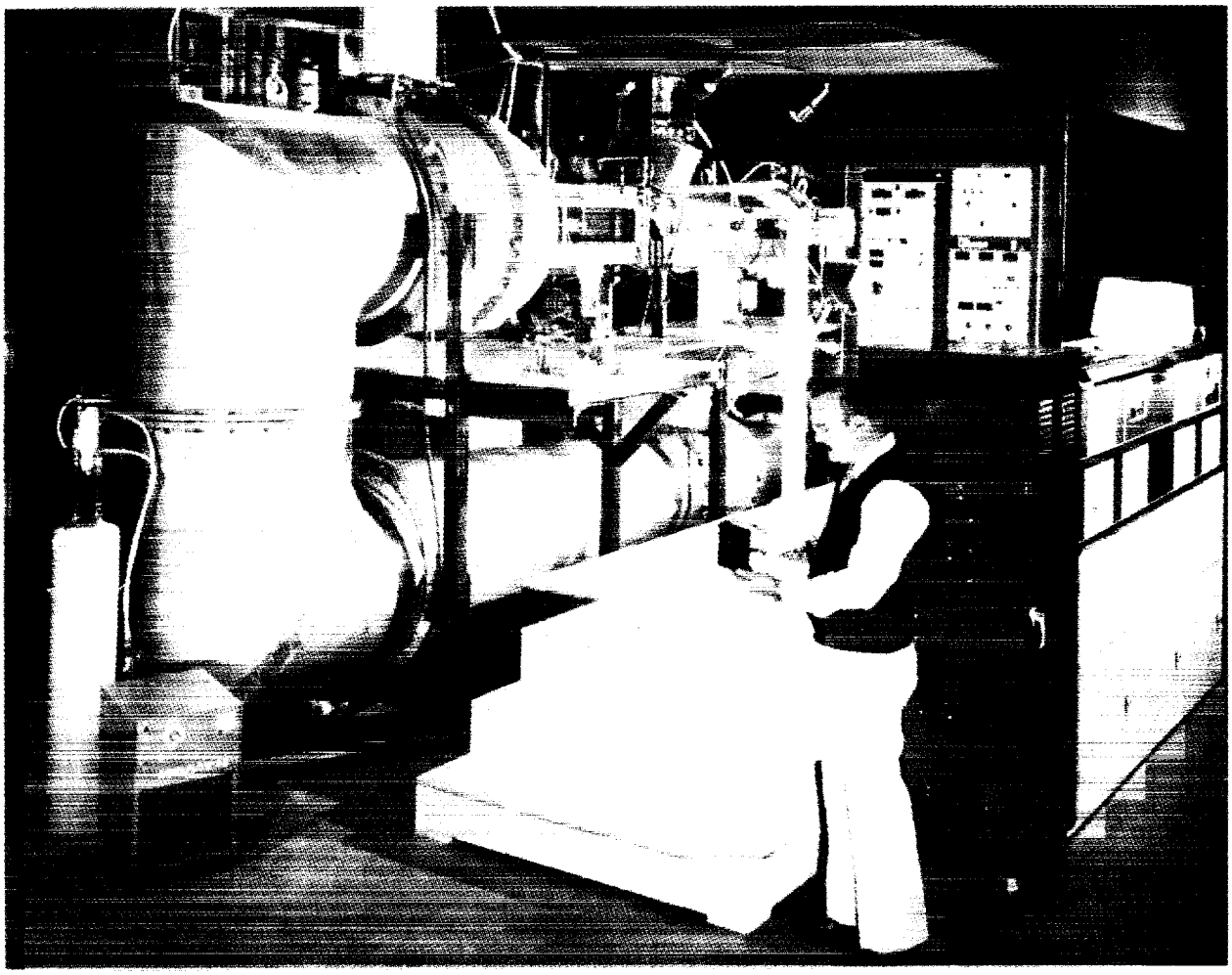

Figure 5. Aeroflightdynamics 8- by 12-in. water tunnel at Ames Research Center.

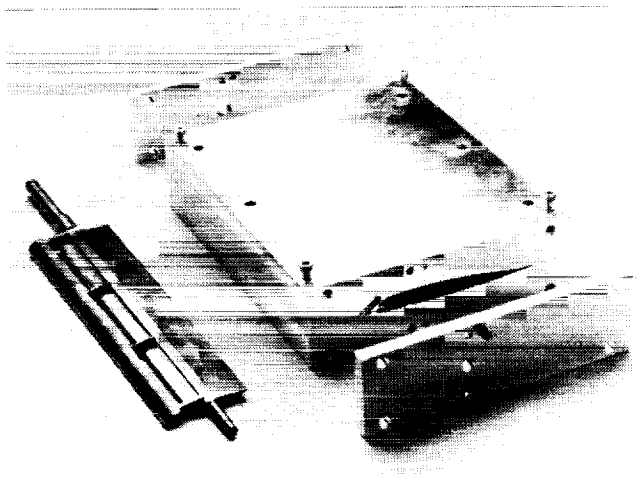

Figure 6. Slat and spar assembly alongside mold for extended-slat VR-12 airfoil.

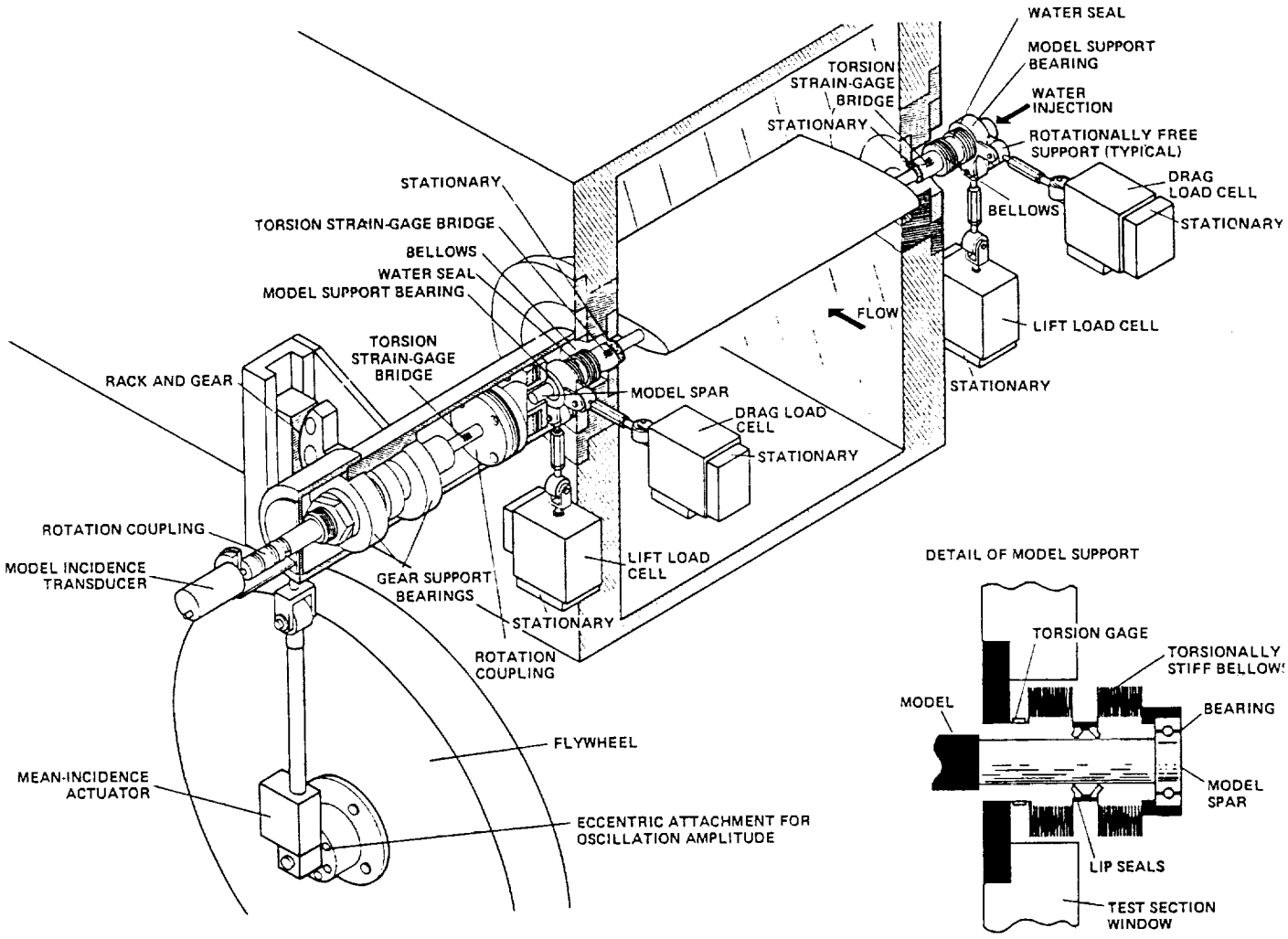

Figure 7. Model installation and balance system for force and moment measurements.

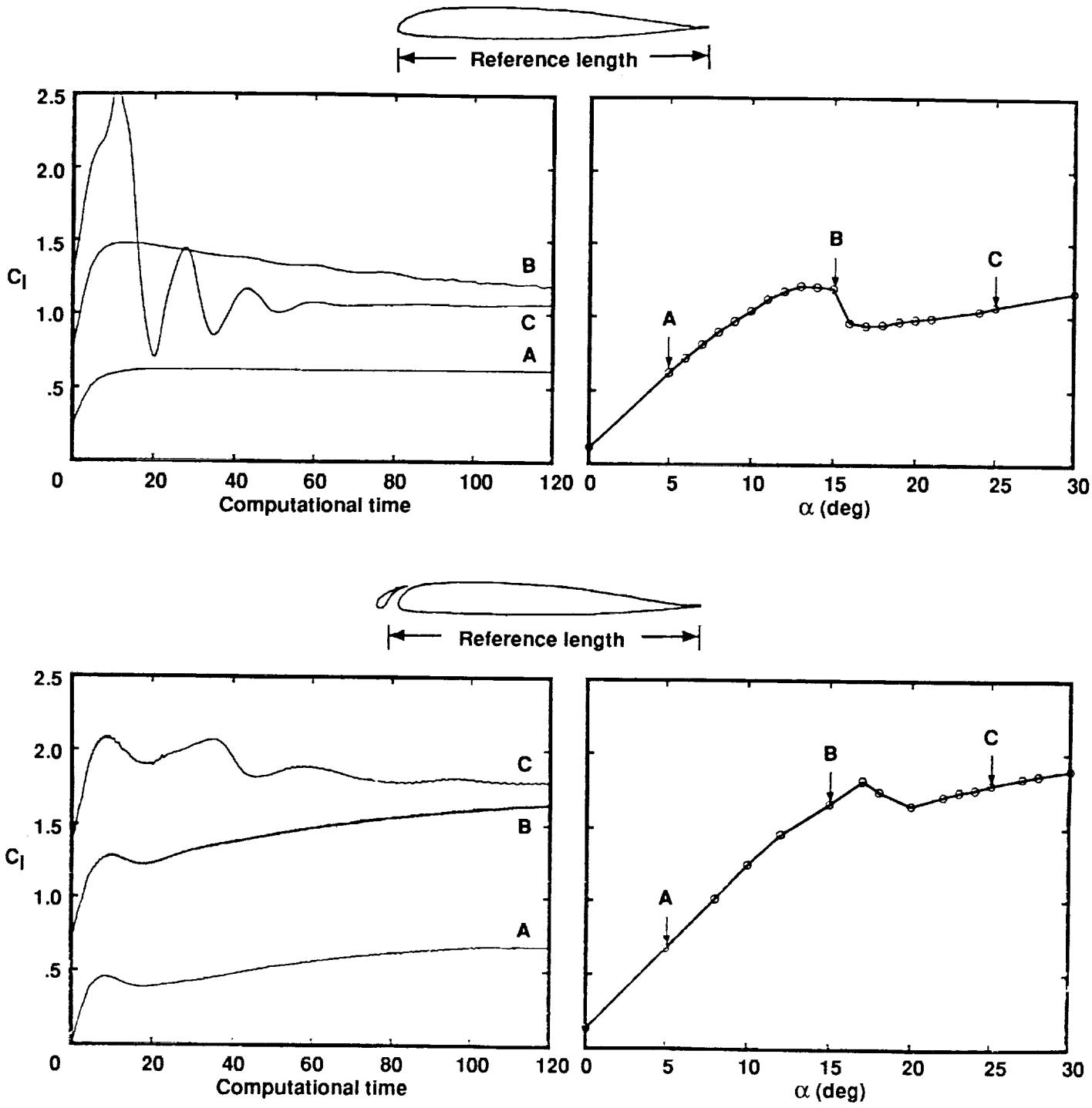

Figure 8. Time history of lift coefficient as asymptotic values are approached at three different angles of attack.

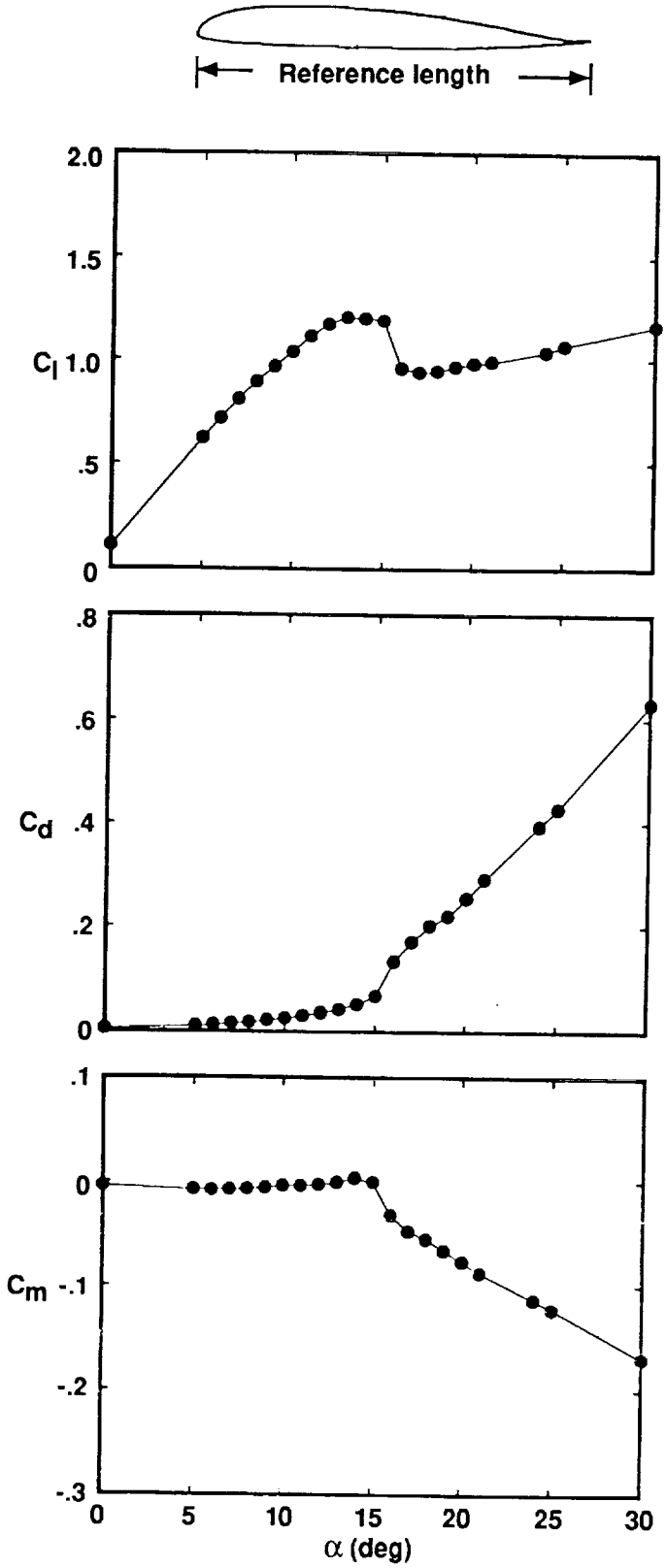

Figure 9. Calculated loads for the basic VR-12 airfoil at fixed angles of attack.

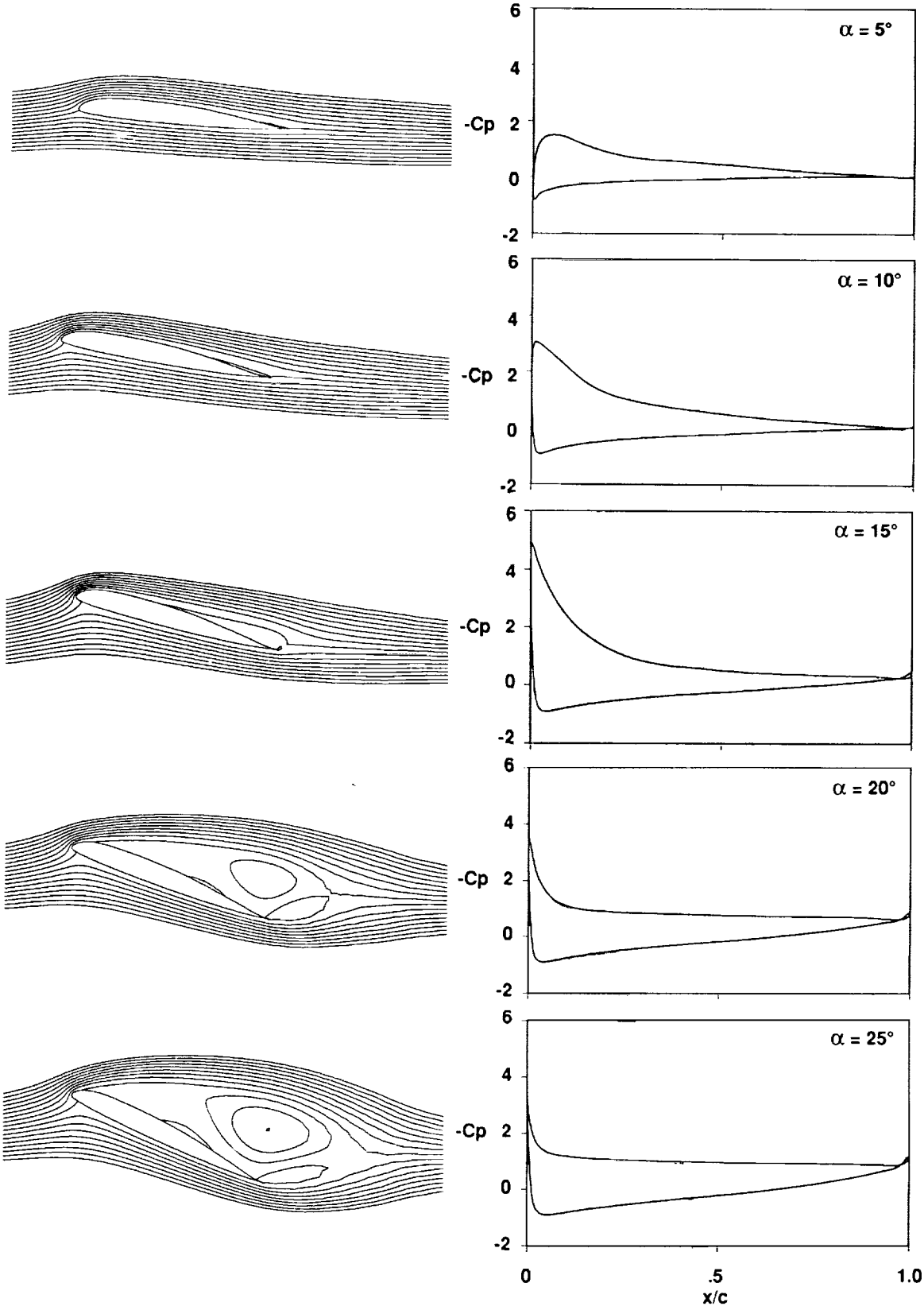

Figure 10. Calculated streamlines and surface pressures for the basic VR-12 airfoil at fixed angles of attack.

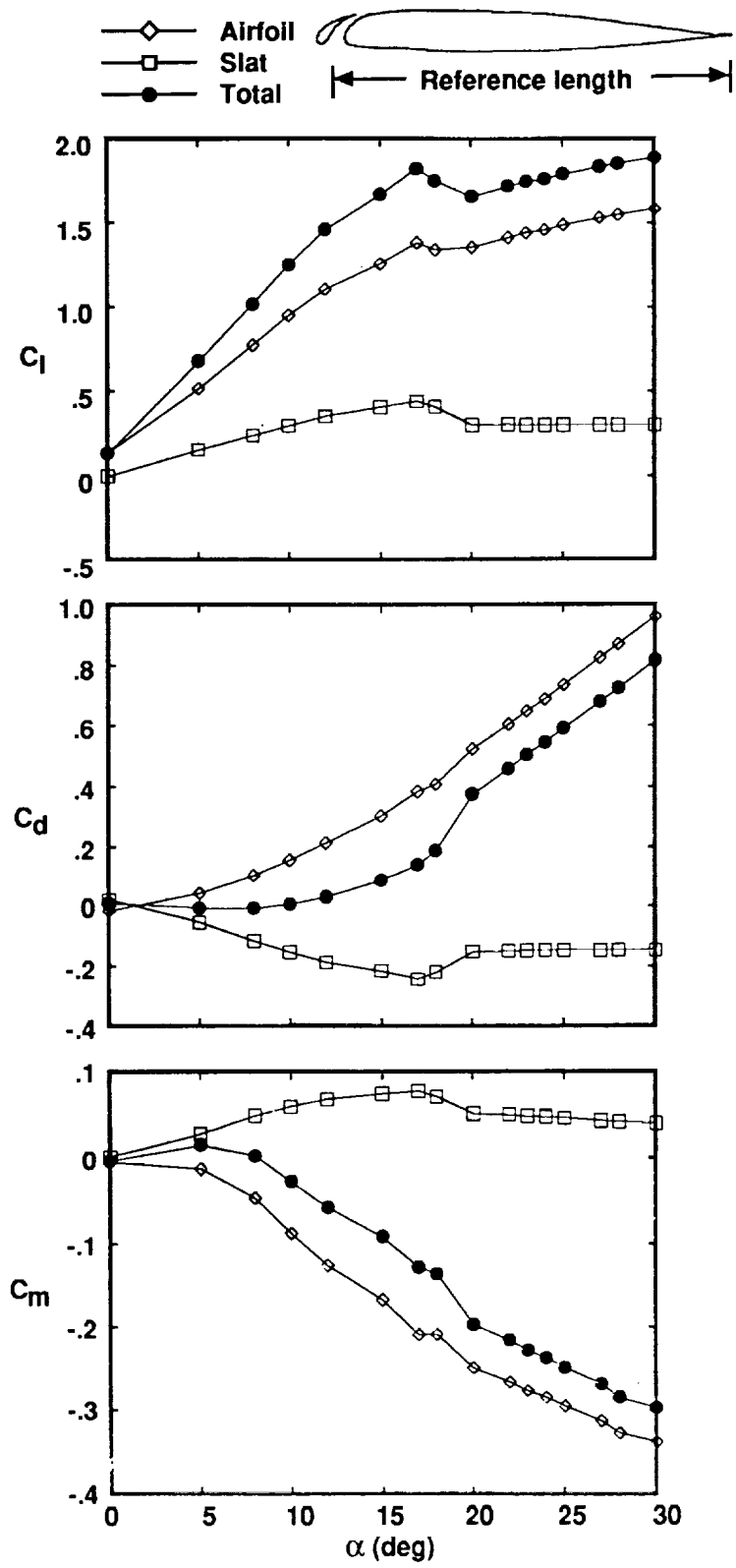

Figure 11. Calculated loads for the extended-slat VR-12 airfoil at fixed angles of attack.

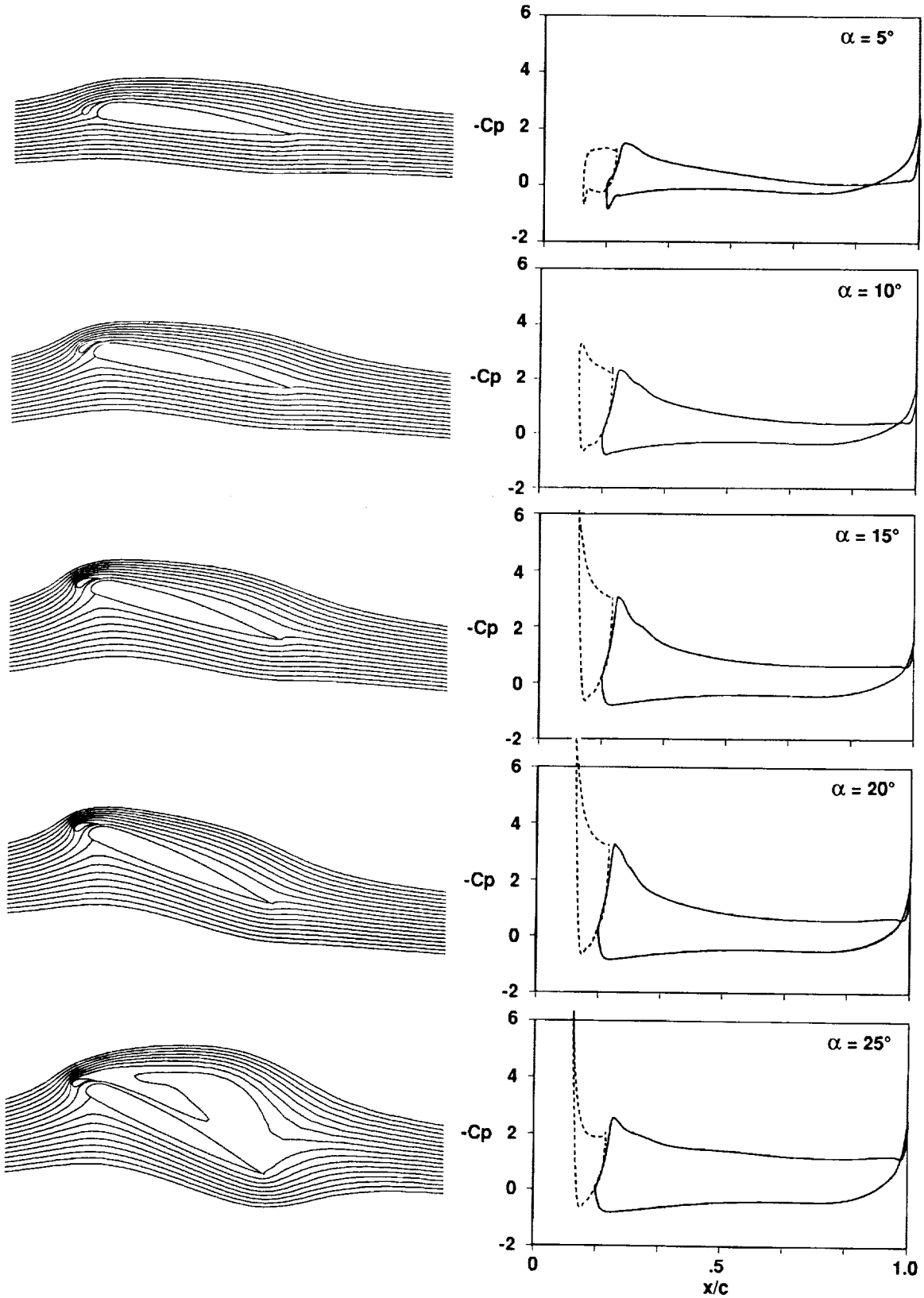

Figure 12. Calculated streamlines and surface pressures for the extended-slat VR-12 airfoil at fixed angles of attack.

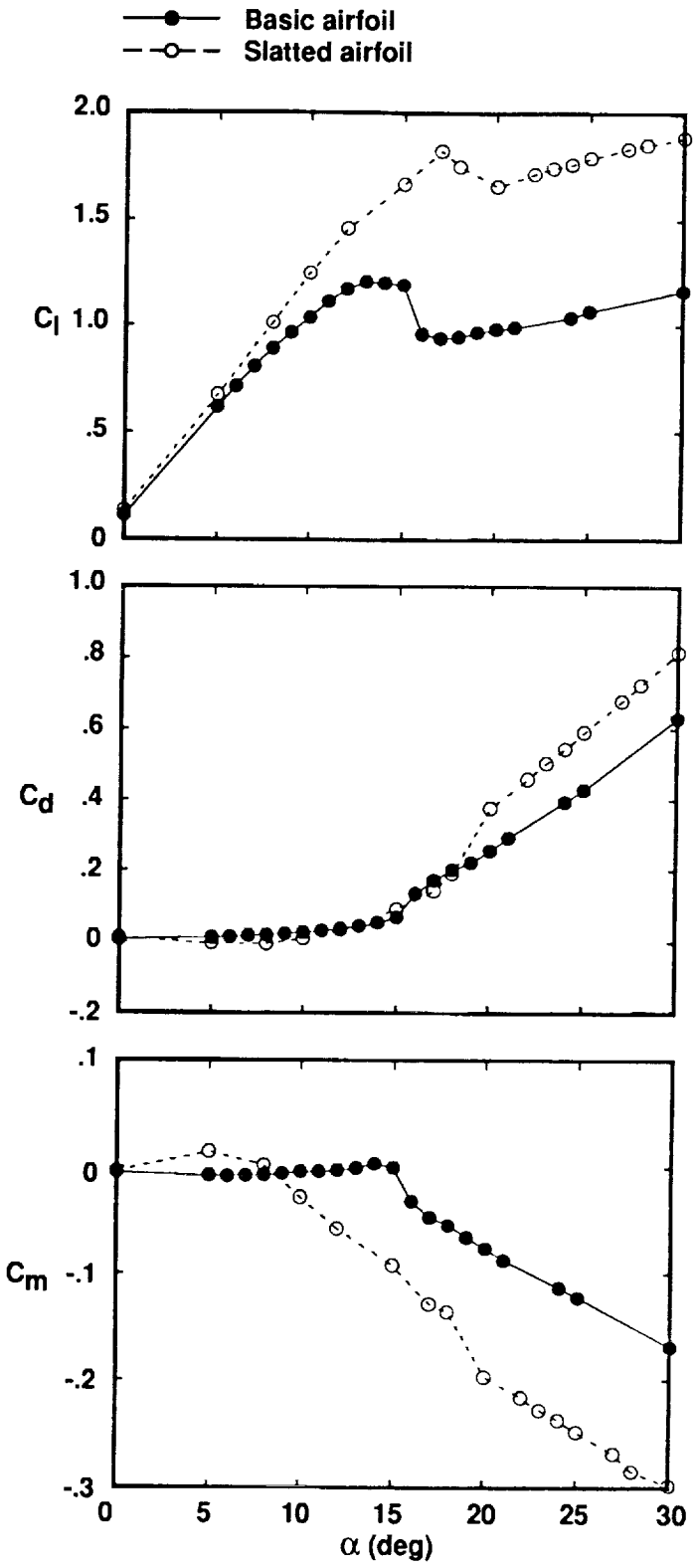

Figure 13. Comparison of the calculated loads at fixed angles of attack for the basic and extended-slat airfoils.

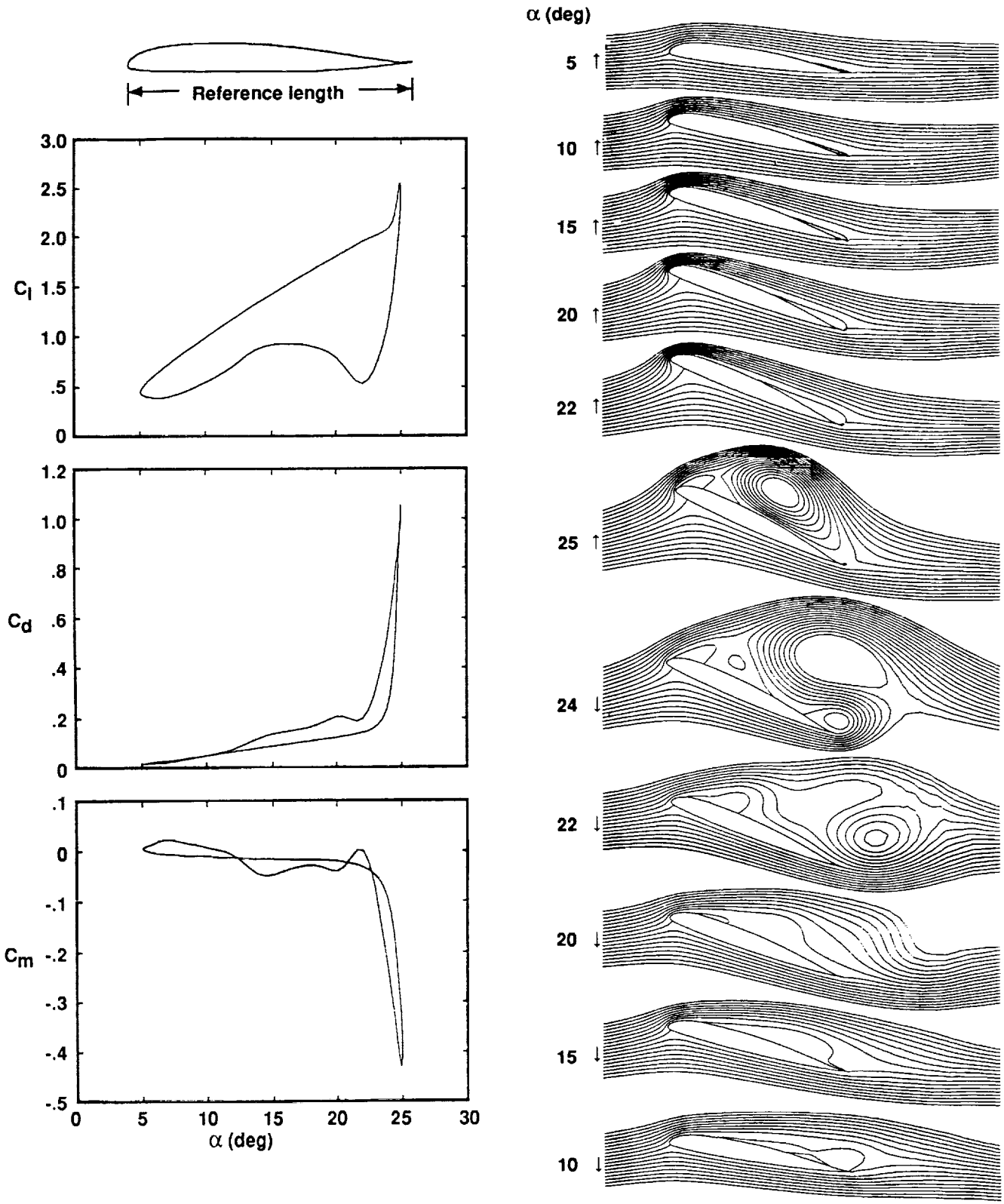

Figure 14. Calculated loads and instantaneous streamlines for the basic VR-12 airfoil with $\alpha = 15° + 10° \sin(\omega t)$ and $k = 0.1$.

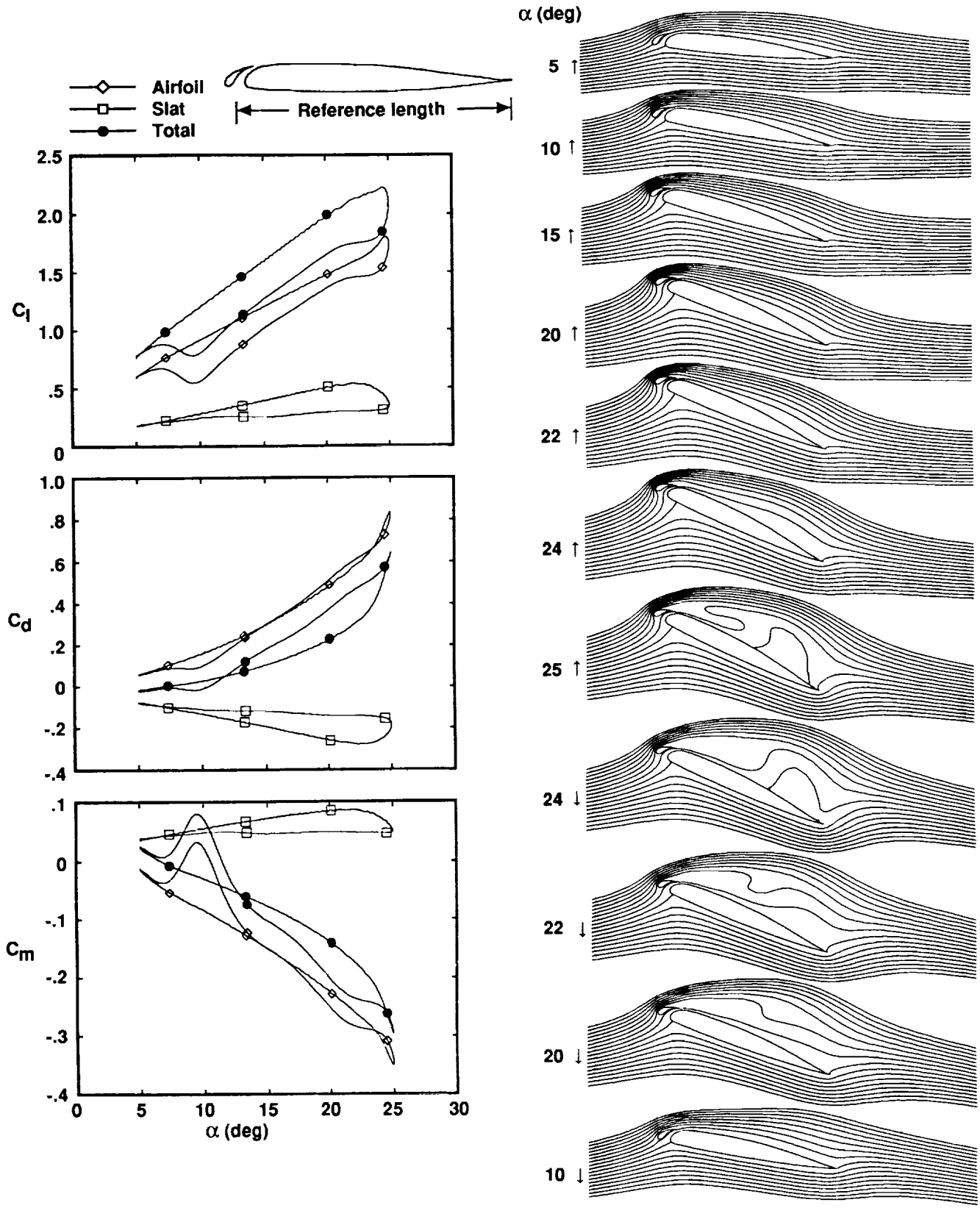

Figure 15. Calculated loads and instantaneous streamlines for the extended-slat VR-12 airfoil with $\alpha = 15° + 10° \sin(\omega t)$ and $k = 0.1$.

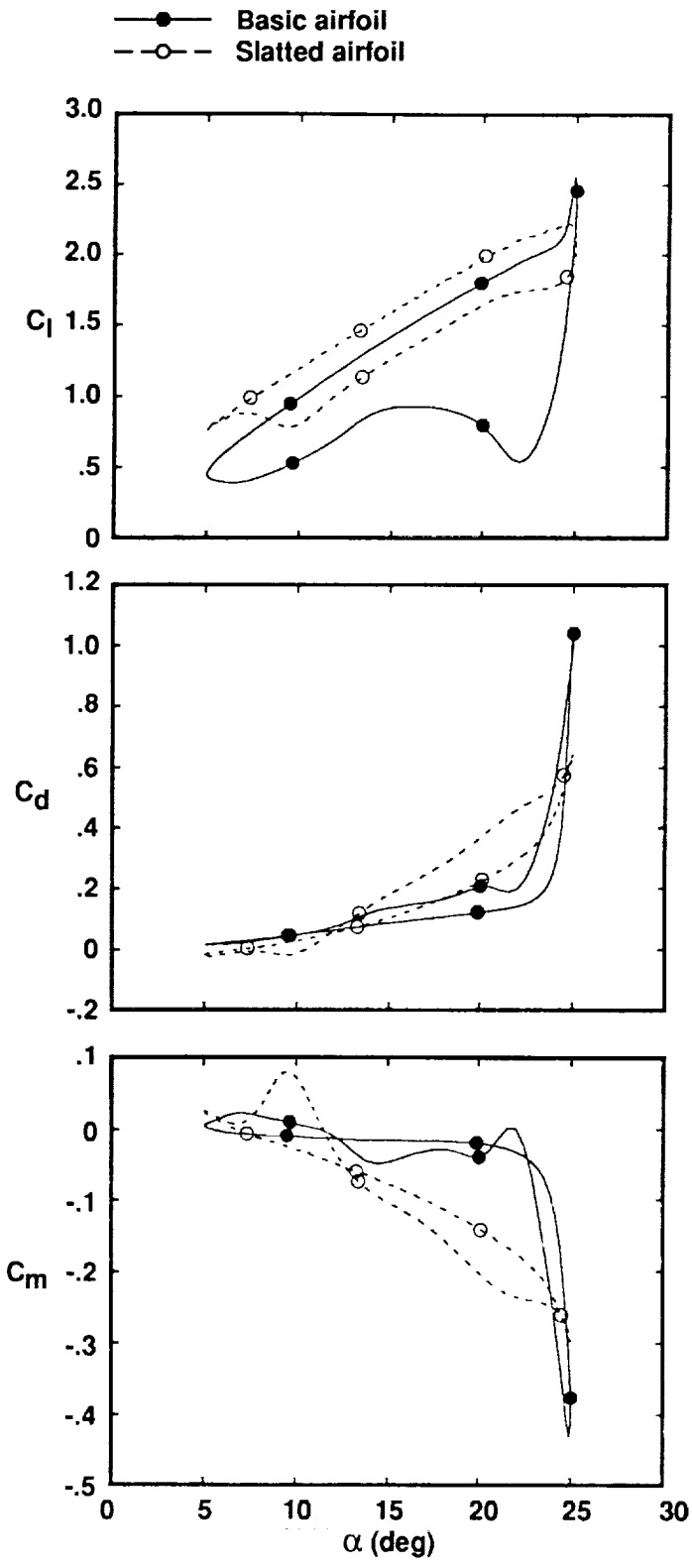

Figure 16. Comparison of the calculated loads for the basic and extended-slat airfoils with $\alpha = 15° + 10° \sin(\omega t)$ and $k = 0.1$.

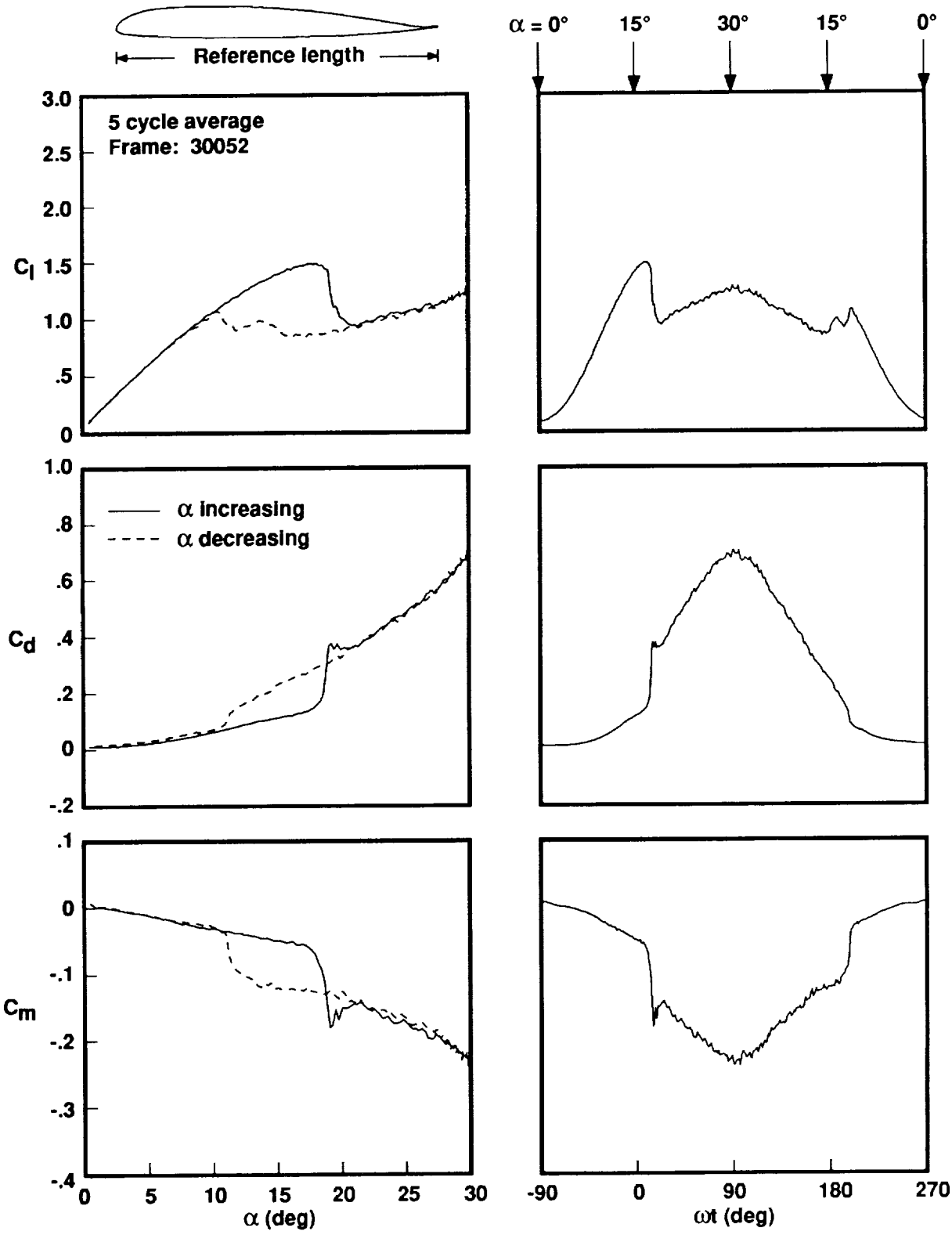

Figure 17. Measured loads for the basic airfoil with $\alpha = 15° + 15° \sin(\omega t)$ and $k = 0.003$.

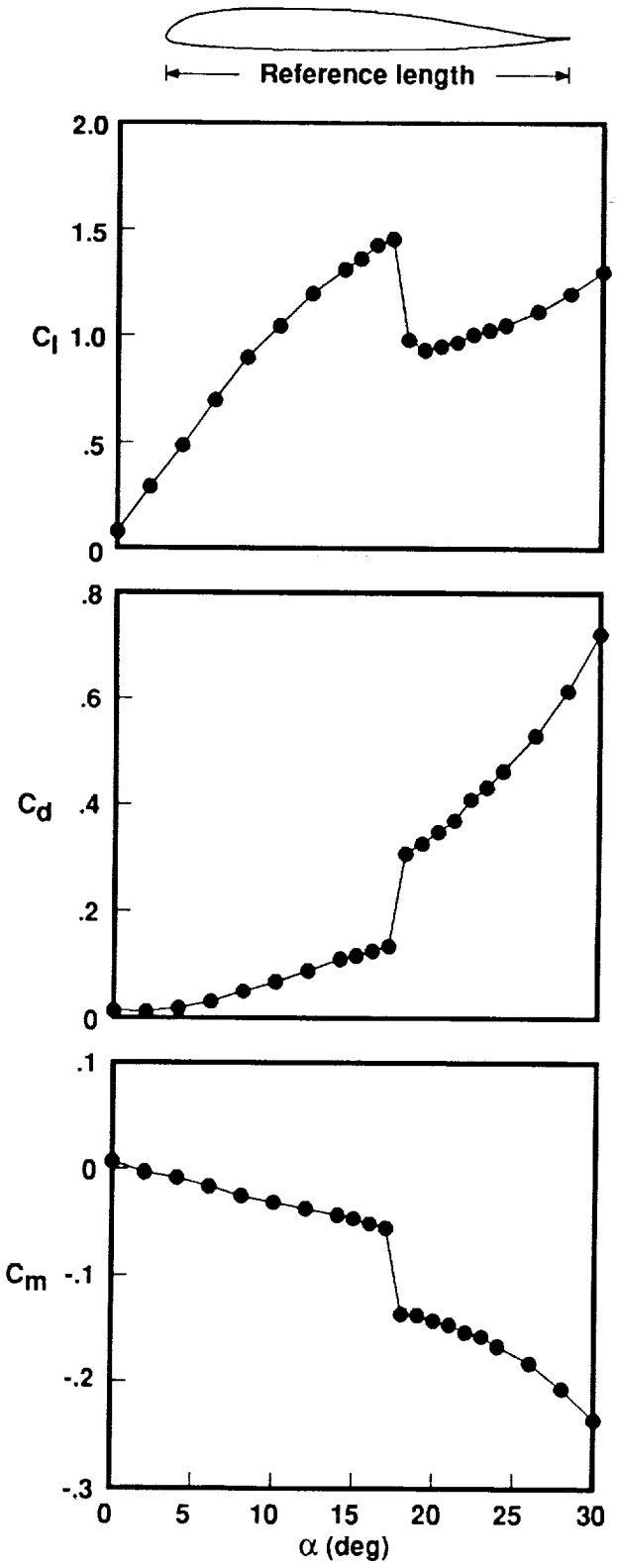

Figure 18. Measured loads for the basic airfoil at fixed angles of attack.

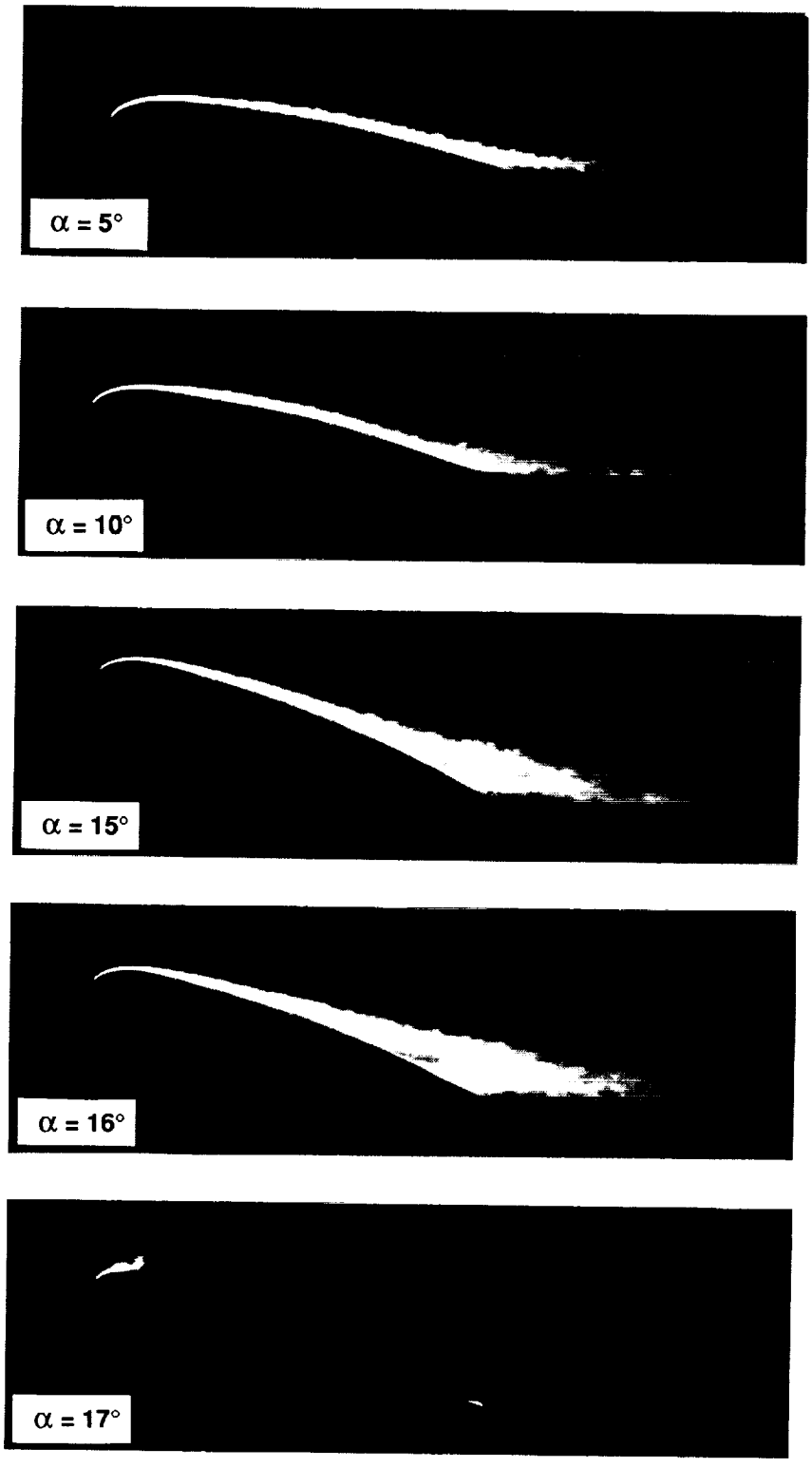

Figure 19. Boundary-layer and wake visualizations for the basic VR-12 airfoil at fixed angles of attack.

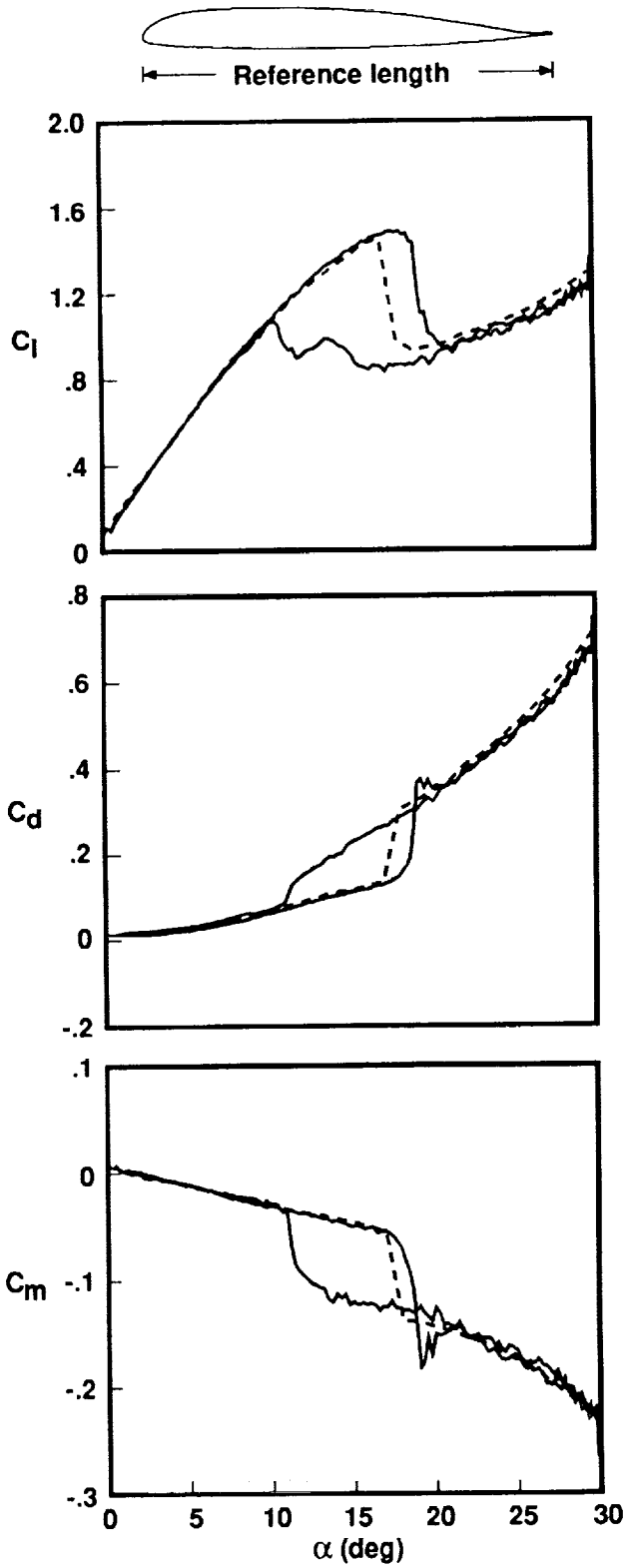

Figure 20. Comparison between steady and quasi-steady measured loads for the basic VR-12 airfoil. Quasi-steady data taken for $\alpha = 15° + 15° \sin(\omega t)$ and $k = 0.003$.

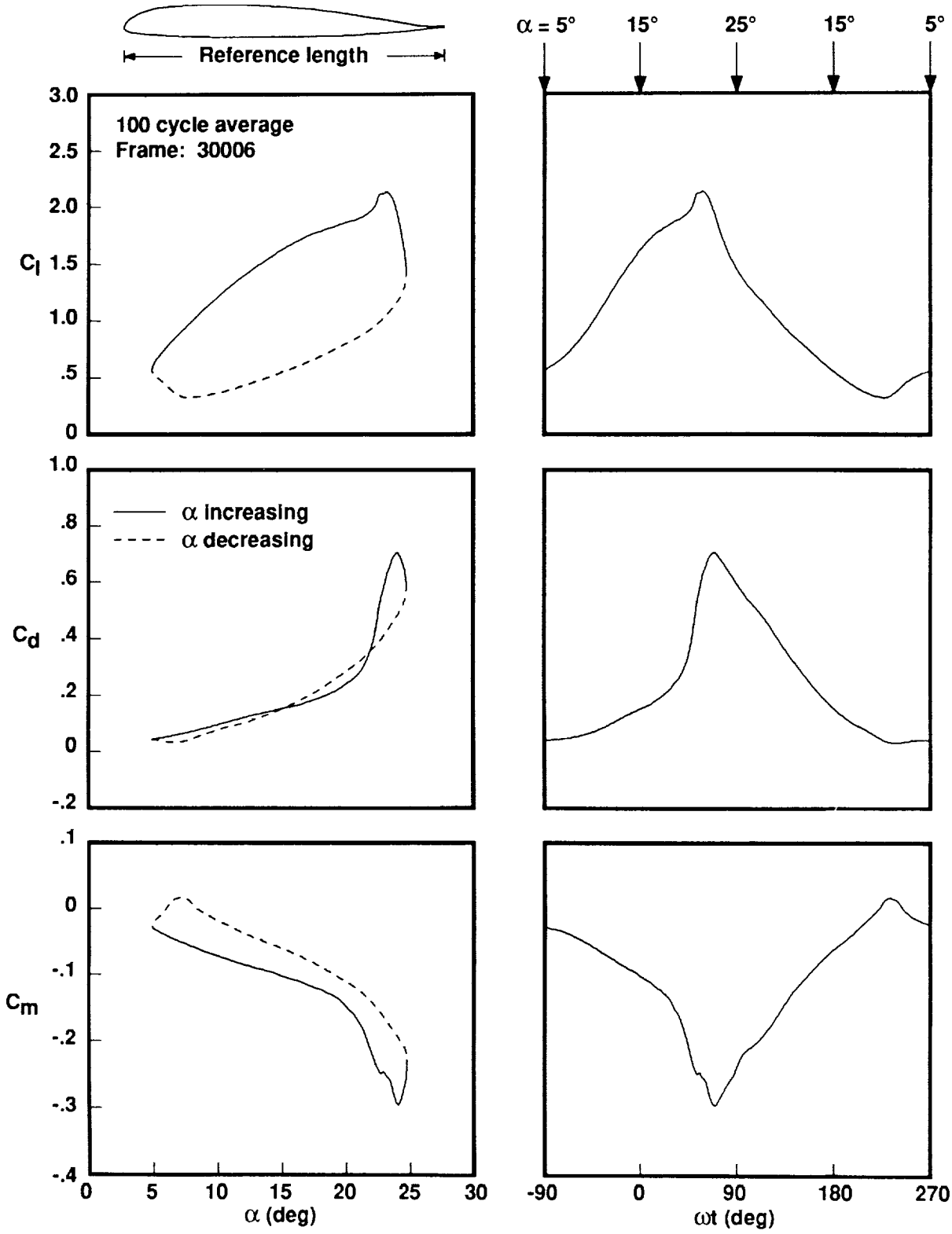

Figure 21. Measured loads for the basic VR-12 airfoil for $\alpha = 15° + 10° \sin(\omega t)$ and $k = 0.10$.

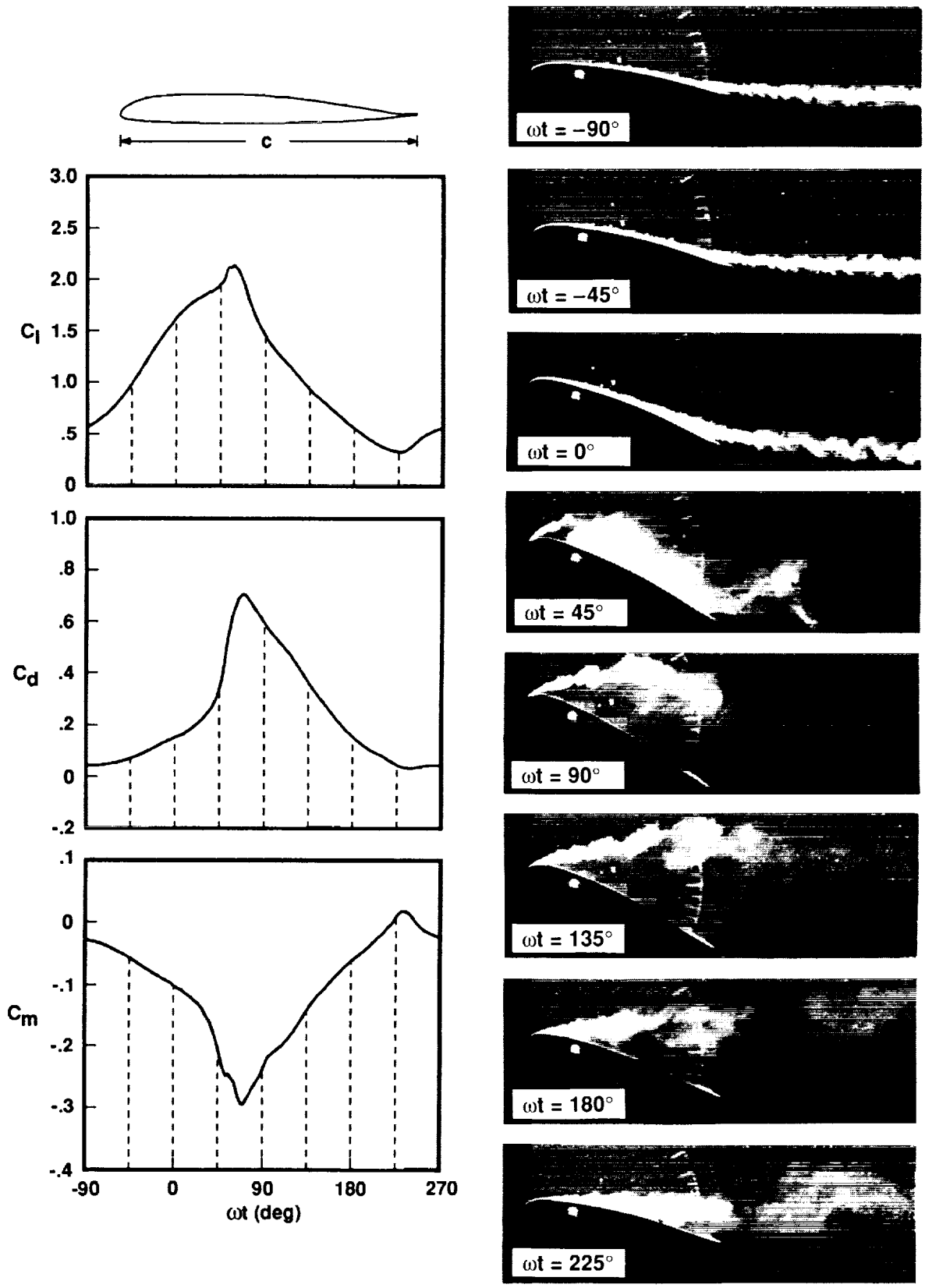

Figure 22. Visualization of flow over cycle of oscillation for the basic VR-12 airfoil at $\alpha = 15° + 10° \sin(\omega t)$ and $k = 0.10$.

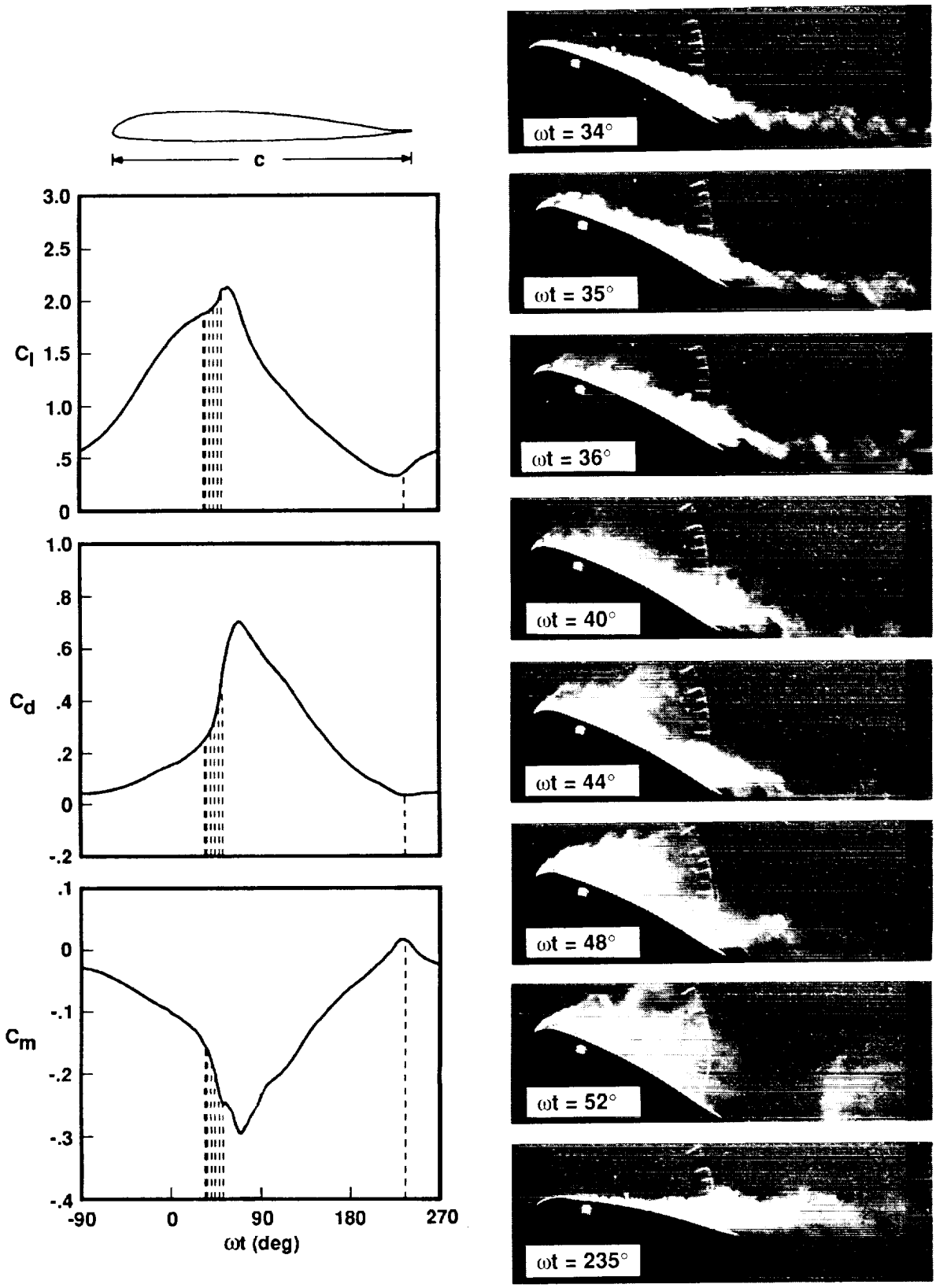

Figure 23. Visualization of flow with emphasis on the initial stages of stall for the basic VR-12 airfoil at $\alpha = 15° + 10° \sin(\omega t)$ and $k = 0.10$.

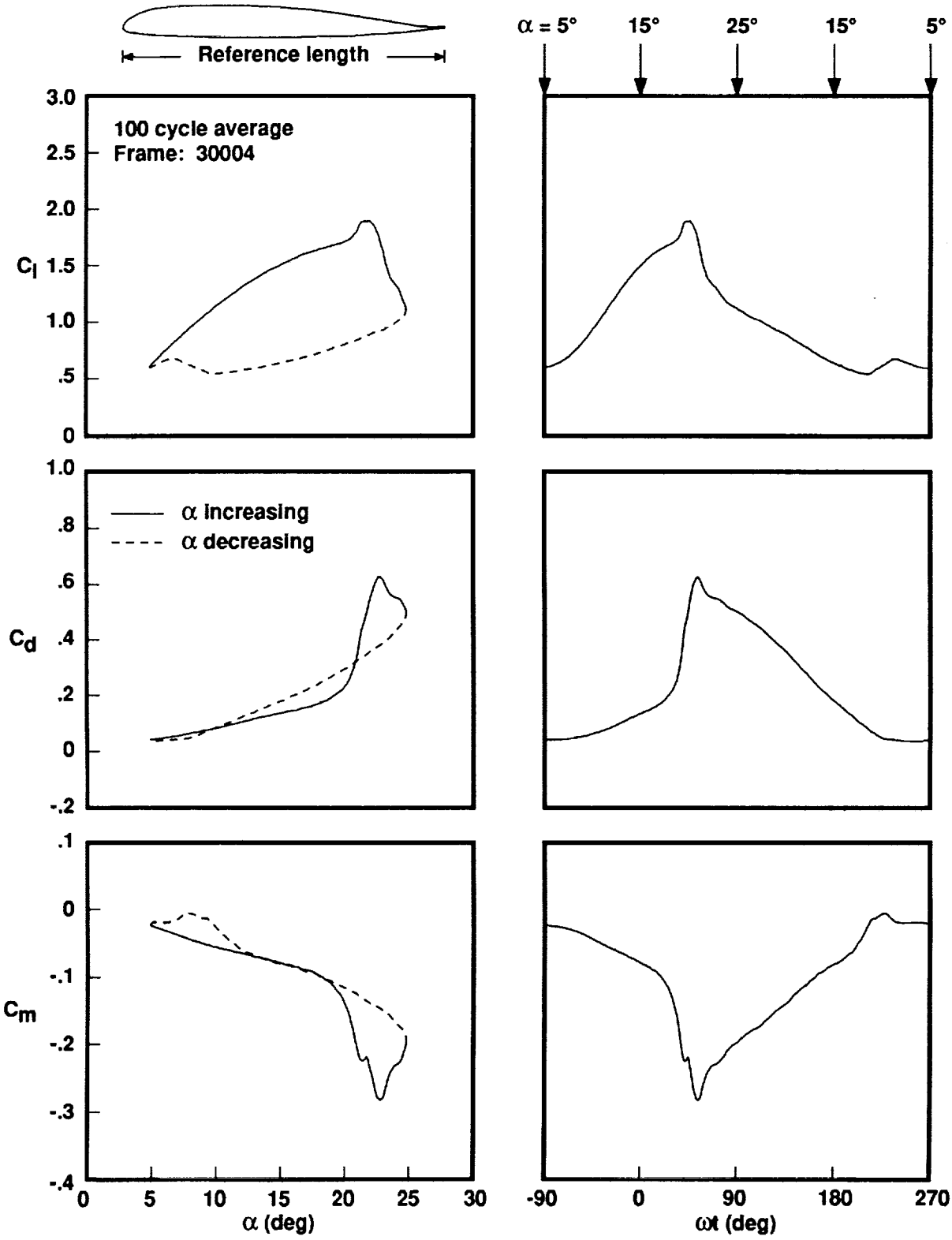

Figure 24. Reduced frequency effects on the basic VR-12 airfoil at $\alpha = 15° + 10° \sin(\omega t)$. (a) $k = 0.05$.

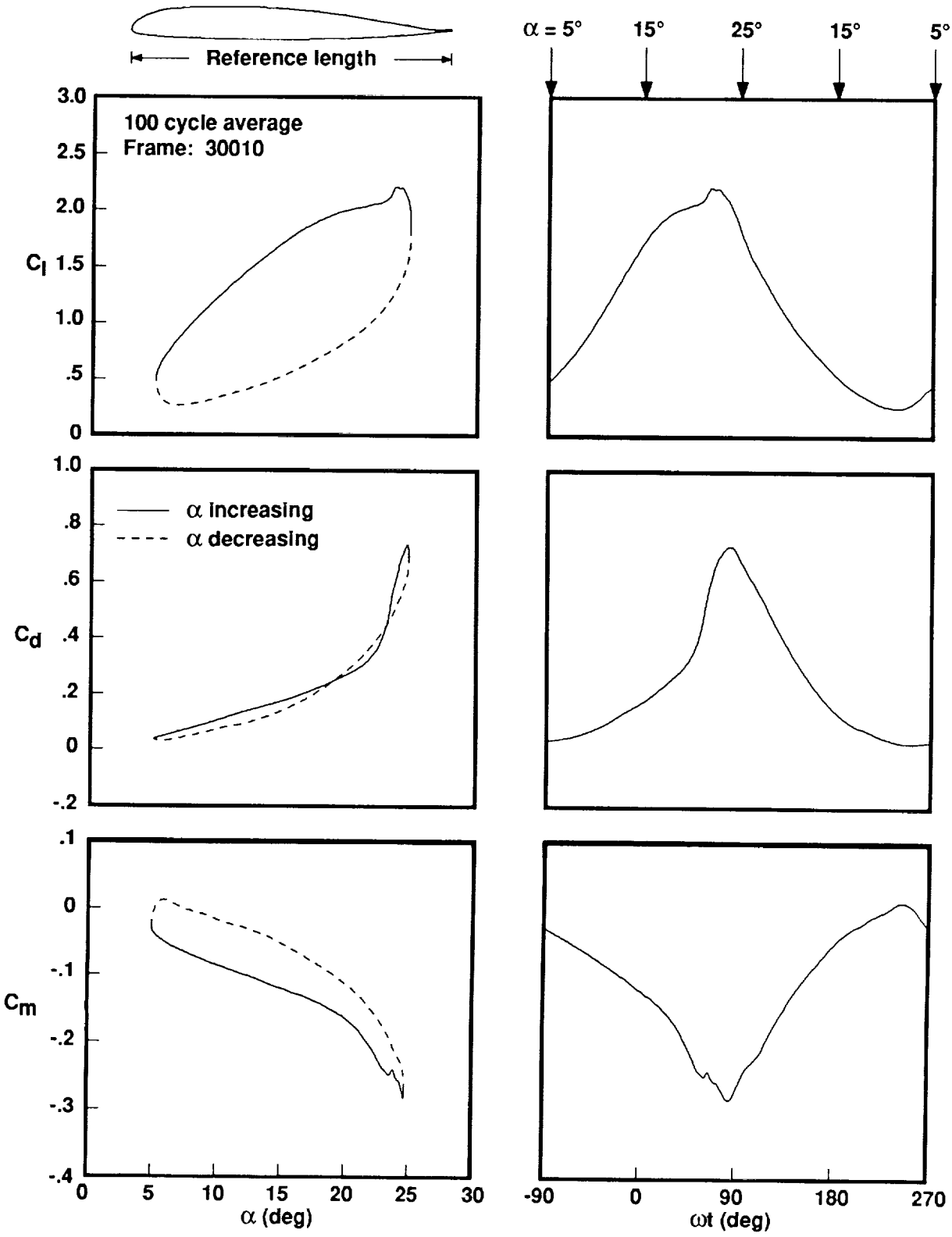

Figure 24. Continued. (b) $k = 0.15$.

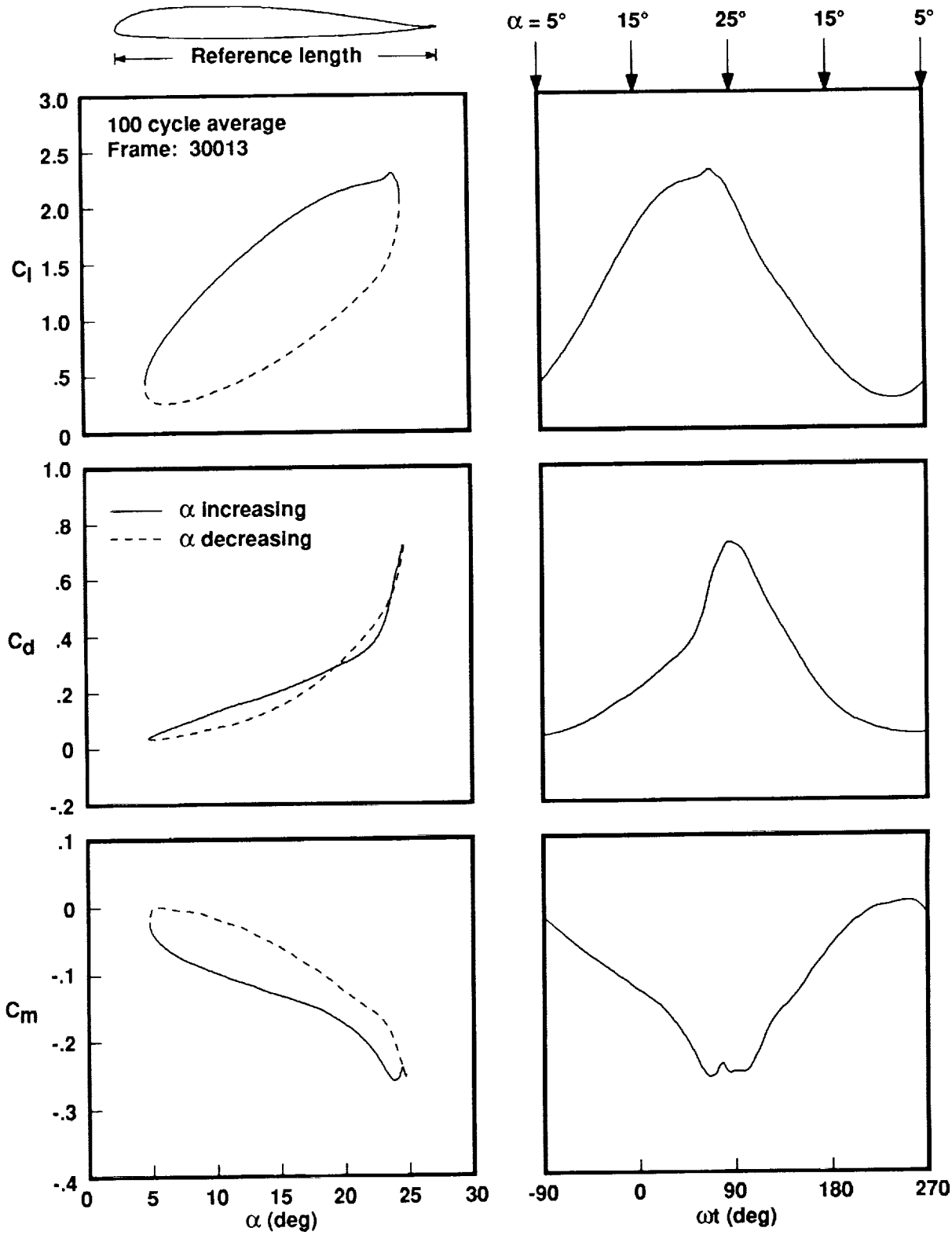

Figure 24. Concluded. (c) $k = 0.20$.

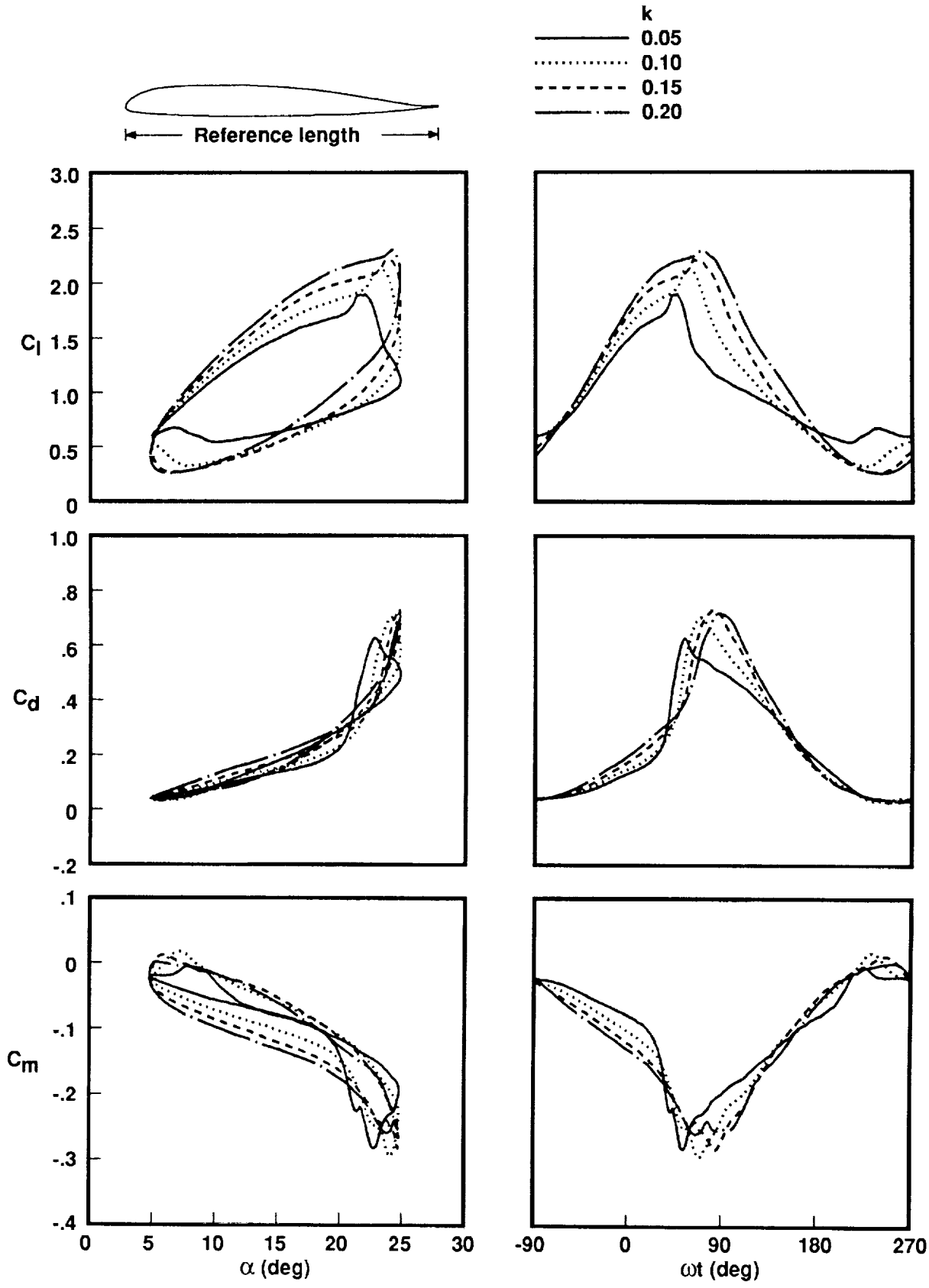

Figure 25. Superposition of results for $k = 0.05 \rightarrow 0.20$ for the basic VR-12 airfoil at $\alpha = 15^\circ + 10^\circ \sin(\omega t)$.

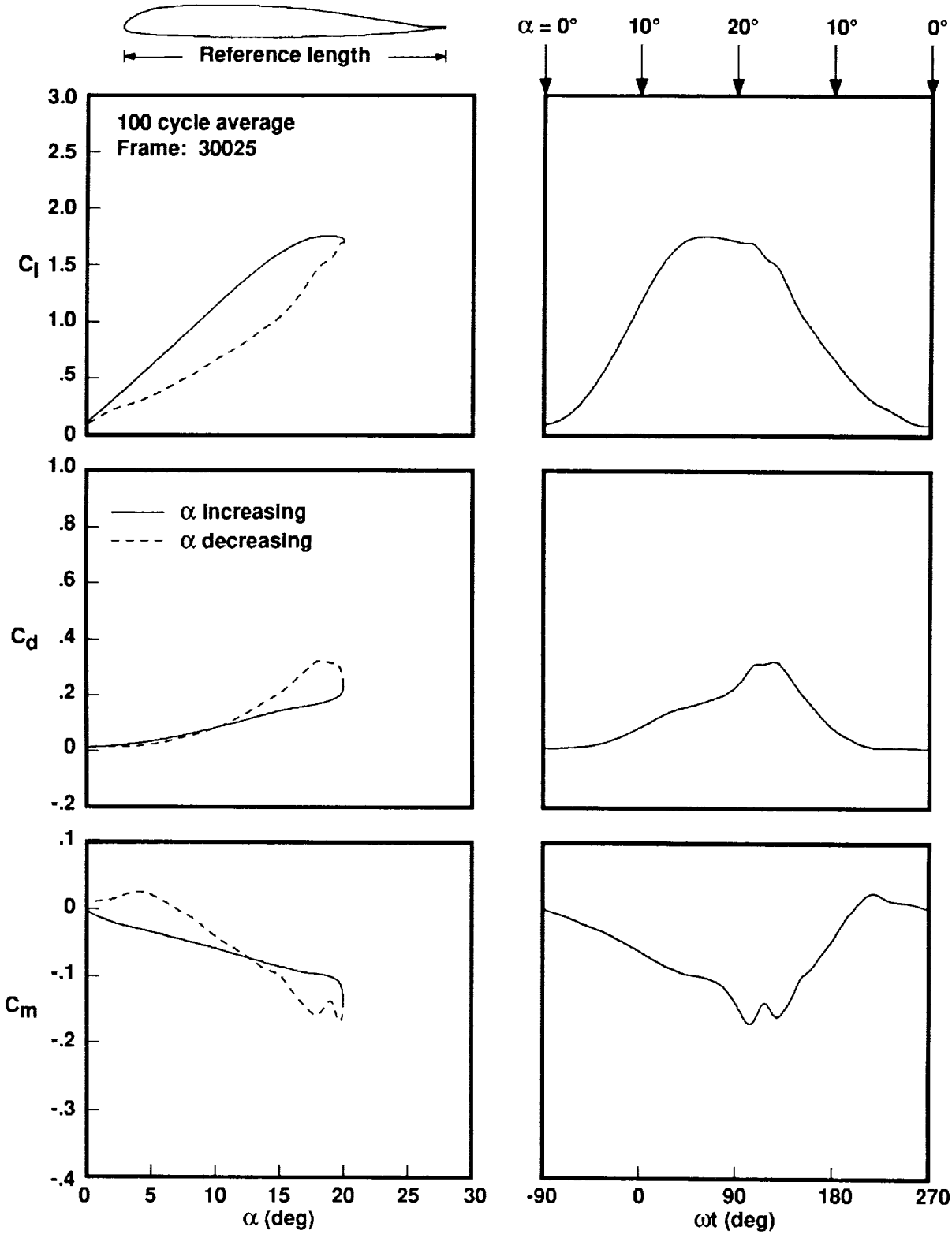

Figure 26. Effects of mean angle of oscillation on the basic VR-12 airfoil at $k = 0.10$. (a) $\alpha = 10° + 10° \sin(\omega t)$.

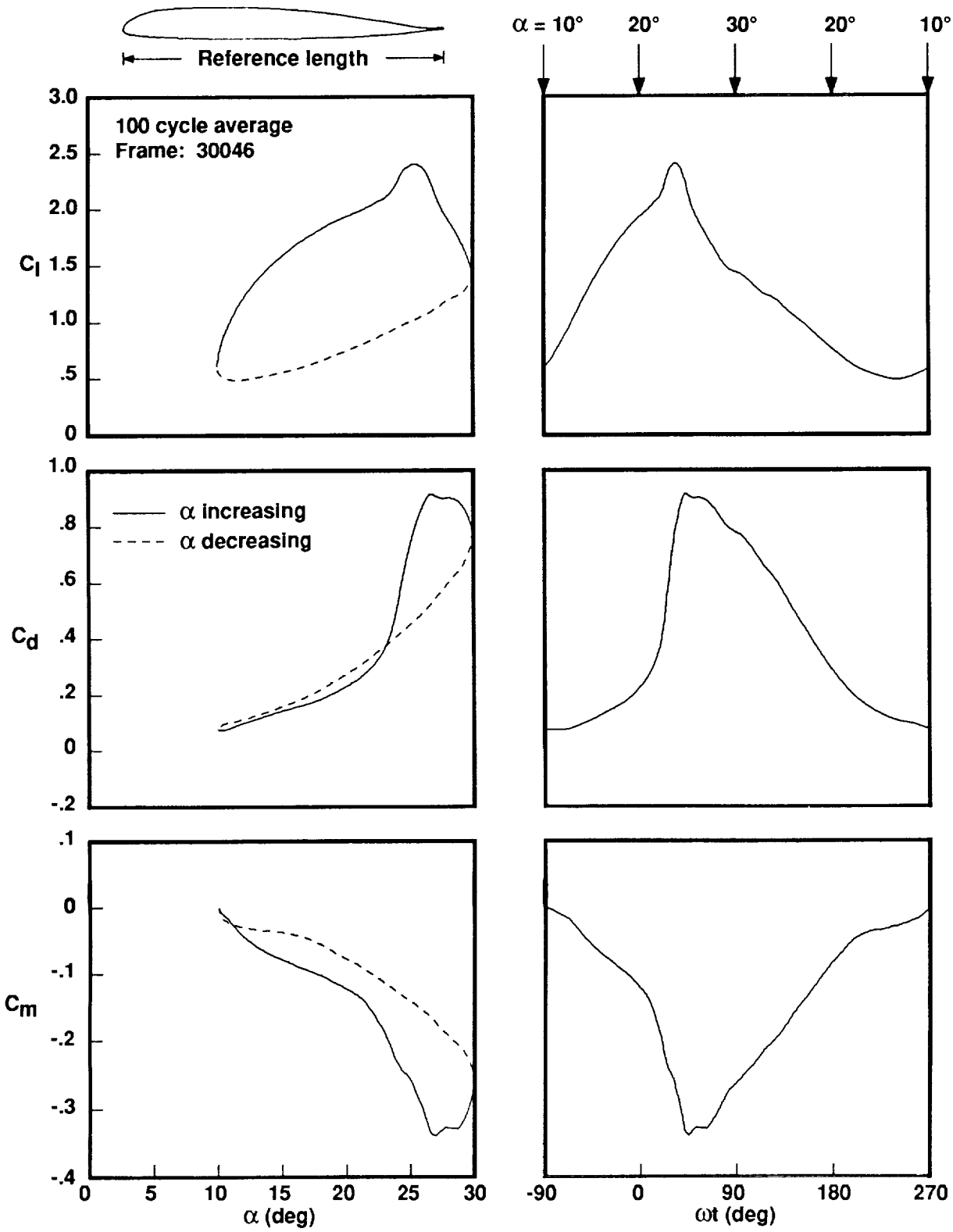

Figure 26. Concluded. (b) $\alpha = 20° + 10° \sin(\omega t)$.

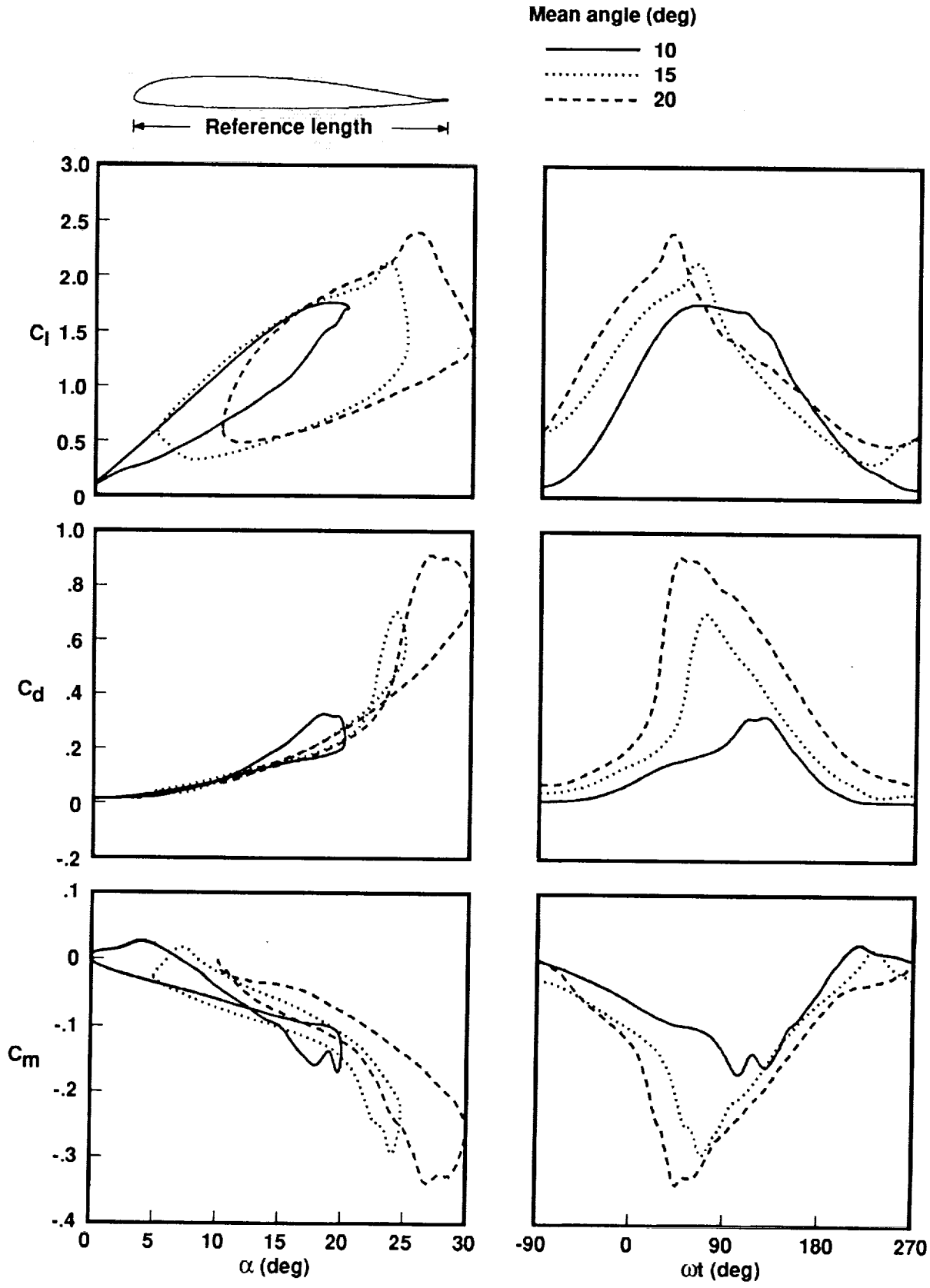

Figure 27. Superposition of results for mean angles of oscillation from 10° → 20° for the basic VR-12 airfoil at $k = 0.10$.

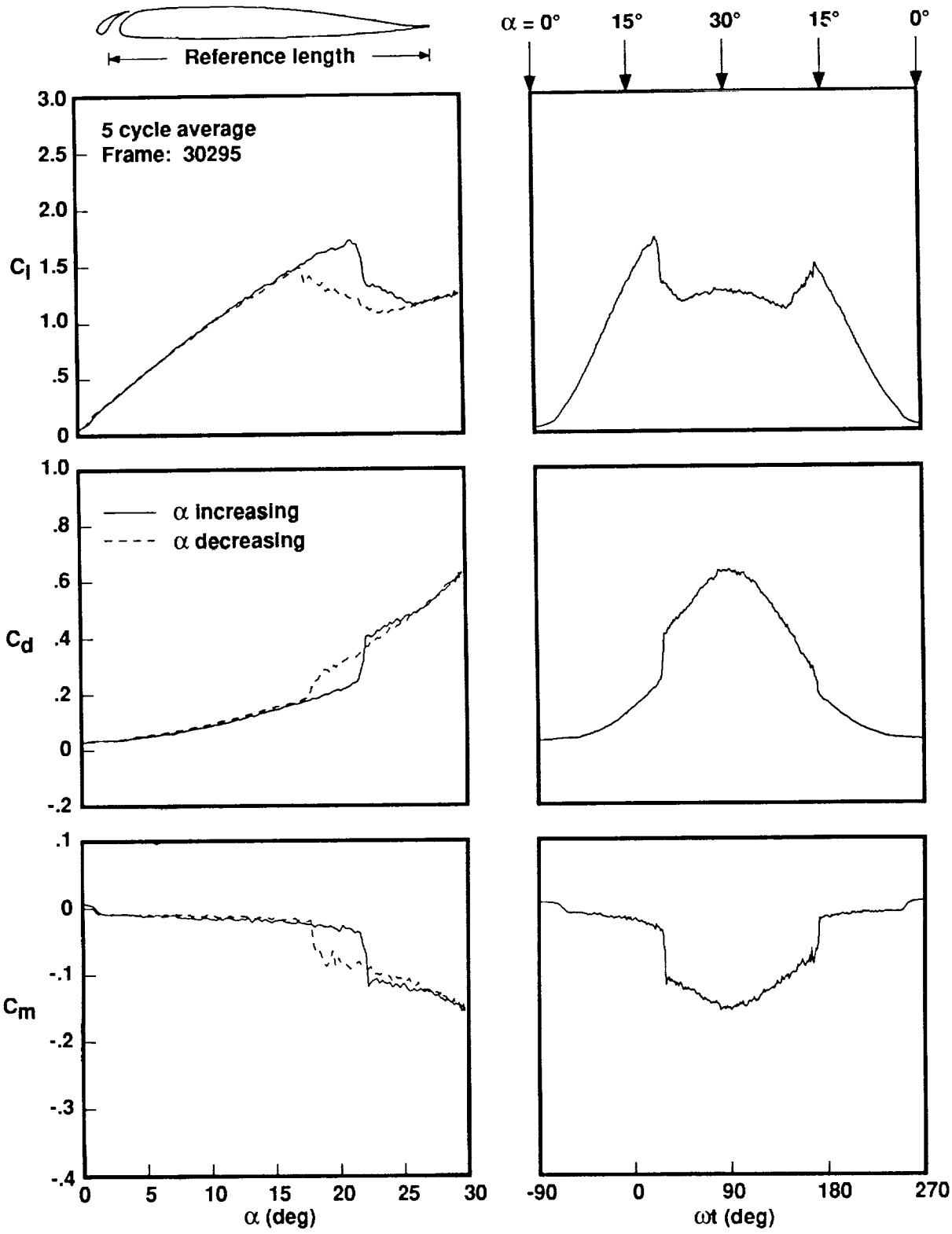

Figure 28. Measured loads for the extended-slat airfoil with $\alpha = 15° + 15° \sin(\omega t)$ and $k = 0.003$.

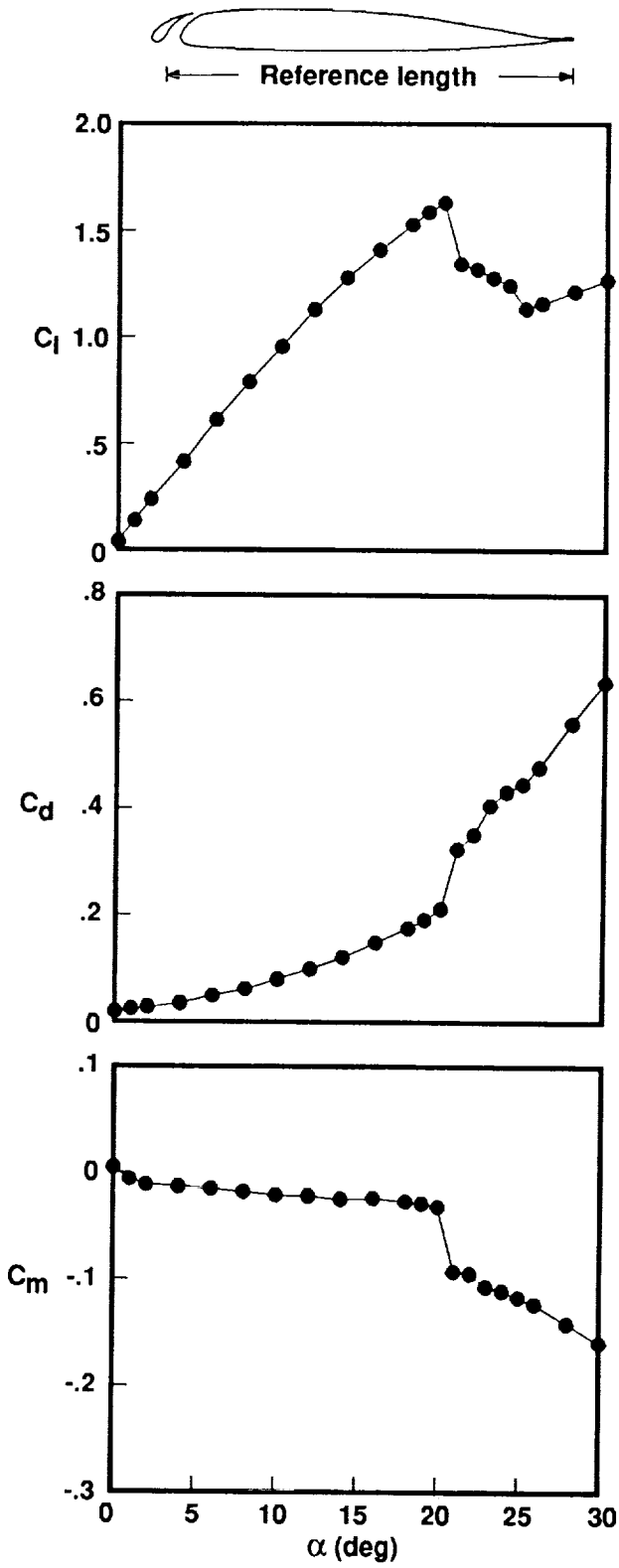

Figure 29. Measured loads for the extended-slat airfoil at fixed angles of attack.

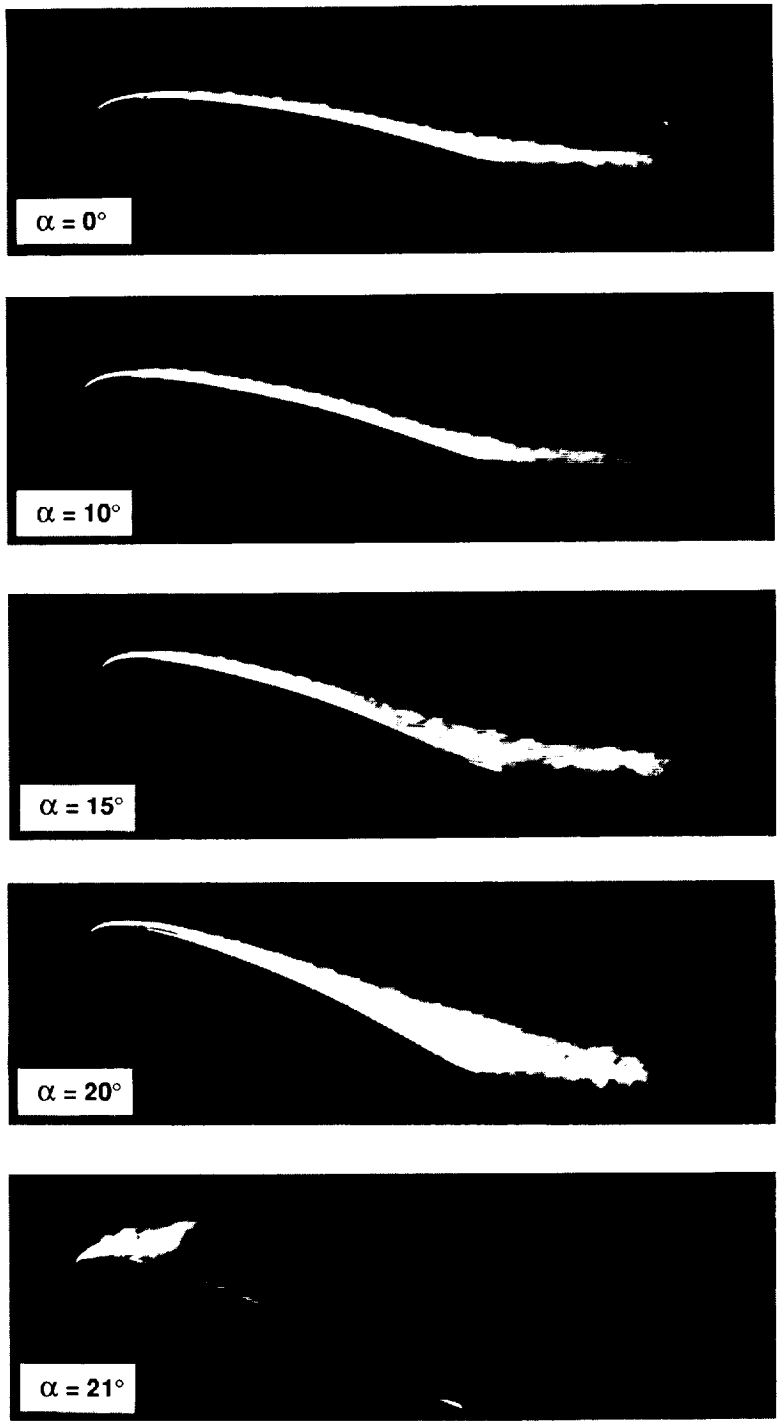

Figure 30. Boundary-layer and wake visualizations for the extended-slat VR-12 airfoil at fixed angles of attack.

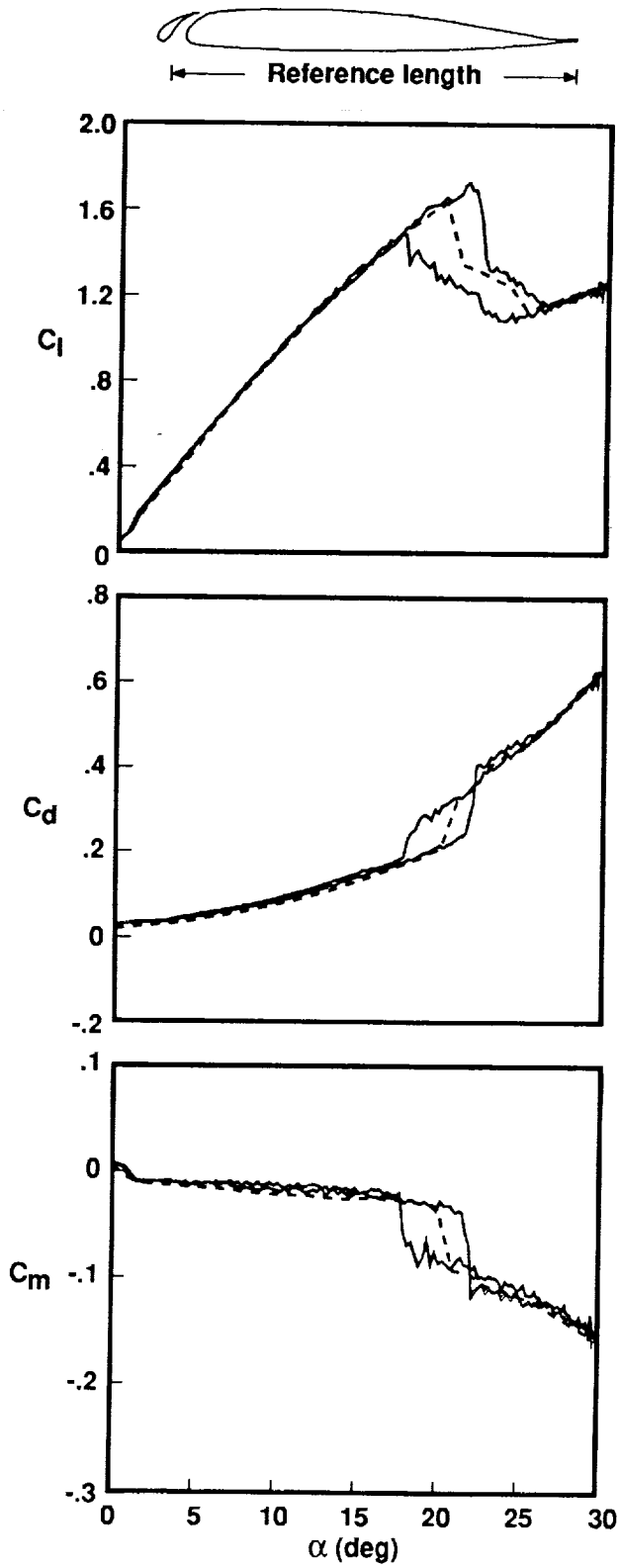

Figure 31. Comparison between steady and quasi-steady measured loads for the extended-slat VR-12 airfoil. Quasi-steady data taken for $\alpha = 15° + 15° \sin(\omega t)$ and $k = 0.003$.

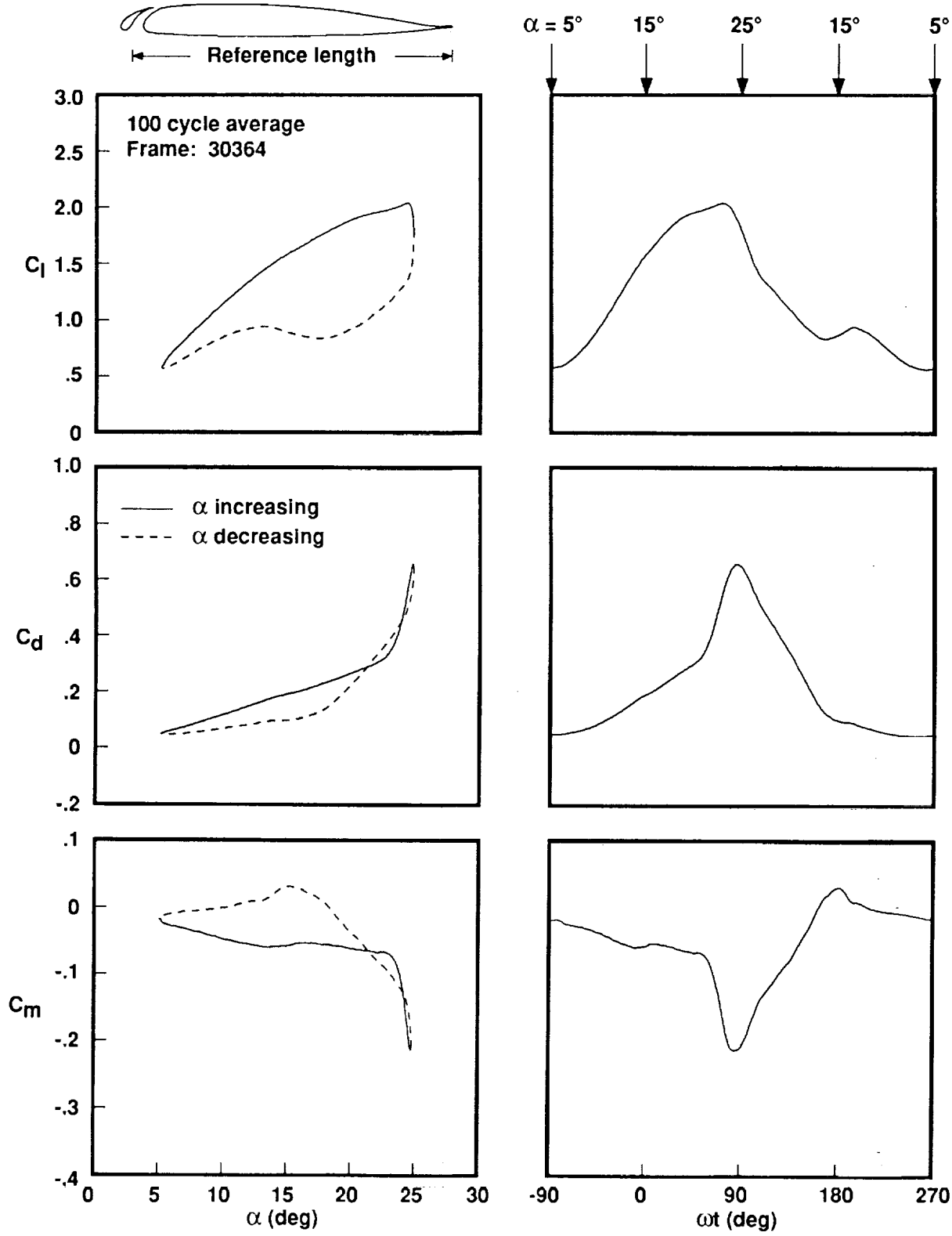

Figure 32. Measured loads for the extended-slat VR-12 airfoil for $\alpha = 15° + 10° \sin(\omega t)$ and $k = 0.10$.

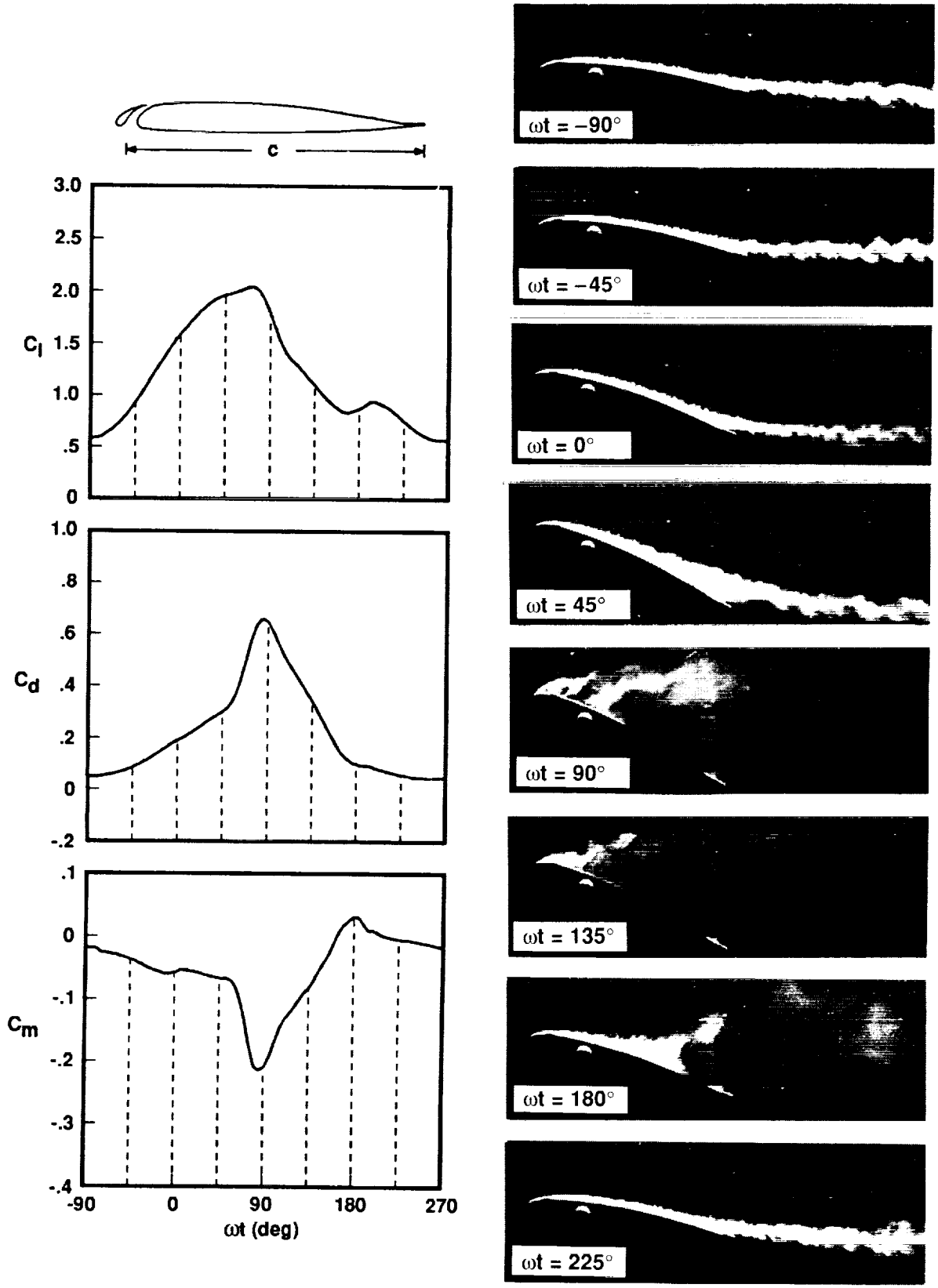

Figure 33. Visualization of flow over cycle of oscillation for the extended-slat VR-12 airfoil at $\alpha = 15° + 10° \sin(\omega t)$ and $k = 0.10$.

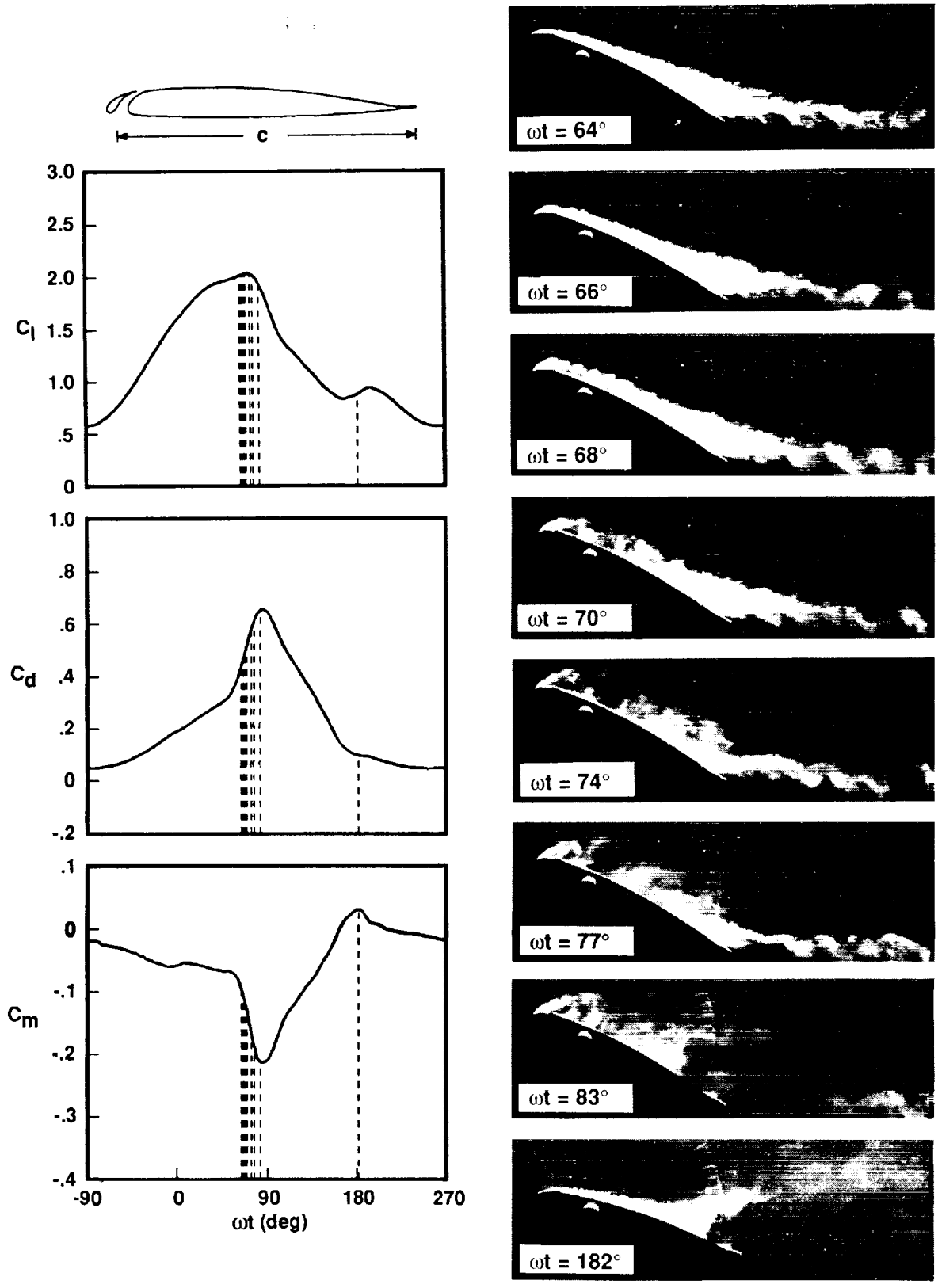

Figure 34. Visualization of flow with emphasis on the initial stages of stall for the extended-slat VR-12 airfoil at $\alpha = 15° + 10° \sin(\omega t)$ and $k = 0.10$.

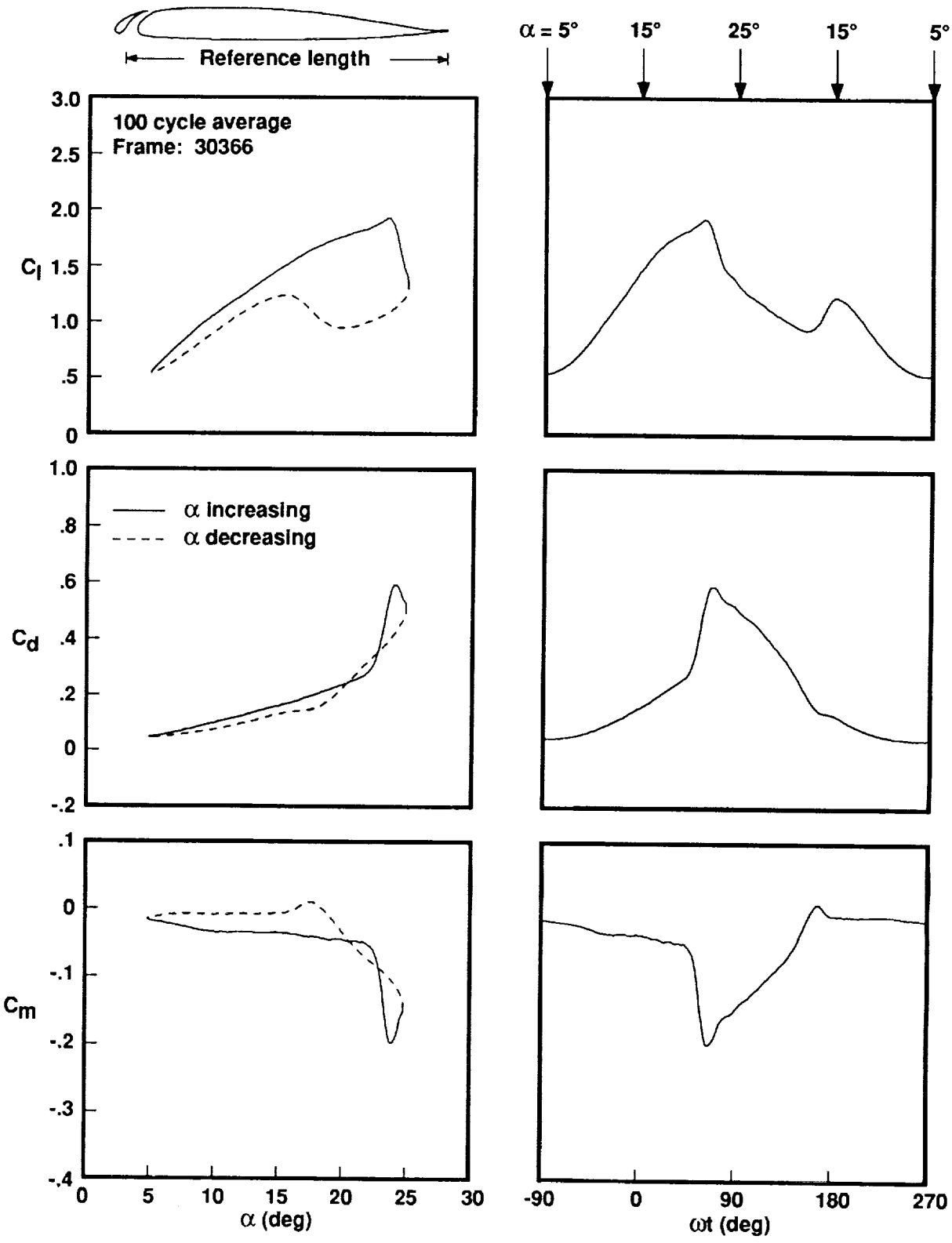

Figure 35. Reduced frequency effects on the extended-slat VR-12 airfoil at $\alpha = 15° + 10° \sin(\omega t)$. (a) $k = 0.05$.

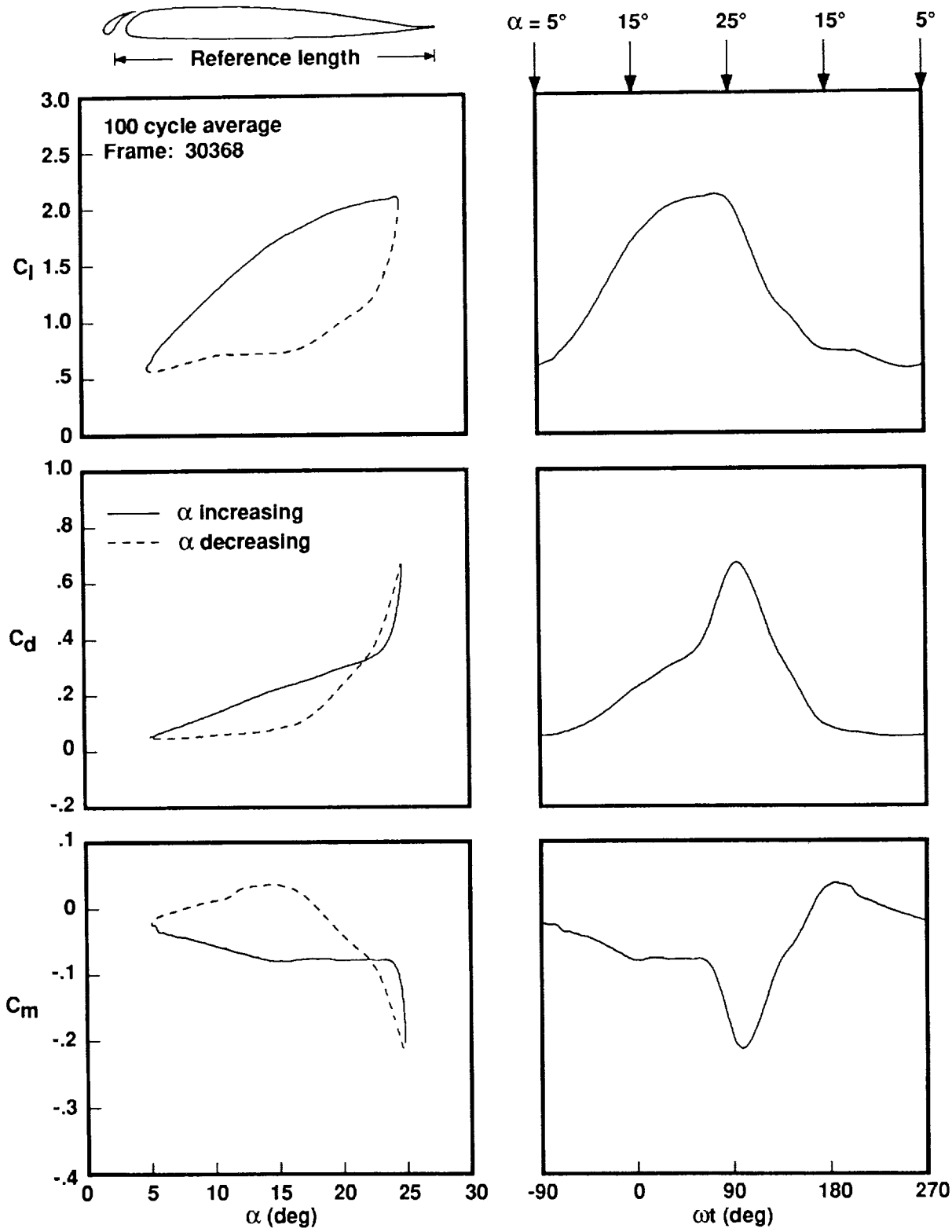

Figure 35. Continued. (b) $k = 0.15$.

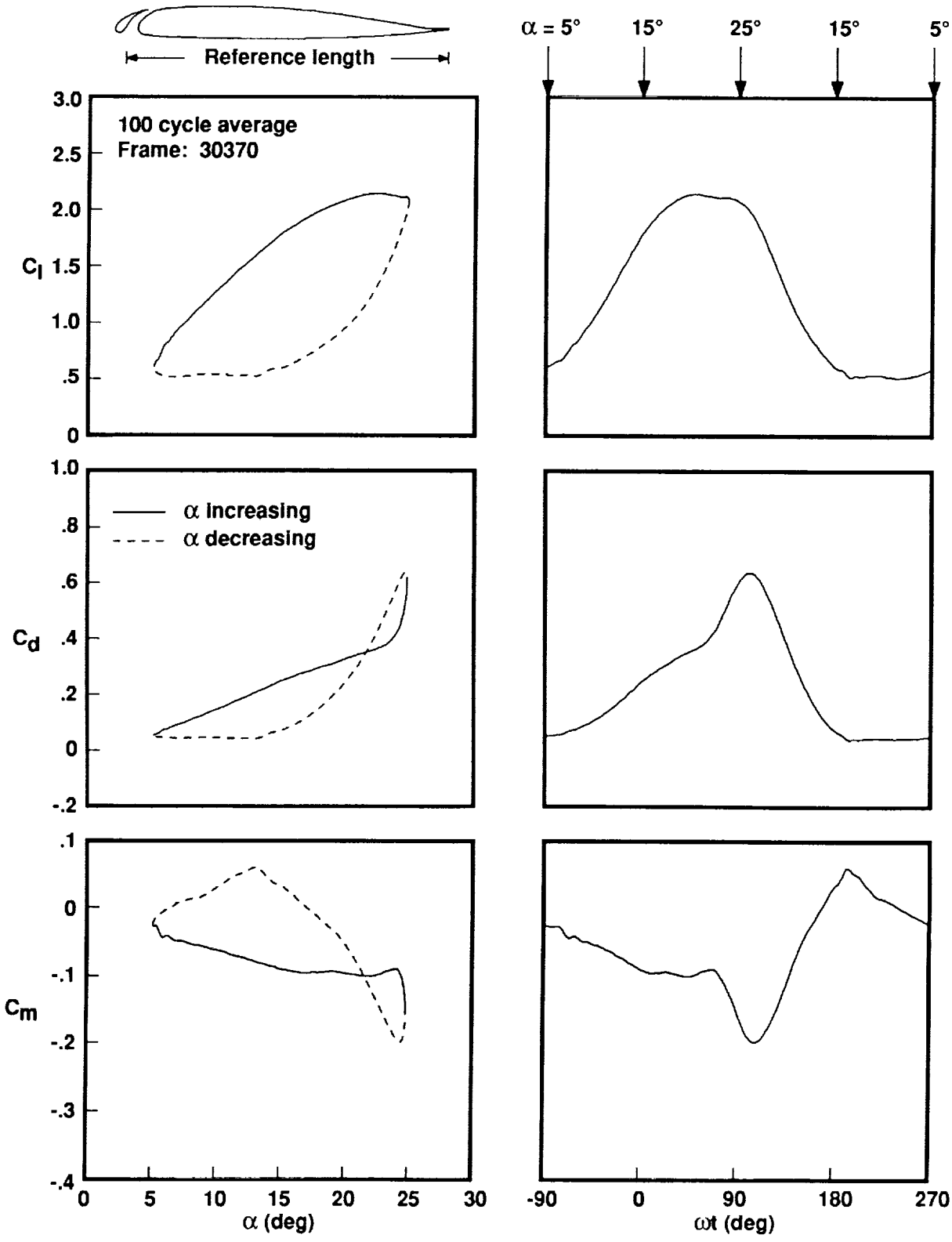

Figure 35. Concluded. (c) $k = 0.20$.

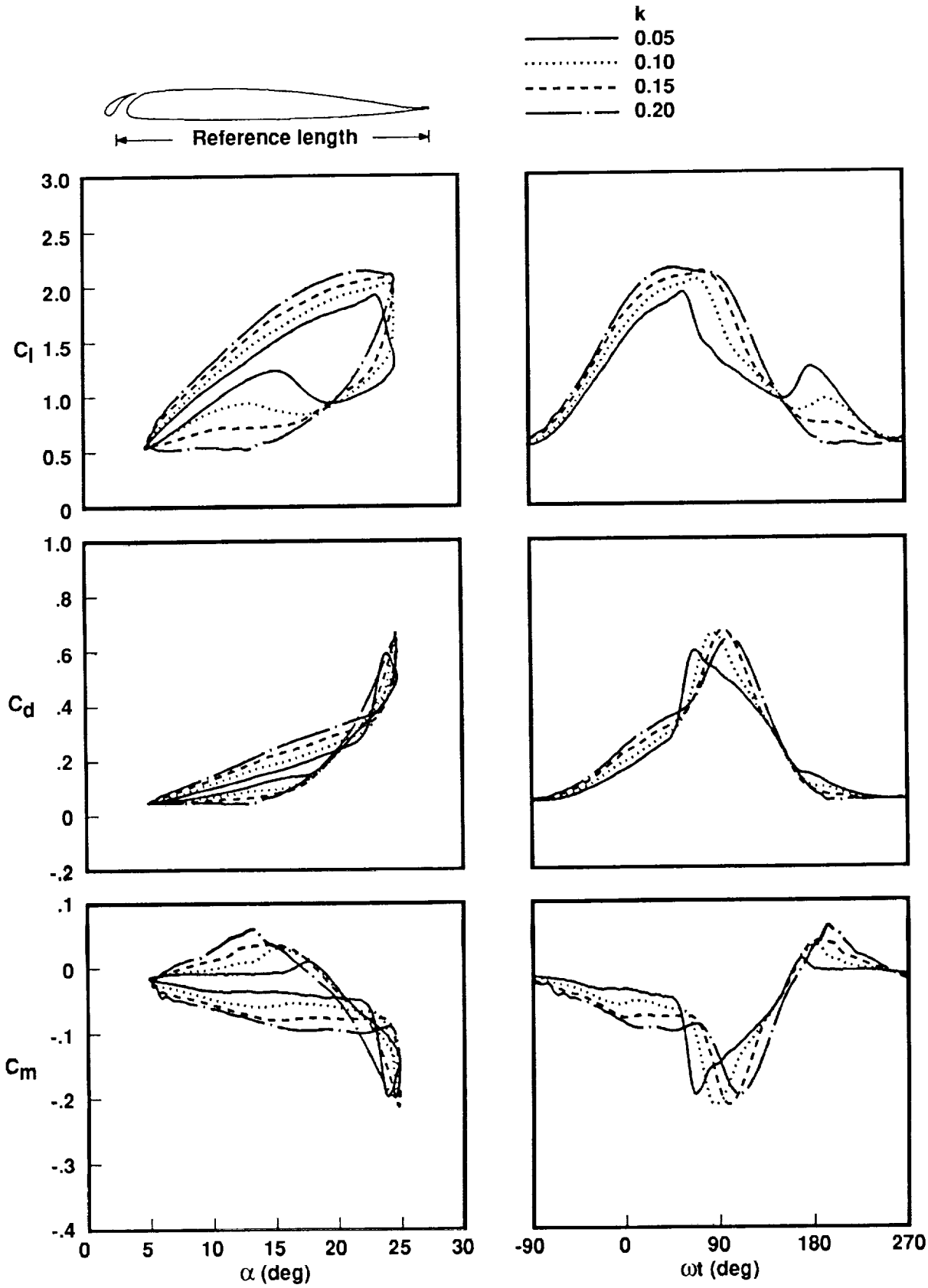

Figure 36. Superposition of results for $k = 0.05 \rightarrow 0.20$ for the extended-slat VR-12 airfoil at $\alpha = 15^\circ + 10^\circ \sin(\omega t)$.

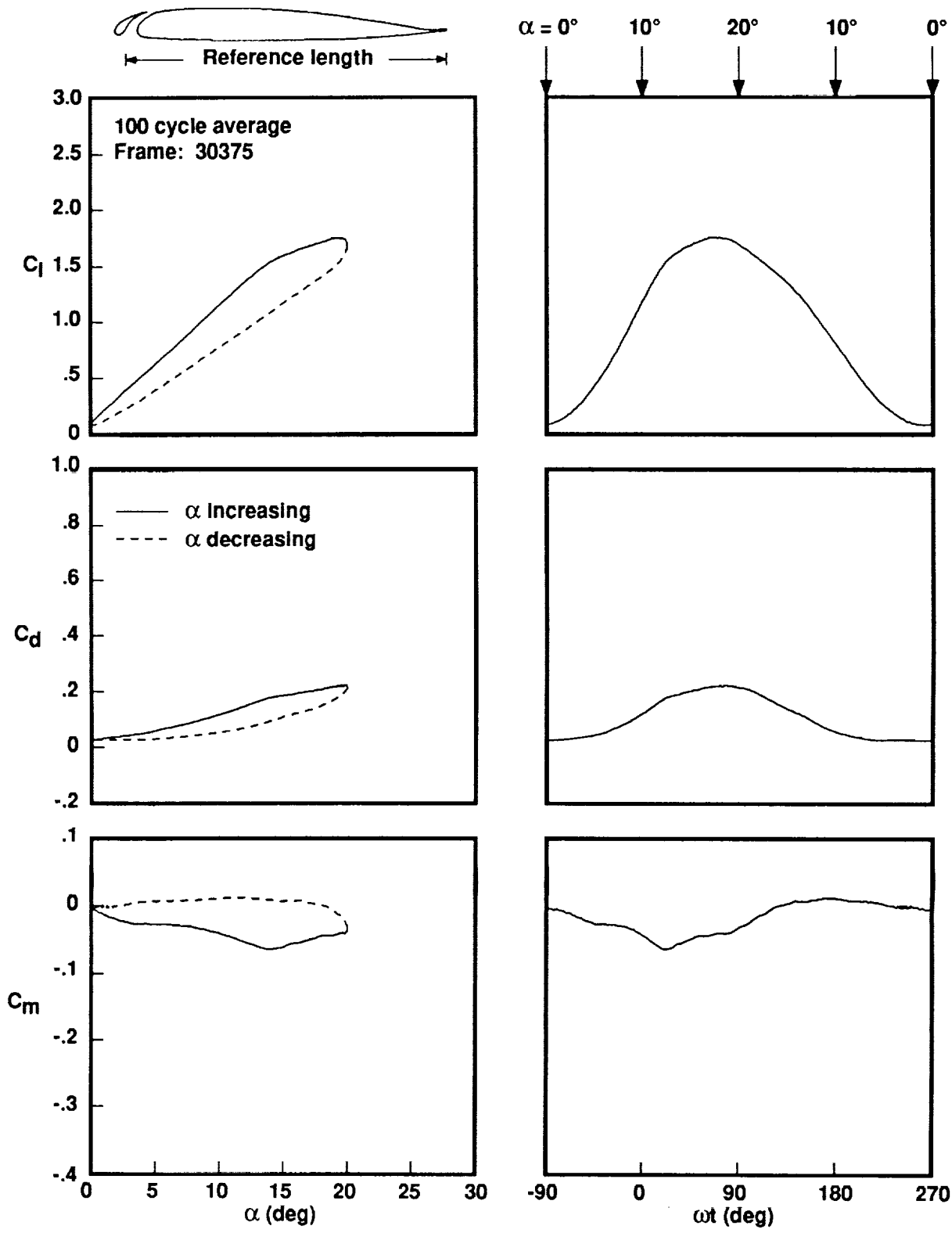

Figure 37. Effects of mean angle of oscillation on the extended-slat VR-12 airfoil at $k = 0.10$. (a) $\alpha = 10° + 10° \sin(\omega t)$.

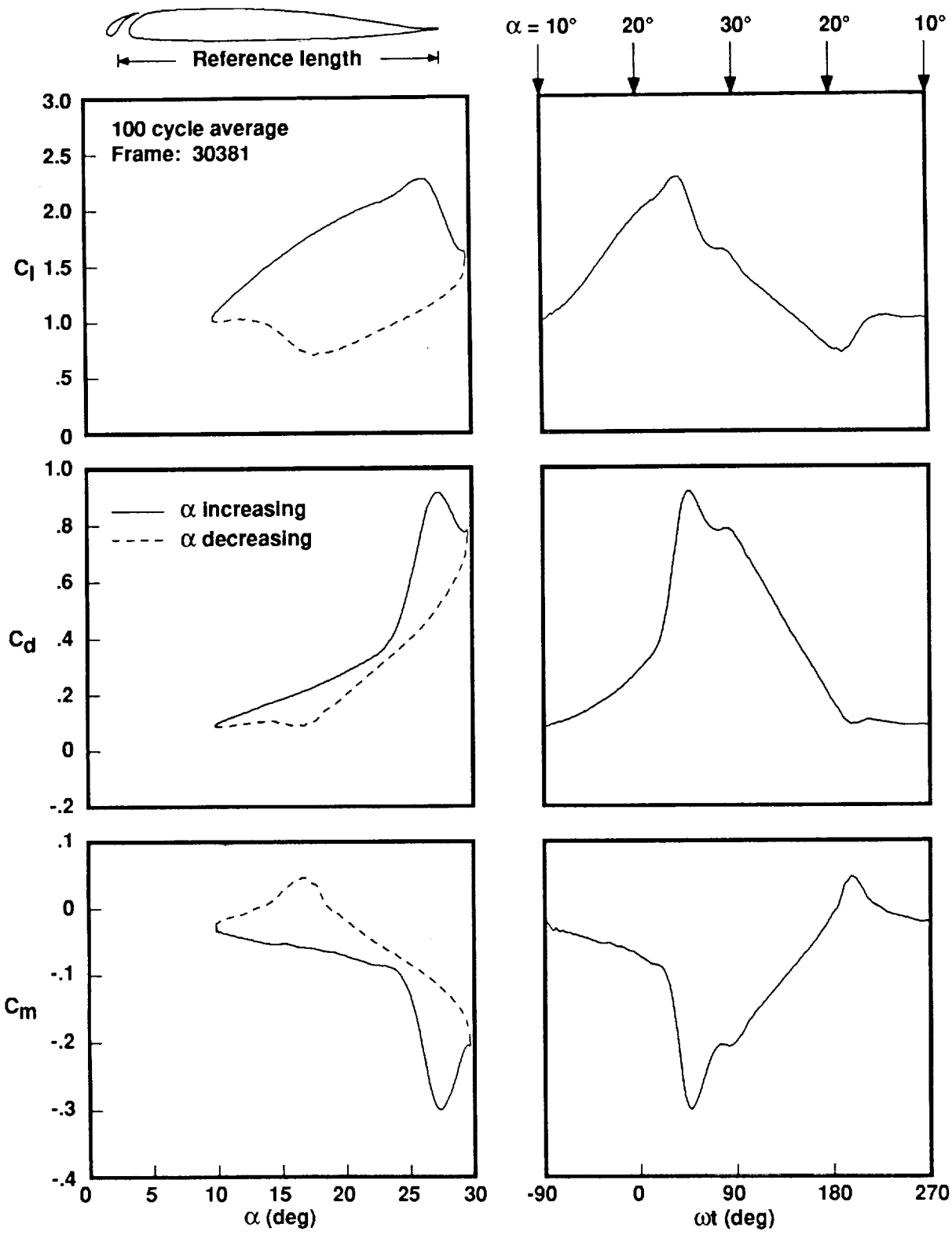

Figure 37. Concluded. (b) $\alpha = 20° + 10° \sin(\omega t)$.

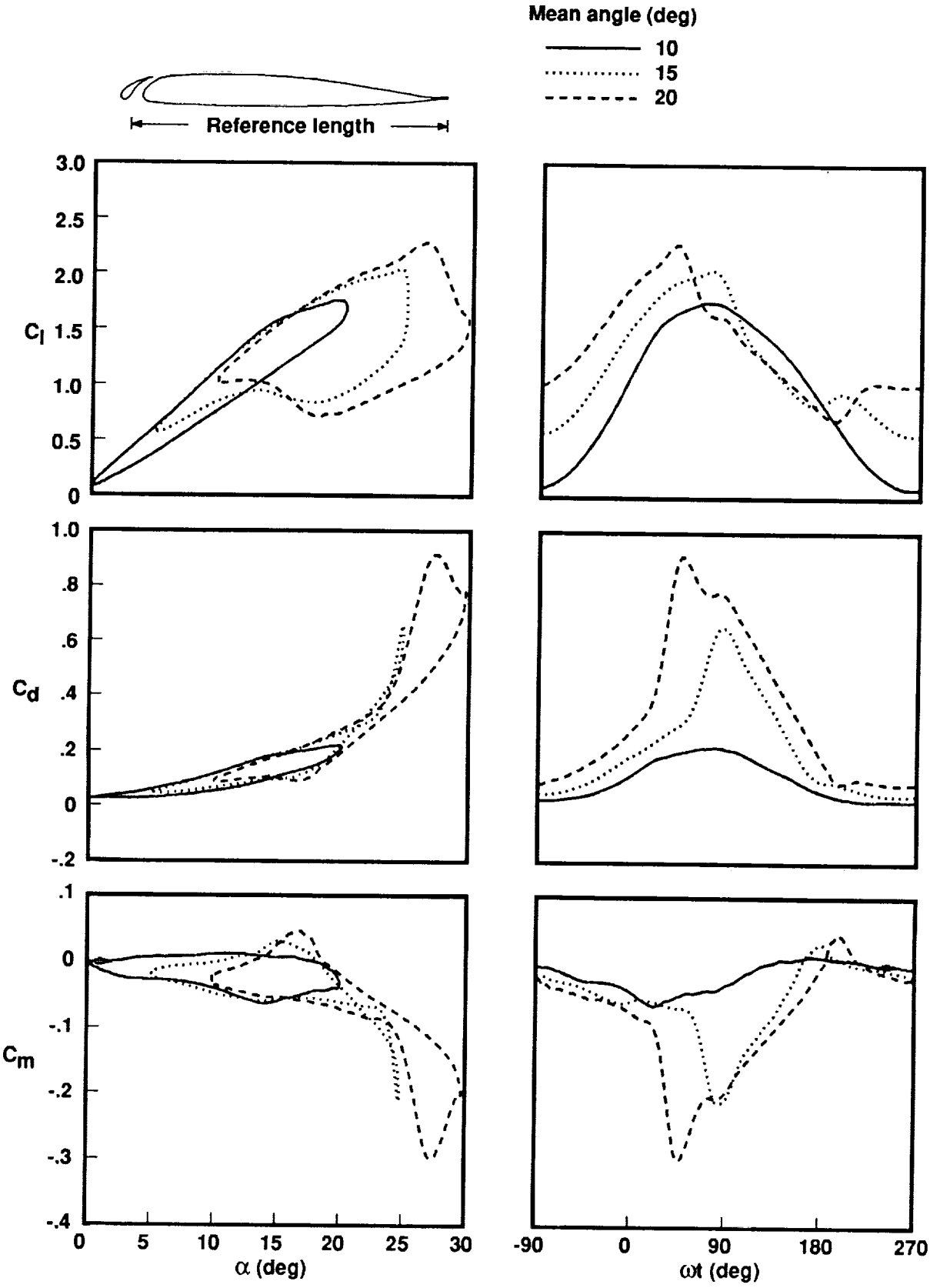

Figure 38. Superposition of results for mean angles of oscillation from 10° → 20° for the extended-slat VR-12 airfoil at $k = 0.10$.

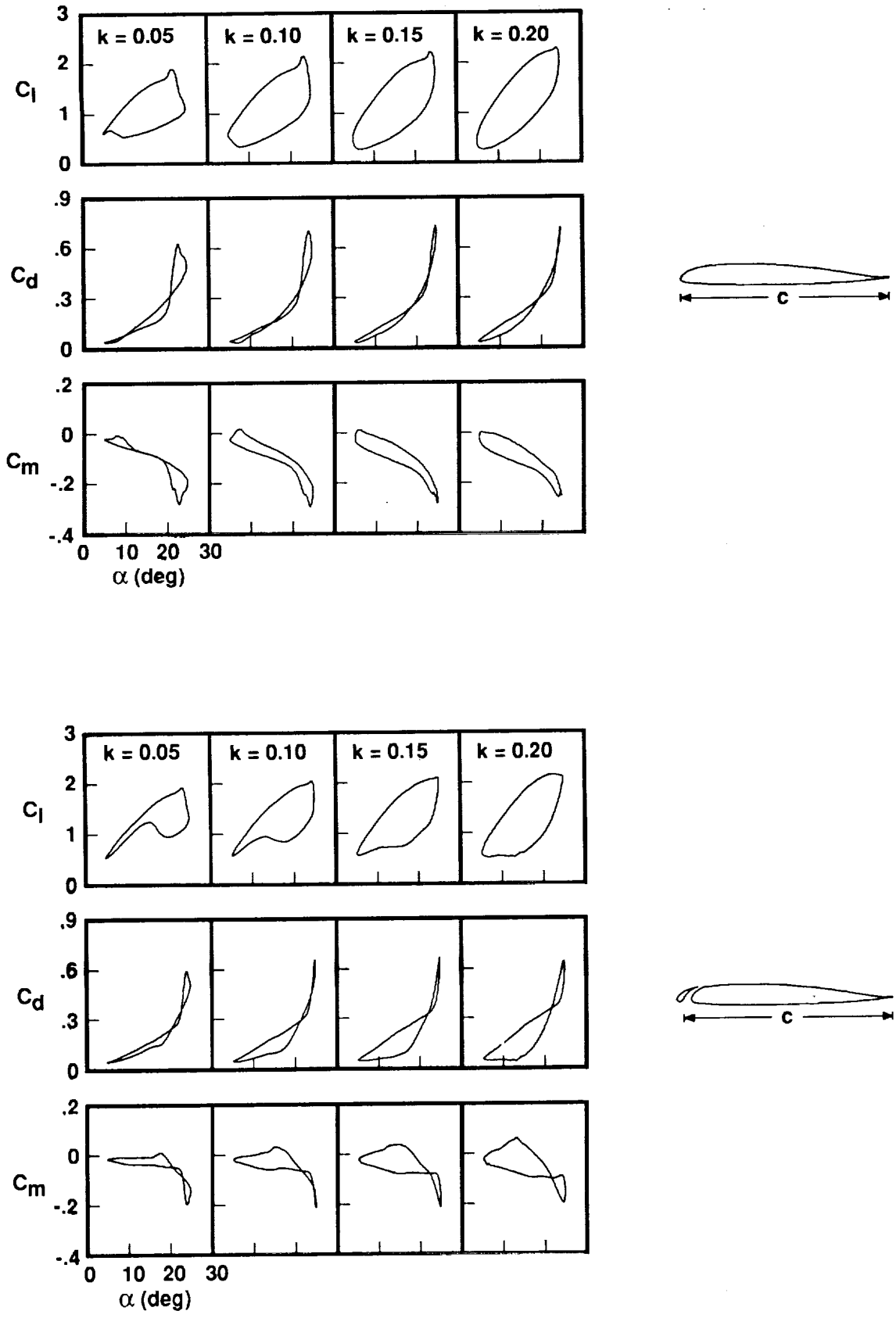

Figure 39. Summary of measured loads for the basic and extended-slat airfoils over a range of α_m and k. (a) $k = 0.05 \rightarrow 0.20$.

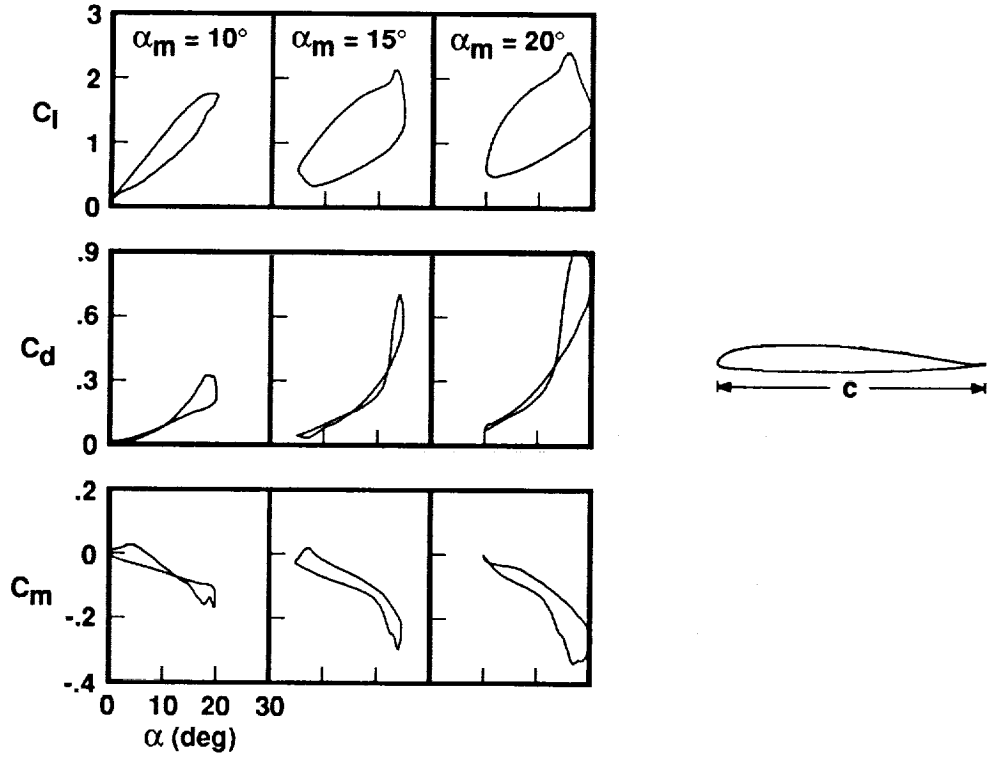

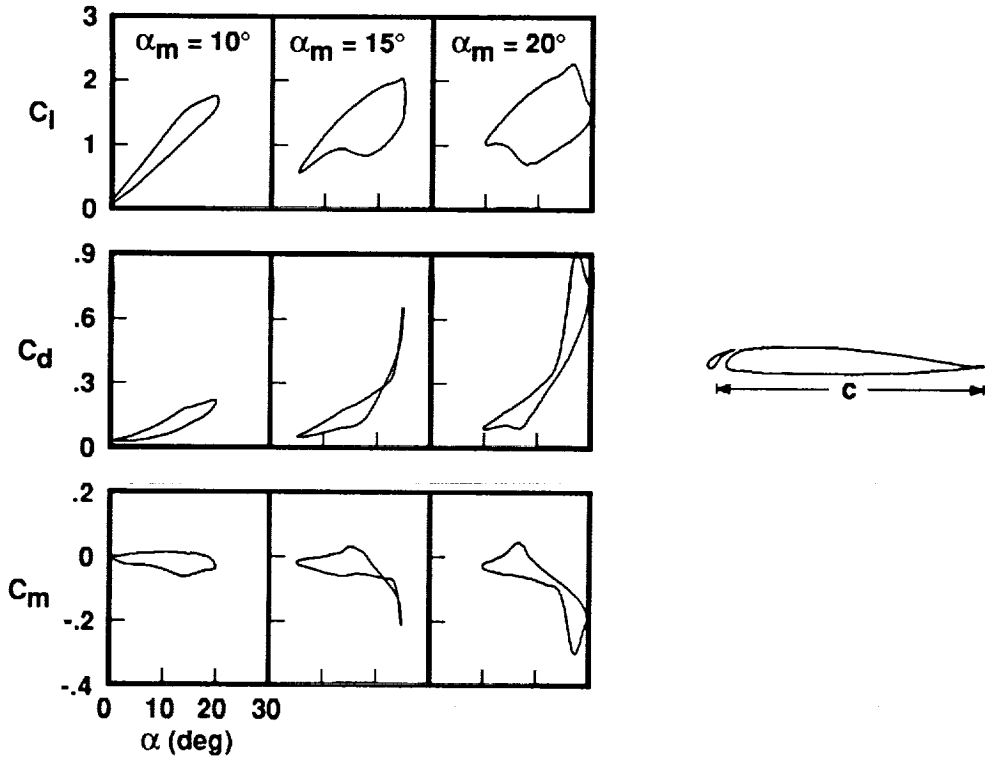

Figure 39. Concluded. (b) $\alpha_m = 10° \rightarrow 20°$.

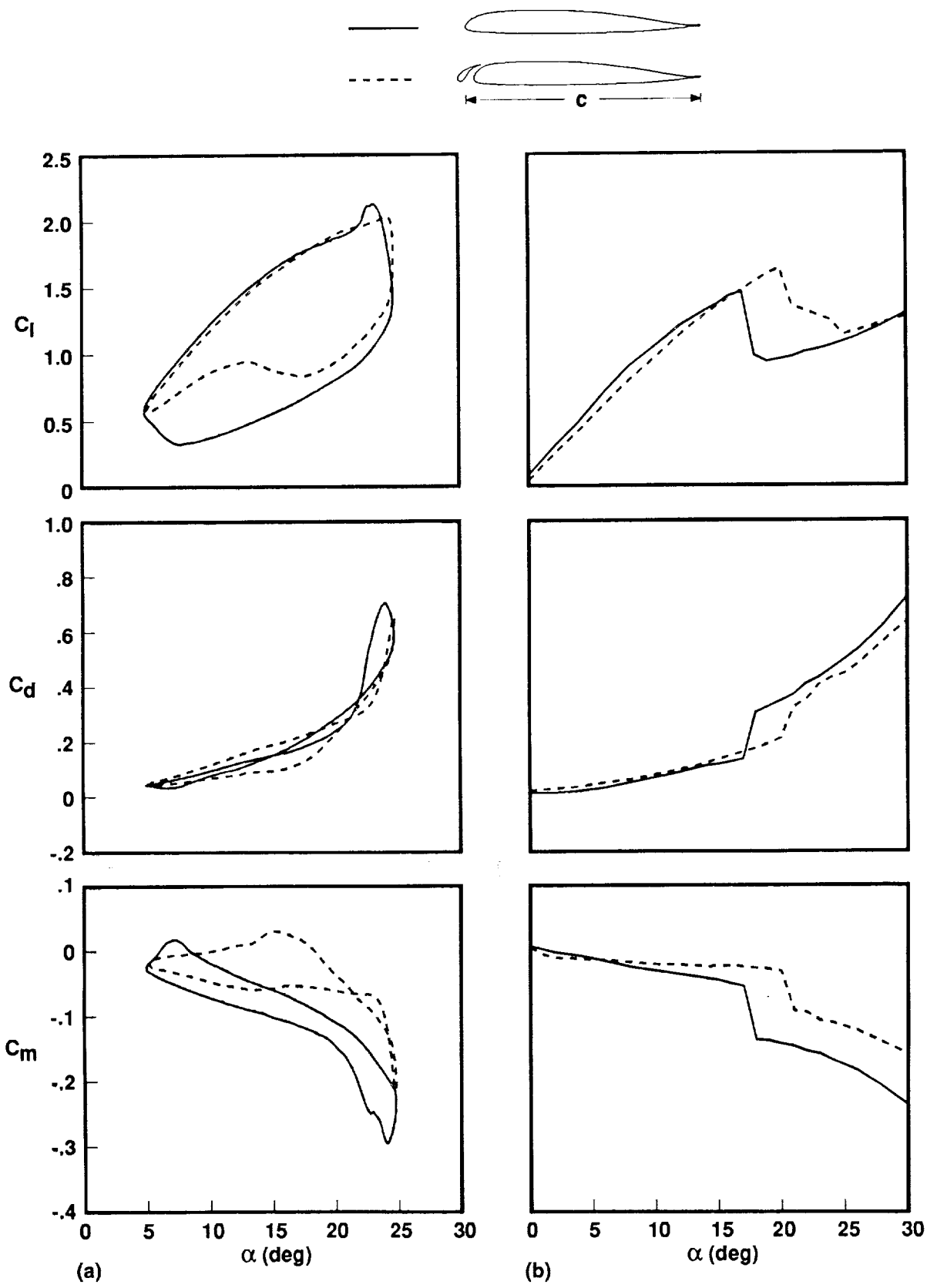

Figure 40. Comparison of measured loads for the basic and extended-slat VR-12 airfoils for steady and unsteady conditions. (a) Unsteady, $\alpha = 15° + 10° \sin(\omega t)$ at $k = 0.10$; (b) steady, $\alpha = 0° \rightarrow 30°$.

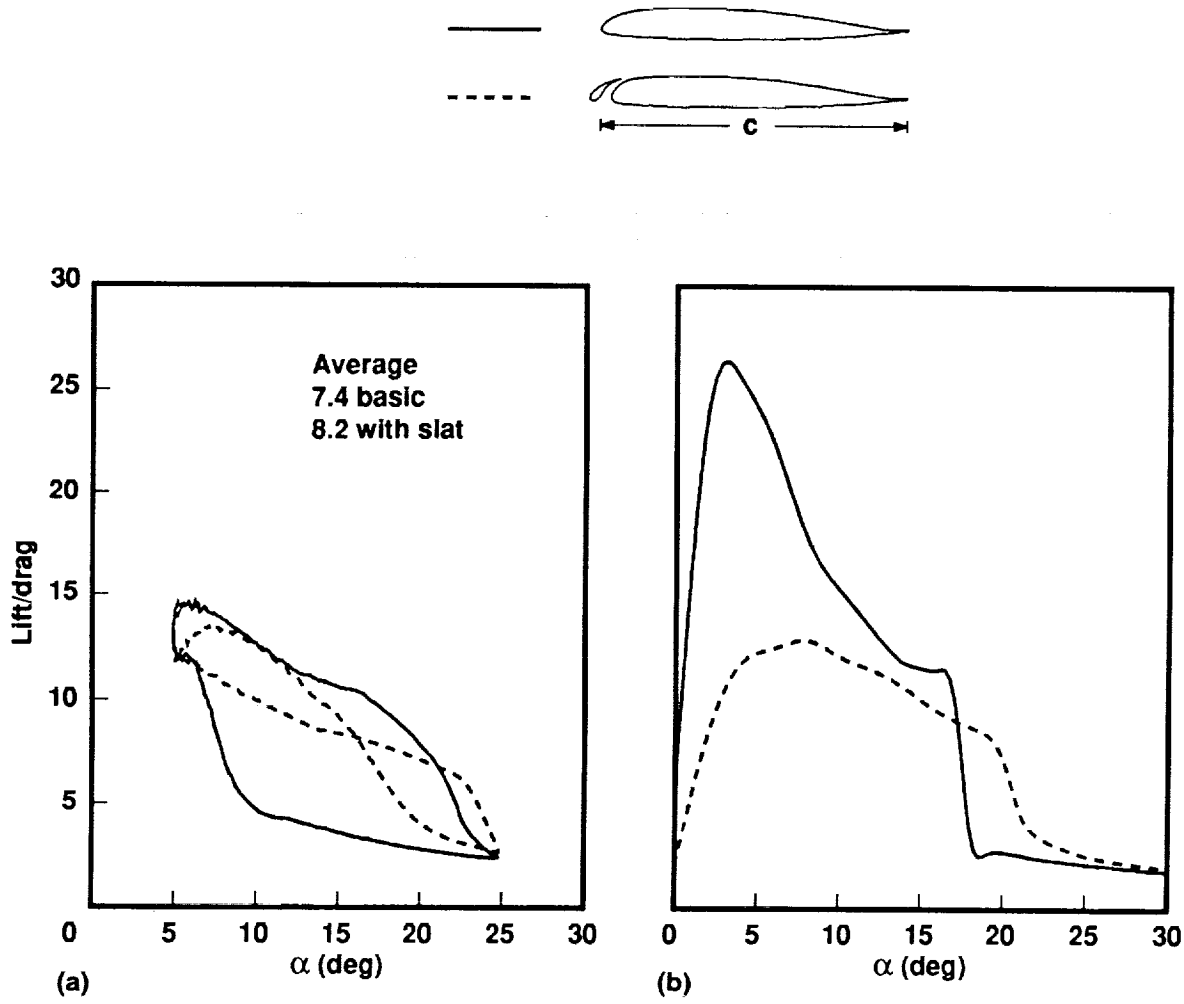

Figure 41. Lift/drag comparison between basic and extended-slat VR-12 airfoils for steady and unsteady conditions. (a) Unsteady, $\alpha = 15° + 10° \sin(\omega t)$ at $k = 0.10$; (b) steady, $\alpha = 0° \rightarrow 30°$.

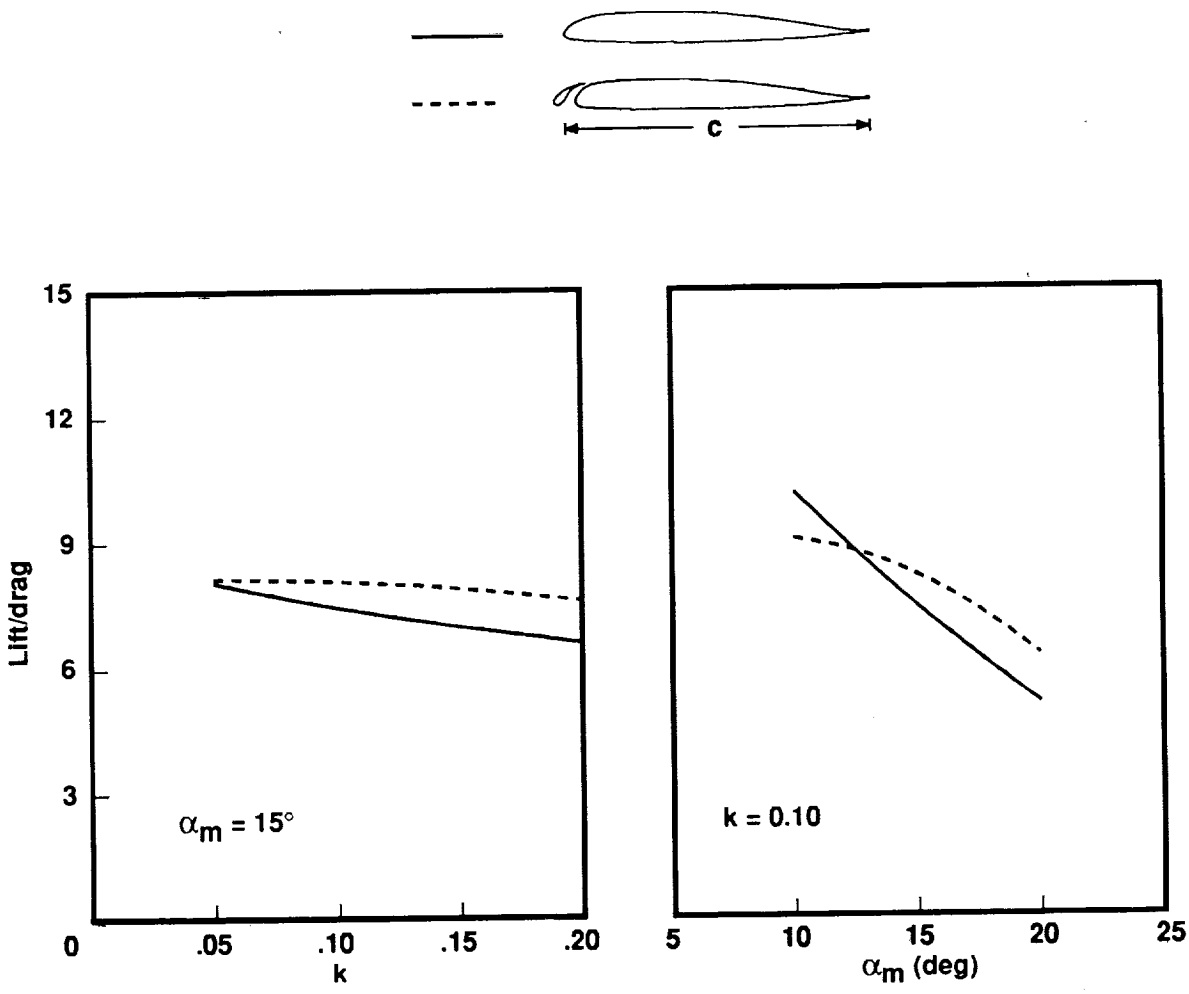

Figure 42. Lift/drag comparison between basic and extended-slat VR-12 airfoils for $k = 0.05 \rightarrow 0.20$ and $\alpha_m = 10° \rightarrow 20°$ with $\alpha = \alpha_m + 10° \sin(\omega t)$.

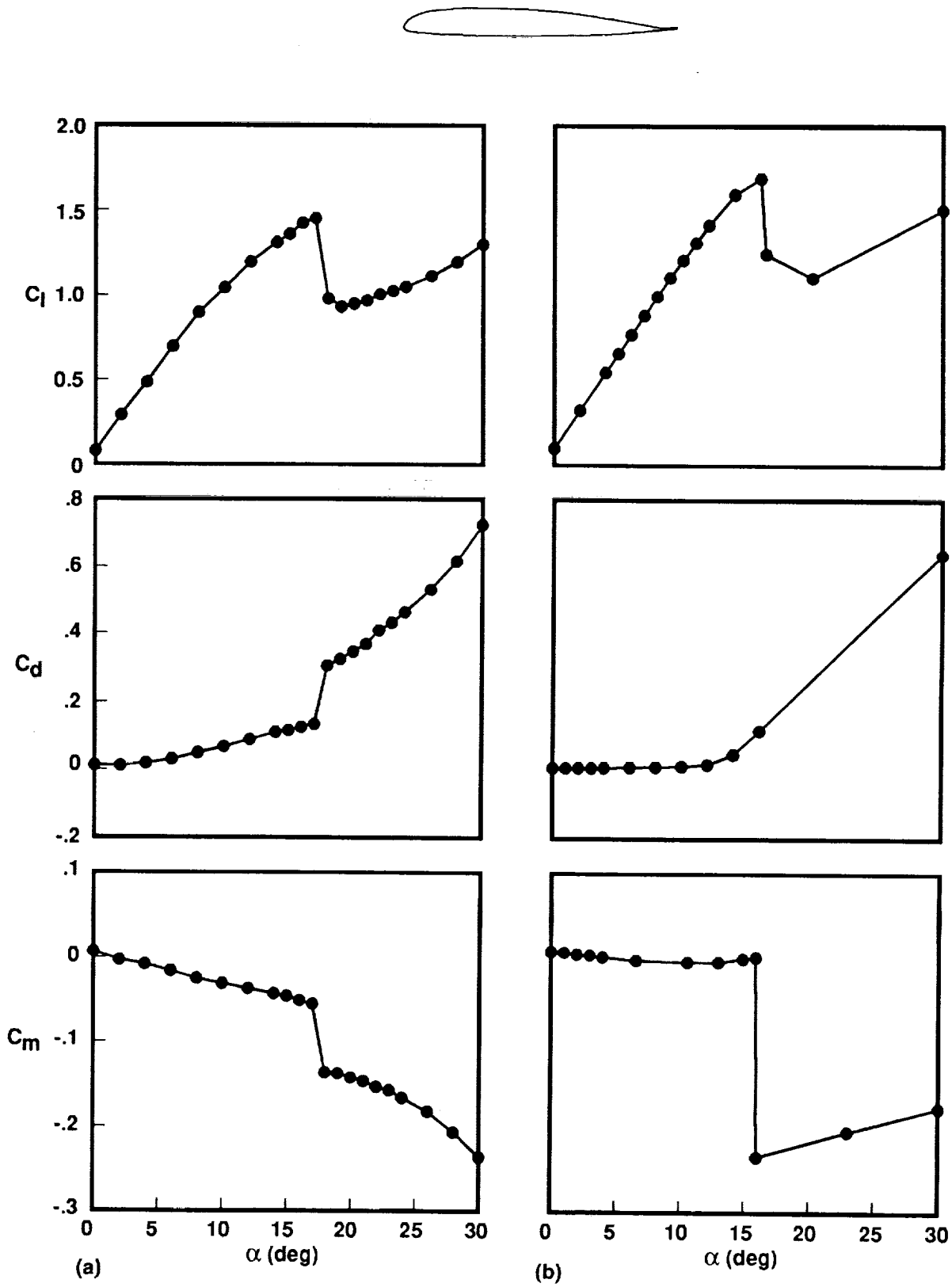

Figure 43. Comparison between water tunnel and wind tunnel results for the basic VR-12 airfoil at fixed angles of attack. (a) Water tunnel, $Re = 2 \times 10^5$ and $M_\infty = 0.0$; (b) wind tunnel, $Re = 4 \times 10^6$ and $M_\infty = 0.3$.

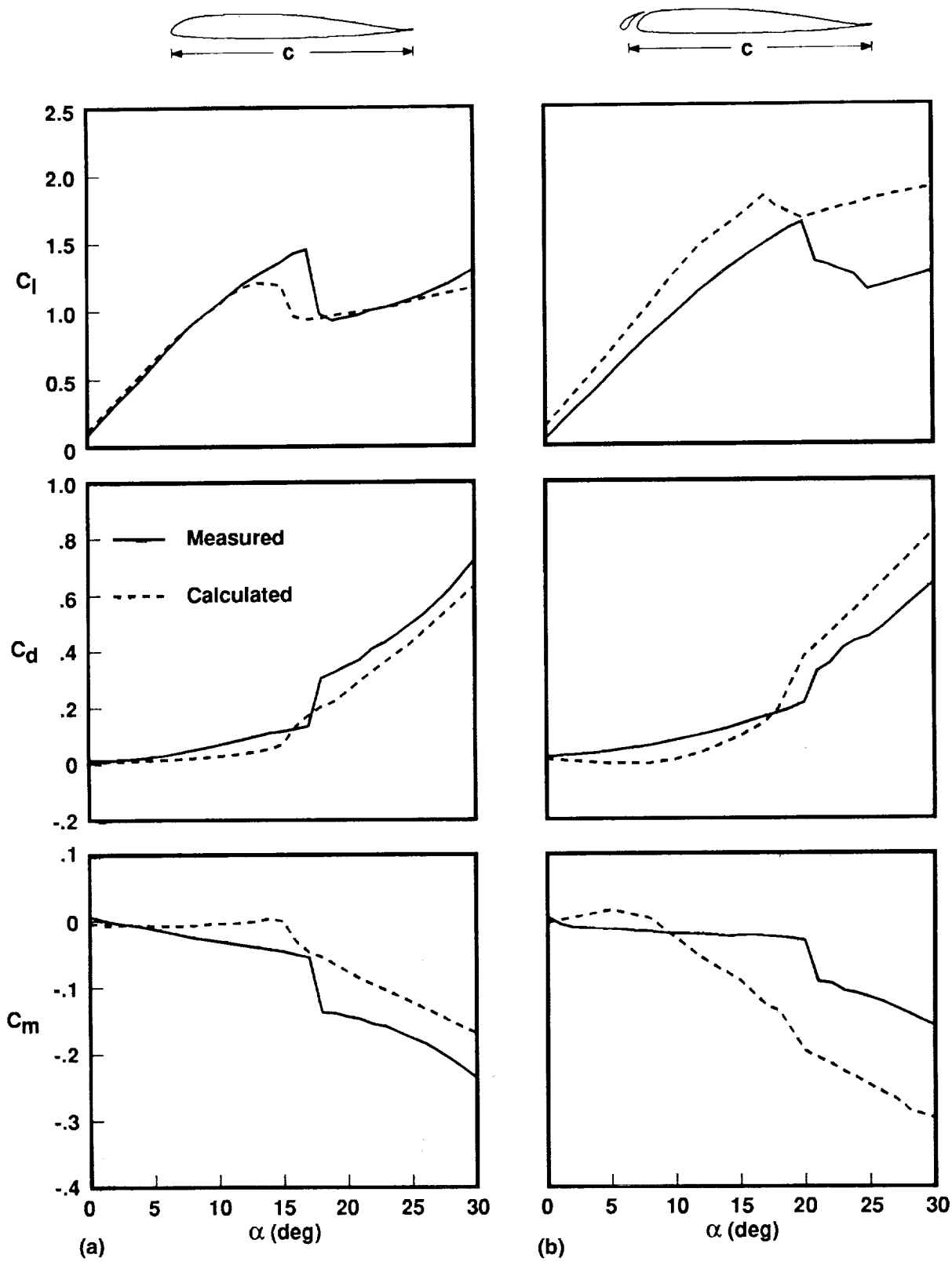

Figure 44. Comparison between measured and calculated results for the basic and the extended-slat VR-12 airfoils at fixed angles of attack. (a) Basic airfoil; (b) extended-slat airfoil.

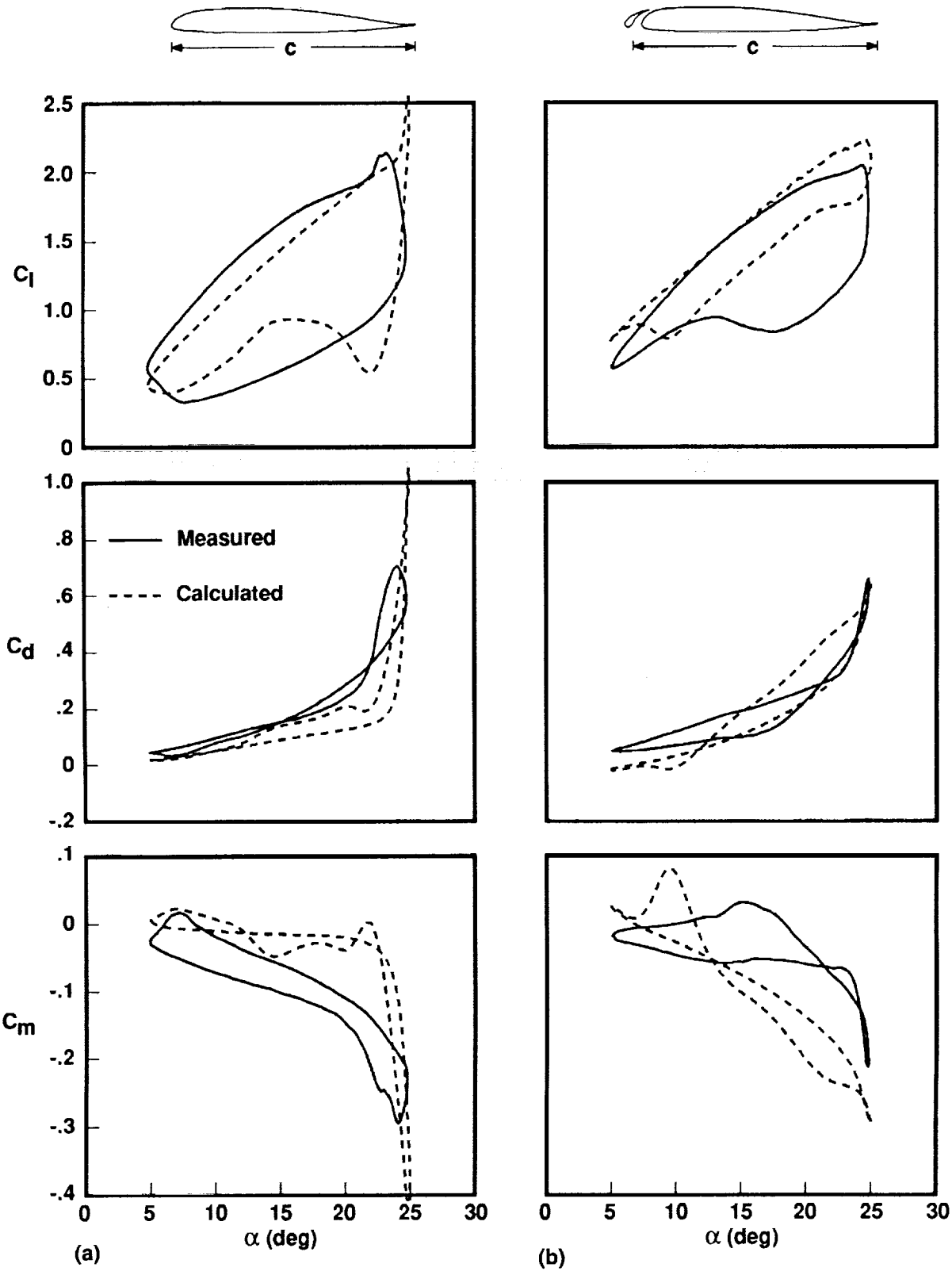

Figure 45. Comparison between measured and calculated results for the basic and the extended-slat VR-12 airfoils with $\alpha = 15° + 10° \sin(\omega t)$ at $k = 0.1$. (a) Basic airfoil; (b) extended-slat airfoil.

REPORT DOCUMENTATION PAGE

Form Approved
OMB No. 0704-0188

1. AGENCY USE ONLY *(Leave blank)*	2. REPORT DATE	3. REPORT TYPE AND DATES COVERED
	September 1993	Technical Paper

4. TITLE AND SUBTITLE
Effect of an Extendable Slat on the Stall Behavior of a VR-12 Airfoil

5. FUNDING NUMBERS
505-61-51

6. AUTHOR(S)
P. Plantin De Hugues,* K. W. McAlister,† and C. Tung†

7. PERFORMING ORGANIZATION NAME(S) AND ADDRESS(ES)
Ames Research Center
Moffett Field, CA 94035-1000

8. PERFORMING ORGANIZATION REPORT NUMBER
A-93056

9. SPONSORING/MONITORING AGENCY NAME(S) AND ADDRESS(ES)
National Aeronautics and Space Administration
Washington, DC 20546-0001

10. SPONSORING/MONITORING AGENCY REPORT NUMBER
NASA TP-3407

11. SUPPLEMENTARY NOTES
Point of Contact: K. W. McAlister, Ames Research Center, MS 215-1, Moffett Field, CA 94035-1000
(415) 604-5892
*French Foreign Ministry, Paris, France. †Aeroflightdynamics Directorate (ATCOM), Ames Research Center.

12a. DISTRIBUTION/AVAILABILITY STATEMENT
Unclassified — Unlimited
Subject Category 02

12b. DISTRIBUTION CODE

13. ABSTRACT ***(Maximum 200 words)***

Experimental and computational tests were performed on a VR-12 airfoil to determine if the dynamic-stall behavior that normally accompanies high-angle pitch oscillations could be modified by segmenting the forward portion of the airfoil and extending it ahead of the main element. In the extended position the configuration would appear as an airfoil with a leading-edge slat, and in the retracted position it would appear as a conventional VR-12 airfoil. The calculations were obtained from a numerical code that models the vorticity transport equation for an incompressible fluid. These results were compared with test data from the water tunnel facility of the Aeroflightdynamics Directorate at Ames Research Center. Steady and unsteady flows around both airfoils were examined at angles of attack between 0° and 30°. The Reynolds number was fixed at 200,000 and the unsteady pitch oscillations followed a sinusoidal motion described by $\alpha = \alpha_m + 10° \sin(\omega t)$. The mean angle ($\alpha_m$) was varied from 10° to 20° and the reduced frequency from 0.05 to 0.20. The results from the experiment and the calculations show that the extended-slat VR-12 airfoil experiences a delay in both static and dynamic stall not experienced by the basic VR-12 airfoil.

14. SUBJECT TERMS
Airfoil stall, Dynamic stall, Leading-edge slat, High-lift device

15. NUMBER OF PAGES
66

16. PRICE CODE
A04

17. SECURITY CLASSIFICATION OF REPORT	18. SECURITY CLASSIFICATION OF THIS PAGE	19. SECURITY CLASSIFICATION OF ABSTRACT	20. LIMITATION OF ABSTRACT
Unclassified	Unclassified		